ISBN 0208 189X (print)
ISSN 1736-7492 (electronic)

Oil Shale

CONTENTS

2026 V.43 N.3

Tallinn 2026

International open access scientific journal
of the Estonian Academy of Sciences
published in collaboration with
Tallinn University of Technology
and the Geological Survey of Estonia

Published since 1984

OIL SHALE 2026, Vol. 43, No. 3

Abstracted/indexed in Science Citation Index Expanded (Web of Science), Current Contents – Engineering, Computing & Technology (Web of Science), Scopus, EBSCO, The Gale Group Inc., ProQuest LLC, Airiti Inc., Scilit, Directory of Open Access Journals (DOAJ)

Full texts available at www.eap.ee/oilshale

Executive Editor: Hedi Tõnso, hedi.tonso@eap.ee
Copyeditor: Kadri Põdra
Layout: Ulla Säre
Consultant: Peet M. Sööt (USA), peet@cmmenergy.com

The journal is published quarterly

Printed by Alfapress OÜ, Reti tee 8, 75312 Peetri, Estonia

Oil Shale, 2026, 43, 3, 241–260 https://doi.org/10.3176/oil.2026.3.01

Review and outlook on the application of thermal-hydraulic-mechanical coupling simulation in in-situ oil shale mining

Shuang Liang[(a)], Yi Pan[(a)], Mingzhe Guo[(a)]*, Hui Yang[(b)]

[(a)] College of Oil and Gas Engineering, Liaoning Petrochemical University, Fushun 113001, China
[(b)] Kunlun Safety & Health Technology Company, Beijing 102200, China

Received 9 October 2025, accepted 1 July 2026, available online 3 August 2026

Abstract. *Against the backdrop of surging global energy demand, oil shale, as a plentiful unconventional energy resource, has emerged as a research hotspot for in-situ exploitation. Oil shale pyrolysis involves temperature, seepage, and stress field coupling, leading to surface deformation and fracture propagation that affect mining efficiency. Thermal-hydraulic-mechanical coupling simulation can effectively reveal multi-physical field interaction mechanisms in reservoirs and offer theoretical support for optimizing mining processes. This paper reviews its application in in-situ oil shale mining, summarizes coupling theories and mathematical models, and analyzes its value in heat injection mining, effective pyrolysis zone prediction, and ground surface deformation analysis. It also summarizes key applications and prospects for future directions, and provides theoretical and technical references for optimizing in-situ oil shale mining, thereby laying a foundation for subsequent thermal-hydraulic-mechanical-chemical research.*

Keywords: *oil shale, in-situ oil shale mining, thermal-hydraulic-mechanical (THM) coupling, thermal-hydraulic-mechanical (THM) coupling simulation, in-situ heat injection mining.*

1. Introduction

Currently, global energy demand continues to grow, while traditional petroleum resources are increasingly depleted due to long-term extraction. This supply–demand contradiction is accelerating the strategic transition in the energy sector, making the development of unconventional energy a key pathway to address the challenge. Among these, oil shale has attracted widespread attention owing to its significant advantages of extensive distribution and abundant reserves [1, 2]. As shown in Figure 1, the global proven reserves

---

* Corresponding author, gmz_lsh@126.com

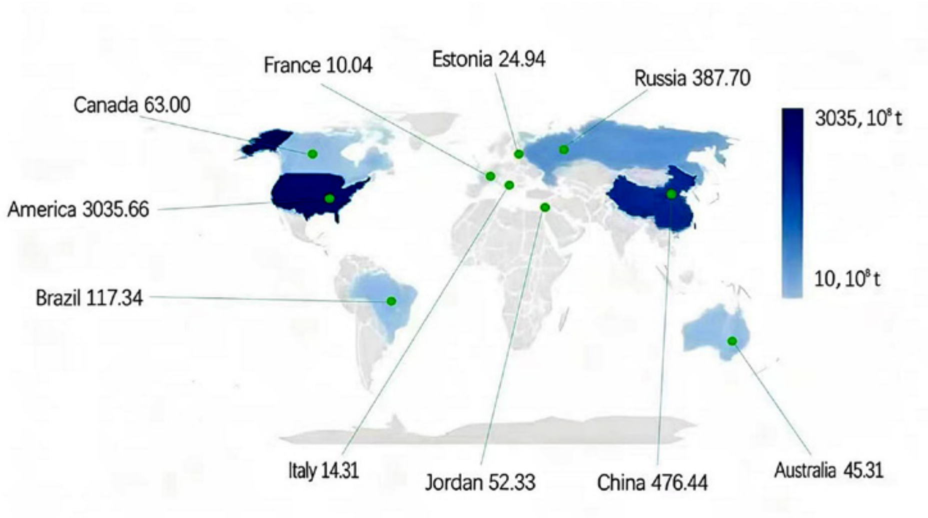

Fig. 1. Distribution map of proven oil shale reserves worldwide.

of oil shale can reach as high as 400 billion tons, demonstrating significant potential for industrial development and application [3]. Therefore, oil shale is regarded as one of the important alternative energy sources to conventional resources [4, 5]. In-situ mining technology promotes the pyrolysis of kerogen in oil shale to generate oil and gas through underground heating. Due to its advantages of reduced environmental impact and high resource utilization efficiency, it has become the main technical approach for the industrial development of oil shale [6, 7]. Oil shale pyrolysis is the process where kerogen decomposes into shale oil, gas, and water at high temperatures. This process triggers a series of physicochemical reactions such as water volatilization, kerogen thermal decomposition, and rock fracture, promoting the formation of pores and fractures and significantly enhancing permeability [8, 9]. These microscale pores and fractures serve as both channels for the migration of pyrolysis products and spaces for internal heat exchange, directly determining rock permeability and representing a crucial link for the efficient realization of in-situ conversion [10].

However, in-situ oil shale mining is a complicated, coupled process involving heat conduction, fluid seepage, rock deformation, and chemical reactions [11]. The high temperatures induced by heat injection not only drive the pyrolysis of organic matter but also lead to complex dynamic interactions among the reservoir temperature field, seepage field, and stress field. These interactions directly affect pyrolysis efficiency, the formation of fracture networks, and even formation stability [12]. Traditional single-physics field models or uncoupled models with simple superposition fail to effectively address rock thermal deformation, mechanical property evolution, pyrolysis product generation, seepage-induced pore pressure changes, and their fracture-driving effects, all of which result from temperature variations. Nor can they account for the reverse impact of stress field redistribution on pore structure and seepage–thermal conduction paths. This limits the reliability of process parameter optimization and safety assessment in in-situ oil shale exploitation.

Thermal-hydraulic-mechanical (THM) coupling simulation integrates temperature fields, rock deformation, and fluid seepage to reveal multi-physical field coupling behaviors during in-situ oil shale exploitation [13]. Notably, while pyrolysis is inherently a chemical process and current research has extended to thermal-hydraulic-mechanical-chemical (THMC) coupling simulation, this paper focuses on THM coupling simulation. It captures the core mechanisms governing pyrolysis: heat transfer, fluid migration, fracture propagation, and rock deformation. In practice, chemical processes such as kerogen conversion kinetics are often simplified as heat and fluid source terms, integrated into THM models to indirectly capture their effects. By concentrating on this central mechanism, the paper reviews the theoretical and application progress of THM simulation, discussing its value in heat injection mining, effective pyrolysis zone and fracture prediction, and ground surface deformation analysis. This work supports the optimization of oil shale extraction parameters and risk prevention, while laying a physical foundation and establishing a model framework for subsequent comprehensive studies on THMC multi-field coupling.

2. Theory and model of thermal-hydraulic-mechanical coupling simulation

As a crucial method for investigating the interactions among multi-physics fields during the in-situ mining of oil shale, THM coupling simulation has its theoretical basis and model construction directly determining the accuracy and reliability of the simulation.

2.1. Theoretical origin of THM coupling simulation

Fluid-solid coupling serves as the foundation of THM coupling. The earliest research on fluid-solid coupling originated with Terzaghi, who proposed the effective stress principle and one-dimensional consolidation theory, thereby laying the groundwork for subsequent studies. However, the initial theory was limited by its assumptions and had restricted capability in solving practical problems [14]. Subsequently, in 1955–1956, Biot [15, 16] built upon this work and established a more comprehensive three-dimensional consolidation model for isotropic porous media under isothermal conditions, later extending the consolidation theory to anisotropic porous media and dynamic analysis. Rice and Cleary [17] introduced the easily determinable Skempton constant, deriving an alternative expression of Biot's theory. In 1984, Zienkiewicz and Shiomi [18] further advanced the development of fluid-solid coupling theory by accounting for geometric and material nonlinearities, proposing a generalized form of Biot's theory.

It is noteworthy that in the fluid-solid coupling theory, the temperature field remains constant. However, during the actual development of oil and gas reservoirs – especially for low-permeability reservoirs such as oil shale – the reservoir temperature undergoes significant changes during the dynamic mining process. Temperature variation not only directly affects the mechanical properties of rocks but also influences the fluid seepage process through changes in fluid physical property parameters. Meanwhile, rock deformation leads to alterations in pore structure, which in turn affects fluid seepage [13]. These factors interact with each other, forming a complex coupling effect among THM fields, as illustrated in Figure 2.

Therefore, traditional fluid-solid coupling models can no longer accurately simulate the real conditions of reservoirs. It is necessary to thoroughly consider the coupling effects among temperature variation, rock deformation, and fluid seepage, which has led the THM coupling theory to gradually become a research focus in the field of oil and gas reservoir development.

In early studies, Bear and Corapcioglu [19] investigated the variations in in-situ stress, temperature, and rock permeability within geothermal regions during geothermal resource extraction. Lewis et al. [20] accounted for the influence of temperature changes on fluid density, phase transitions, and rock thermal expansion, and analyzed how rock deformation alters fluid flow paths through changes in porosity and permeability. Additionally, they noted that variations in fluid pressure during seepage exert a feedback effect on the rock skeleton. Jing et al. [21] conducted research on fluid flow, solid deformation,

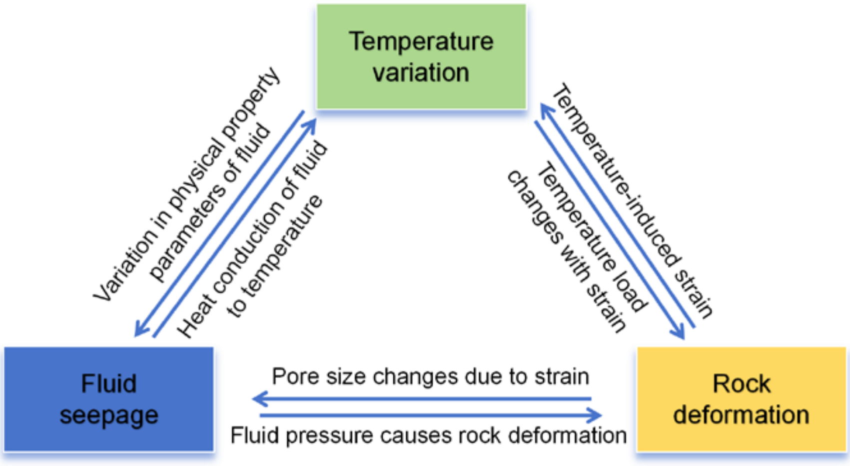

Fig. 2. Thermal-hydraulic-mechanical coupling diagram.

and heat transfer in hard rock structures but did not systematically consider the full coupling effect among temperature, seepage, and deformation. In 1997, Gutierrez and Makurat [22] developed a THM coupling model to investigate the fluid-solid coupling process during water injection into pressurized fractures; however, limited by technical constraints, the relationship between the temperature field and rock deformation was not considered. Starting from the interrelationships among rock mass seepage, stress, and temperature, Chai [23] established a coupling mechanism for THM processes.

With the deepening of research, scholars have progressively applied the THM coupling theory to the in-situ mining of oil shale. In 2008, Kang [24] was the first to integrate the theories of rock mechanics, heat transfer, and seepage mechanics, establishing a THM coupling mathematical model for the in-situ heat injection mining of oil shale. This model provided a crucial basis for the application of THM coupling simulation in oil shale-related studies. Zhao [25] further developed a THM coupling model for the underground co-gasification and thermal mining of oil shale and coal, analyzing the dynamic distribution laws of the temperature field, seepage field, and stress field during the gasification process of oil shale reservoirs. Wang [26] pioneered the establishment of an anisotropic THM coupling mathematical model for oil shale. Utilizing parameters related to heat transfer, seepage, mechanics, and deformation obtained from laboratory experiments, he analyzed the variation laws of reservoir pore pressure, temperature, stress, deformation, permeability, and production during the in-situ pyrolysis of oil shale. Jin et al. [27] developed a THM-coupled model that incorporates the temperature dependence of key properties of oil shale and the transverse isotropy resulting from its bedding structure. This model integrates multi-stage pyrolysis kinetics of kerogen, fluid flow in porous media, and heat transfer processes, providing theoretical guidance and parameter optimization strategies for the field application of in-situ oil shale conversion.

Amid in-depth research on in-situ oil shale conversion mechanisms and a growing understanding of multi-field coupling effects during extraction, the THM coupling theory has expanded toward two key directions: one focuses on developing a fully coupled THMC model, which integrates chemical reaction kinetics (e.g., kerogen pyrolysis) into the physical field coupling system to accurately simulate the interactions among heat transfer, product generation, and rock mass deformation [28, 29]; the other centers on developing a refined model considering anisotropy, which couples thermal damage theory with anisotropic constitutive relations to characterize the evolution of permeability and mechanical properties induced by directional fracture development [30, 31]. These advancements have propelled simulations from traditional three-field physical coupling to a new stage of full physical-chemical coupling and dynamic characterization of reservoir properties, providing more precise theoretical support for optimizing in-situ mining processes.

2.2. Construction of the mathematical model of THM coupling simulation

The mathematical model of THM coupling forms the core of numerical simulation and can be broadly categorized into non-complete coupled and complete coupled approaches [32]. Non-complete coupled models introduce temperature-related functions based on fluid-solid coupling frameworks but fail to account for the dynamic coupling effects among temperature variations, rock deformation, and fluid flow. For instance, Wang et al. [33] developed a non-complete coupled mathematical model that comprises the following three types of equations: seepage equations, rock deformation equations, and thermal strain equations.

Seepage equation:

$$\nabla\left[\frac{KK_r\rho}{\mu}\nabla(p-\gamma D)\right]-\nabla(\phi S\rho v_s)+q=\frac{\partial(\phi S\rho)}{\partial t}, \tag{1}$$

where ∇ is the Hamilton operator, K is the absolute permeability of oil and gas reservoirs (mD), D is elevation (m), Kr is the relative permeability of oil and gas reservoirs (mD), μ is fluid viscosity (mPa · s), γ is the weight rate, ρ is density (g/cm^3), p is fluid pressure (MPa), ϕ is porosity, v_s is the absolute velocity of solid particles (cm/s), S is fluid saturation, t is time (s), and q is the source or sink of material change per unit volume (cm^3/s).

Rock deformation:

$$\sigma'_{ij,i}+\left(p\delta_{ij}\right)_i+\sigma^h_{ij,i}+[(1-\phi)\rho_s+\phi S_o\rho_o+\phi S_w\rho_w]g_j=0, \tag{2}$$

$$\varepsilon_{ij}=\frac{1}{2}\left(u_{i,j}+u_{j,i}\right), \tag{3}$$

$$d\sigma'_{ij}=D^{ep}d\varepsilon_{ij}, \tag{4}$$

where $\sigma'_{ij,i}$ is the effective stress tensor (MPa), $\sigma^h_{ij,i}$ is thermal stress (MPa), δ_{ij} is the Kronecker function, ε_{ij} is the strain tensor, u is displacement (m), D^{ep} is an elastic-plastic matrix, $g_j = [\ 0\ 0\ g\ ]$, where g is the acceleration of gravity (m/s^2), S_o and S_w are oil saturation and water saturation, respectively, ρ_o and ρ_w are the density of oil and water, respectively (g/cm^3), and ρ_s is rock skeleton density (g/cm^3).

Thermal strain equation:

$$\{R\}^e+\iiint[B]^T[D][\varepsilon_0]dx\,dy\,dz=[K]^e\{\delta\}^e, \tag{5}$$

where $\{R\}^e$ is the equivalent nodal force due to external forces, $[B]^T$ is the element strain matrix, $[D]$ is the constitutive matrix for the unit, $[\varepsilon_O]$ is the unit thermal strain, $[K]^e$ is the element stiffness matrix, and $\{\delta\}^e$ is the virtual displacement of the node.

In contrast, complete coupled models comprehensively account for the coupling effects among temperature variation, rock deformation, and fluid seepage, making them more consistent with the actual conditions of temperature-varying oil and gas reservoirs. The fully coupled mathematical model constructed by Li et al. [34] comprises three components: seepage equations, temperature field equations, and rock deformation equations. Within the seepage equations, the influences of temperature and pressure on fluid density, viscosity, and rock permeability are comprehensively considered, the temperature field equations incorporate the effect of solid deformation on heat energy conservation, and the rock deformation equations take into account the roles of fluid pore pressure and thermal stress. This model system can describe the physical phenomena in the oil shale mining process more accurately and provide a more reliable basis for numerical simulations.

Seepage equation:

$$\nabla\left[\frac{K}{\mu_f}\nabla\left(p+\rho_f gz\right)\right]+c_a\frac{\partial T}{\partial t}-c_k\frac{\partial p}{\partial t}-(1-\phi)\frac{\partial \varepsilon_k}{\partial t}=0, \tag{6}$$

where ρ_f is fluid density (g/cm^3), μ_f is fluid viscosity (mPa · s), c_a is the average coefficient of thermal expansion, c_k is the average volume compression coefficient, ε_k is volume strain, z is depth (m), and T is the absolute temperature change value at a certain point in the rock mass (K).

Thermal strain equations:

$$c\frac{\partial T}{\partial t}+\rho_f c_f\left(v_f\nabla\right)T+\beta T_0\frac{\partial \varepsilon_k}{\partial t}-c_t T_0\frac{\partial p}{\partial t}-\nabla(\lambda\nabla T)=0, \tag{7}$$

$$c_t=\frac{(1-\phi)\rho_s c_s}{k_s}+\frac{\phi\rho_f c_f}{k_f}, \tag{8}$$

where T_0 is the absolute temperature (K), c is the average heat capacity, c_s and c_f are the heat capacity coefficients of the solid and fluid, respectively, β is the thermal stress coefficient, k_s and k_f are the bulk elastic moduli of the solid and fluid, respectively (MPa), λ is the average thermal conductivity, and v_f is the seepage velocity (cm/s).

Rock deformation equations:

$$\left.\begin{aligned}(G+\gamma)\frac{\partial \varepsilon_k}{\partial x}+G\nabla^2 u+\alpha\frac{\partial p}{\partial x}-\beta\frac{\partial T}{\partial x}+f_x=\rho_s\frac{\partial^2 u}{\partial t^2}\\(G+\gamma)\frac{\partial \varepsilon_k}{\partial y}+G\nabla^2 v+\alpha\frac{\partial p}{\partial y}-\beta\frac{\partial T}{\partial y}+f_y=\rho_s\frac{\partial^2 v}{\partial t^2}\\(G+\gamma)\frac{\partial \varepsilon_k}{\partial z}+G\nabla^2 w+\alpha\frac{\partial p}{\partial z}-\beta\frac{\partial T}{\partial z}+f_z=\rho_s\frac{\partial^2 w}{\partial t^2}\end{aligned}\right\}, \tag{9}$$

where G and γ are the Lamé coefficients, α is the Biot coefficient, f_x, f_y, and f_z are the volume force components, and u, v, and w are the solid displacement components.

The mathematical model for THM coupling simulation is a complex interdisciplinary system involving multiple fields such as thermodynamics, fluid mechanics, solid mechanics, and chemical reactions. By coupling these physical processes, the physical and chemical behavior of oil shale during the in-situ mining process can be simulated and predicted more accurately.

3. Application of thermal-hydraulic-mechanical coupling simulation of oil shale

THM coupling simulation holds broad application prospects in oil shale development, with its specific applications in areas such as in-situ heat injection mining, effective pyrolysis zone prediction, and ground surface deformation analysis significantly advancing the understanding and optimization of in-situ mining processes.

3.1. Simulation and optimization of in-situ heat injection mining

In the in-situ thermal injection mining of oil shale, high-temperature steam is injected into the oil shale reservoir to heat and decompose the organic matter stored therein into oil and gas products. Meanwhile, the mineral skeleton of oil shale undergoes complex physicochemical changes, forming seepage channels conducive to product transportation. This process involves intricate THM coupling effects [35].

THM coupling simulation can reveal the interrelationships among steam migration, temperature propagation, and rock deformation. For instance, Kang [24] established a THM coupling mathematical model for in-situ steam injection development of oil shale, which represents a crucial breakthrough in the application of THM coupling simulation technology in the field of in-situ heat injection mining of oil shale.

Liu [36] further studied the evolution of the physical properties of oil shale and fluids under the action of temperature and pressure. Through THM coupling simulation, he analyzed the dynamic distribution laws of the temperature field, seepage field, and displacement field during the in-situ heat injection process of oil shale, providing a reference basis for the in-situ heat injection mining of oil shale.

Wang et al. [37] took the Fushun oil shale reservoir as the research object, set the injection temperature at 650 °C and the injection pressure at 3 MPa, and compared the efficiency of conduction heating and steam convection heating by THM coupling simulation. Under the same pyrolysis time, the effective pyrolysis area ratio of steam convection heating is 22.4 times that of conduction heating, and the oil production is 7259 times that of conduction heating, which fully proves that the efficiency of convection heating pyrolysis of oil shale is much higher than that of conduction heating.

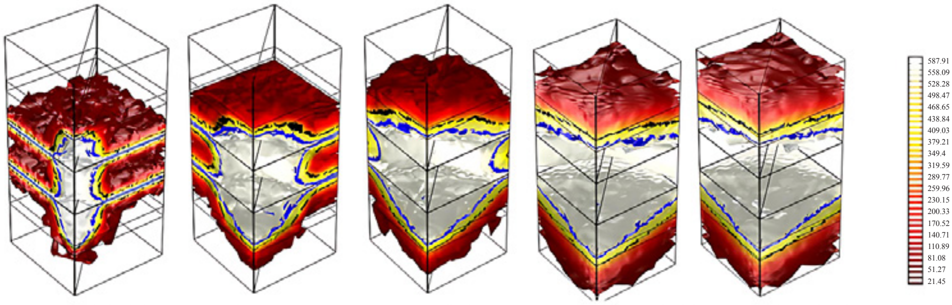

(a) 30 d (b) 150 d (c) 300 d (d) 500 d (e) 800 d

Fig. 3. Temperature distribution of the reservoir at different times [38].

To accurately simulate the in-situ pyrolysis process of oil shale, Wang et al. [38] established a coupled model considering transversely isotropic THM characteristics to simulate the in-situ pyrolysis process of superheated steam. Figure 3 shows the temperature distribution of in-situ steam injection pyrolysis of oil shale at different times. The temperature of the ore layer within the blue line is higher than 550 °C, and the temperature of the ore layer outside the black line is lower than 350 °C. It can be seen from the figure that the initial heat is transmitted along high-permeability fractures. Because the permeability of the parallel bedding is much higher than that of the vertical direction, and the high pressure of the wellbore promotes the migration of steam, an ellipsoidal high temperature zone is rapidly formed. At 500 days, the oil shale between the injection and production wells basically reaches the pyrolysis temperature. THM simulation can intuitively show the dynamic evolution law of reservoir temperature field with steam injection time, and provide key visual evidence for understanding the oil shale pyrolysis process.

In 2025, Chen et al. [30] pioneered the integration of a statistical damage variable into the THM coupling theory for three-dimensional fractured rock masses. They developed a coupled model that incorporates anisotropic thermal damage and a transverse isotropic constitutive law. Using COMSOL simulations of the in-situ conversion process under convective heating, their study revealed the intrinsic relationship between the anisotropy of pore structures and the physico-mechanical properties of oil shale during in-situ steam injection pyrolysis.

3.2. Prediction of effective pyrolysis zone and fracture propagation

The dynamic evolution of the effective pyrolysis zone and the law of fracture propagation are the core factors that determine the mining efficiency of oil shale. THM coupling simulation provides key technical support for improving reservoir utilization efficiency and optimizing mining conditions by accurately quantifying the influence of the temperature field on kerogen pyrolysis and the development mechanism of fractures under the coupling of the three fields.

THM coupling simulation can accurately predict the variation law of the effective pyrolysis zone of the reservoir and its pyrolysis effect, and this evolution has become a key indicator for evaluating mining efficiency in in-situ oil shale heat injection exploitation. The objective of in-situ oil shale exploitation is to fully pyrolyze its organic matter (kerogen). Consistent with existing findings, Wang et al. [39] and Saif et al. [40, 41] demonstrated that the complete pyrolysis temperature of oil shale kerogen is generally above 400 °C. Only when the temperature threshold is reached can kerogen undergo sufficient pyrolysis, generating recoverable oil and gas products. Thus, to define the temperature range enabling sufficient kerogen pyrolysis and meeting exploitation needs, 400 °C is designated as the effective pyrolysis temperature, and the zone with temperatures above 400 °C is defined as the effective pyrolysis zone.

Tang et al. [42] revealed the multi-physical field variation law of the reservoir during in-situ heat injection mining of oil shale using THM coupling simulation and conducted an in-depth analysis of the variation law of the effective pyrolysis zone of the Fushun oil shale reservoir with heat injection time, which provided an important theoretical reference for the in-situ heat injection mining of oil shale.

Addressing the challenges of unclear evolution patterns in the reservoir's effective pyrolysis zone and difficulties in accurately evaluating actual pyrolysis effectiveness during in-situ heat injection mining of oil shale, Yu et al. [43] developed a THM coupling model that incorporates two distinct types of random fractures: bedding fractures and hydraulic fractures. Through THM coupling simulation, they successfully analyzed the evolution characteristics of the effective pyrolysis zone during the in-situ thermal extraction process. As shown in Figure 4a, when superheated steam diffuses along bedding fractures, multiple narrow and elongated primary pyrolysis pathways are formed. In contrast, Figure 4b demonstrates that when superheated steam propagates through hydraulic fractures, it does not form such elongated pathways but rapidly establishes a dendritic high-temperature network.

In addition, the stress field distribution of the oil shale reservoir and its influence on fracture propagation are also a research focus of THM coupling simulation. The fracture propagation of oil shale is not only affected by the temperature field during pyrolysis but also by the combined action of the in-situ stress field and fluid pressure. Based on the THM coupling model, Huang [44] found that fractures exhibit bidirectional propagation characteristics under the combined effects of thermal stress and expansion forces: outward extension when dominated by expansion forces, and inward propagation when primarily driven by thermal stress. Moreover, thermal stress plays a critical role in determining the initiation locations and quantity of fractures.

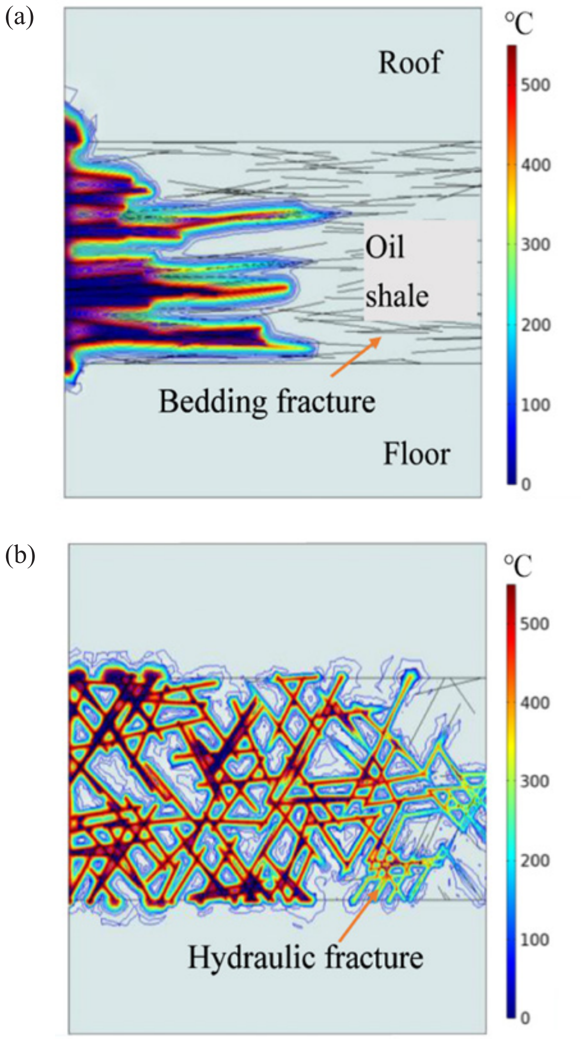

Fig. 4. Temperature changes in a bedding fracture reservoir (a) and in a hydraulic fracturing reservoir (b) with heat injection time [43].

On this basis, Lee et al. [45, 46] used a self-developed kerogen pyrolysis simulator with complete functions to simulate the kerogen pyrolysis process in a steam-injected multi-stage horizontal well system with transverse fractures. They clarified that the fluid conduction effect of fractures and the irreducible water saturation of the reservoir matrix jointly influence oil production capacity.

In 2024, Jia et al. [47] further constructed Case 1 (single fracture, hydraulic fracturing) and Case 2 (multi-fracture, hydraulic fracturing + penetrating thermal fracturing) models and used THM coupling simulation technology to simulate the heat transfer process under 200 m buried depth stress. The temperature distribution cloud diagram is shown in Figure 5. The single-crack model presents a "single-peak" heat transfer mode. The heat is mainly concentrated around the crack, and the temperature at the center of the crack is the highest. In contrast, the multi-crack model presents a "multi-peak" heat transfer mode, and the high-temperature region covers a wider range. At the same time, they also studied the effects of permeability and external stress on oil shale pyrolysis. It is found that under the condition of constant external stress and thermo-mechanical coupling, after exceeding the critical temperature of oil shale, the mechanical strength of the rock increases significantly, and the permeability increases sharply.

(a)

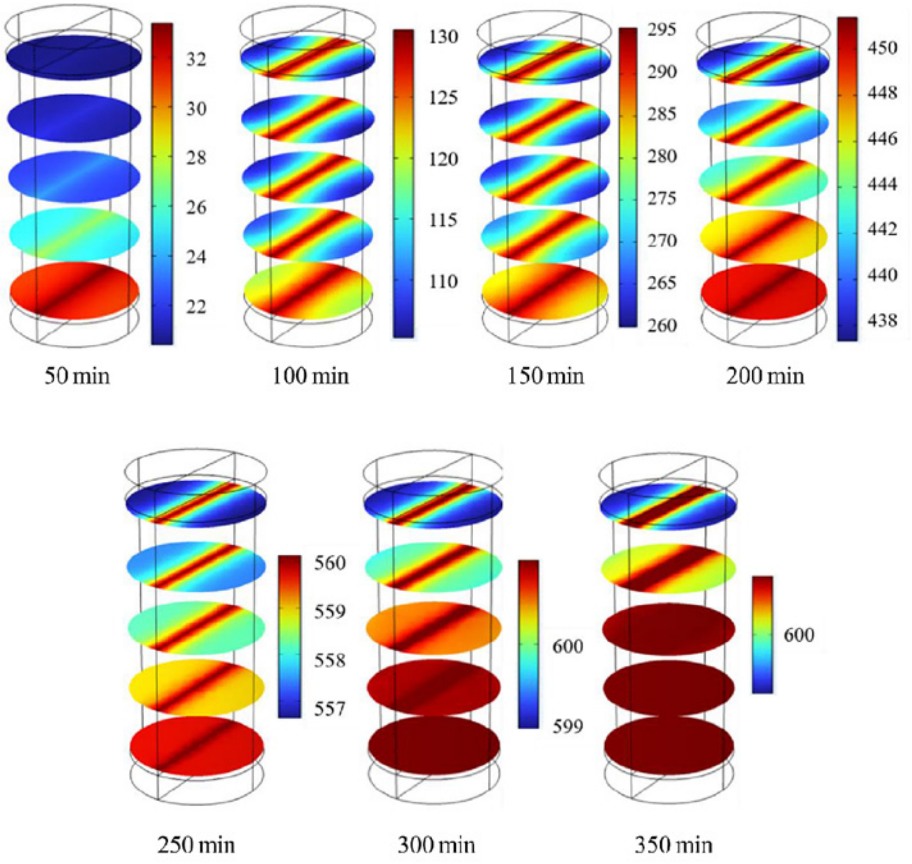

(b)

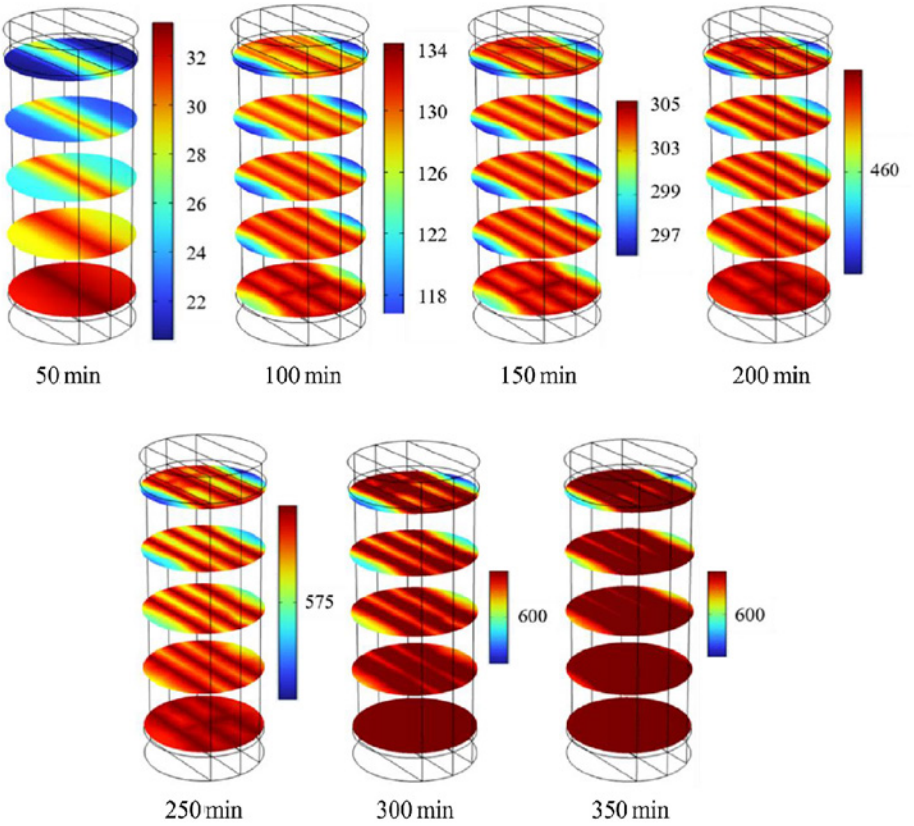

Fig. 5. Cloud diagram of the heat transfer process in Case 1 (a) and Case 2 (b) [47].

3.3. Dynamic mechanism of ground surface deformation

In the process of in-situ oil shale mining, ground surface deformation and ground subsidence not only affect the normal operation of downhole equipment but may also trigger environmental and geological problems [48]. By integrating the mechanical properties of rock masses and multi-field coupling effects, THM coupling simulation can quantify the laws of ground surface deformation and reveal the intrinsic mechanism of deformation, which provides core support for engineering risk prevention and control and the formulation of environmentally friendly mining schemes.

Zhao et al. [49] combined THM coupling simulation with practical engineering requirements. Through simulation, it was found that during horizontal well production, the fluid short-circuited along high-permeability channels, resulting in low heating efficiency in the early stage, and the uneven heating further increased the difference in bottom-hole deformation. In addition, they quantitatively analyzed the dynamic characteristics of surface deformation, providing a reference for the design of the in-situ oil shale mining process and the formulation of equipment protection schemes.

Aiming at environmental geological problems such as ground subsidence after in-situ mining of oil shale, Zhang et al. [50] innovatively combined physical experiments, theoretical analysis, and THM coupling simulation to construct a transverse anisotropy constitutive model suitable for in-situ mining deformation of oil shale, and revealed the internal mechanism of oil shale deformation under thermal action. The results show that the reservoir reaches the target temperature within 16 days, and the vertical final deformation is about 6.5 cm. The influence of in-situ mining on the geological environment is less than that of the traditional method, which provides a practical paradigm for this kind of coupling simulation in the study of heterogeneous rock mining.

Hu [51] studied ground surface deformation throughout the entire process of in-situ oil shale mining. Based on the convective heating method, FLAC3D software was used to construct the whole stratum numerical model of the Fuyu in-situ oil shale mining pilot test base. The whole process of in-situ oil shale mining was simulated using THM coupling. It was revealed that the thermal expansion and stress concentration of the rock mass near the heating well were caused by rapid heat flow in the heating stage, which promoted the surface uplift of 2.93 cm. In the cooling stage, the stress concentration of the rock mass was weakened after cooling, and the compression of the oil shale led to surface settlement of 3.52 cm.

In 2024, Song et al. [52] constructed a THM coupling model considering the dynamic changes in pore structure and in thermophysical and mechanical parameters with temperature to analyze the multi-field evolution and ground surface deformation caused by in-situ mining of oil shale. The results show that surface displacement exhibits the evolution characteristics of heating-induced uplift, cooling-induced subsidence, and steady-state stabilization, and the final stratum settlement is about 0.59 cm.

In summary, the application of THM coupling simulation in in-situ mining of oil shale has important theoretical and practical significance. Through comprehensive analysis of the interaction among the temperature field, fluid field, and stress field, THM coupling simulation clarifies the mechanism of efficient steam injection pyrolysis, accurately predicts the evolution law of the pyrolysis zone under different fracture systems, as well as quantitatively reveals the formation deformation caused by in-situ oil shale mining, providing critical theoretical support and a decision-making basis for the implementation of efficient, safe, and environmentally friendly in-situ mining of oil shale. The application of THM coupling simulation is summarized in this paper, as shown in Table 1. Currently, with advances in model refinement, full multi-field coupling, and multi-scale characterization technologies, THM coupling simulation is gradually expanding to full THMC simulation to more comprehensively depict the interaction mechanisms between chemical processes such as pyrolysis kinetics, product generation, and migration and physical fields. This has further enhanced the predictability and controllability of oil shale exploitation under complex geological conditions, advancing oil shale resource development toward a safer, more efficient, and environmentally friendly model.

Table 1. Summary of applications of THM coupling simulation in oil shale

Direction of application	Core objective	Main conclusion
Simulation and optimization of in-situ heat injection mining	Accurate simulation of the oil shale pyrolysis process and improvement of pyrolysis efficiency	Steam pyrolysis efficiency is higher than that of conduction heating, and the intrinsic correlation between anisotropy and the pore-mechanical properties of oil shale should be considered
Prediction of effective pyrolysis zone and fracture propagation	Expanding the pyrolysis range and shortening the mining cycle	Hydraulic fractures are more efficient than bedding fractures, and multi-fracture networks achieve wide-area high-temperature coverage
Dynamic mechanism of ground surface deformation	Preventing geological risks and ensuring equipment safety	Ground surface deformation is characterized by "heating uplift–cooling subsidence–steady state"

4. Conclusions

THM coupling simulation quantifies the coupling effects of temperature, seepage, and stress fields, revealing the core mechanisms of in-situ oil shale exploitation. It delivers key theoretical support for optimizing mining parameters, risk mitigation, and engineering design, with its application value fully demonstrated in heat injection efficiency improvement, effective pyrolysis zone prediction, and ground surface deformation analysis.

1. Oil shale pyrolysis efficiency depends on the synergy of temperature transfer, fracture development, and fluid migration: the temperature field initiates pyrolysis, the stress field controls fracture propagation, the seepage field affects heat and product transport, and their dynamic balance is key to efficient exploitation.
2. Accurate prediction of the effective pyrolysis zone requires centering on the 400 °C pyrolysis temperature threshold and integrating fracture morphological characteristics. Hydraulic fractures can significantly shorten the pyrolysis cycle compared with parallel bedding fractures,

while multi-fracture networks enable broader high-temperature coverage than single fractures.

3. The dynamic evolution of surface deformation can be predicted in advance via coupling simulation, exhibiting the intrinsic characteristics of heating-induced uplift, cooling-induced subsidence, and steady-state stabilization. Moreover, in-situ mining causes less disturbance to the geological environment than traditional mining technologies.

Currently, THM coupling simulation still has limitations. First, the full THMC coupling mechanism is not fully clarified, with insufficient deep integration of chemical processes and physical fields. Second, simulation parameters lack adequate matching with field operating conditions, compromising the accuracy of engineering guidance.

Future research should prioritize developing THMC models and strengthening the coupling of multi-scale reservoir heterogeneity with pyrolysis kinetics. Meanwhile, a multi-scale parameter inversion method should be established by integrating micro-CT and field monitoring data to enhance model adaptability to real reservoirs, providing comprehensive technical support for maximum oil shale resource utilization and precise mining risk control.

Data availability statement

No new data were generated or analyzed in support of this review.

Acknowledgments

Shuang Liang contributed to writing the original draft, Yi Pan contributed to funding acquisition, Mingzhe Guo contributed to supervision and proofreading, and Hui Yang contributed to investigation and formal analysis. This work was supported by the National Science Funding of China (grant No. 52574041), “Microscopic mechanism of transverse isotropic thermal damage in microwave-enhanced pyrolysis of oil shale.” The publication costs of this article were partially covered by the Estonian Academy of Sciences.

References

1. Wang, L., Gao, C.-H., Xiong, R.-Y., Zhang, X.-J., Guo, J.-X. Development review and the prospect of oil shale in-situ catalysis conversion technology. *Petroleum Science*, 2024, **21**(2), 1385–1395. https://doi.org/10.1016/j.petsci.2023.08.035
2. Mohr, S. H., Wang, J., Ellem, G., Ward, J., Giurco, D. Projection of world fossil fuels by country. *Fuel*, 2015, **141**, 120–135. https://doi.org/10.1016/j.fuel.2014.10.030

3. Ma, L., Yin, X. Y., Sun, H., Fu, B. S. Present status of oil shale resource utilization in the world and its development prospects. *Global Geology*, 2012, **31**(4), 772–777.
4. Aurela, M., Mylläri, F., Konist, A., Saarikoski, S., Olin, M., Simonen, P. et al. Chemical and physical characterization of oil shale combustion emissions in Estonia. *Atmospheric Environment: X*, 2021, **12**, 100139. https://doi.org/10.1016/j.aeaoa.2021.100139
5. Chen, B., Li, Y. L., Yuan, M. X., Shen, J., Wang, S., Tong, J. H. et al. Study of the co-pyrolysis characteristics of oil shale with wheat straw based on the hierarchical collection. *Energy*, 2022, **239**, 122144. https://doi.org/10.1016/j.energy.2021.122144
6. Kang, W.-L., Zhou, B.-B., Issakhov, M., Gabdullin, M. Advances in enhanced oil recovery technologies for low permeability reservoirs. *Petroleum Science*, 2022, **19**(4), 1622–1640. https://doi.org/10.1016/j.petsci.2022.06.010
7. Li, L. L., Zhang, F. Q. Current situation and suggestion of oil shale in-situ exploitation technology. *Chemical Engineer*, 2023, **37**(8), 71–75. https://doi.org/10.16247/j.cnki.23-1171/tq.20230871
8. Geng, Y. D., Liang, W. G., Liu, J., Cao, M. T., Kang, Z. Q. Evolution of pore and fracture structure of oil shale under high temperature and high pressure. *Energy & Fuels*, 2017, **31**(10), 10404–10413. https://doi.org/10.1021/acs.energyfuels.7b01071
9. Yang, D., Wang, L., Zhao, Y. S., Kang, Z. Q. Investigating pilot test of oil shale pyrolysis and oil and gas upgrading by water vapor injection. *Journal of Petroleum Science and Engineering*, 2021, **196**, 108101. https://doi.org/10.1016/j.petrol.2020.108101
10. Wang, L., Yang, D., Kang, Z. Q. Evolution of permeability and mesostructure of oil shale exposed to high-temperature water vapor. *Fuel*, 2021, **290**, 119786. https://doi.org/10.1016/j.fuel.2020.119786
11. Gao, C., Su, J. Z., Wang, Y. W., Meng, X. L., Wang, Y. Research progress of numerical simulation on oil shale in-situ production. *Oil Drilling & Production Technology*, 2018, **40**(3), 330–335. https://doi.org/10.13639/j.odpt.2018.03.010
12. Wang, G. Y., Yang, D., Kang, Z. Q., Lv, Y. Q. Numerical study of in-situ injecting superheated steam thermal recovery of transversely isotropic oil shale reservoir. *Taiyuan University of Technology*, 2020, **51**(1), 81–90.
13. Song, J. C., Fan, X. Y., Liu, J. J., Yin, G. Q., Zhang, X. L., Wang, Z. M. A review on thermal-hydraulic-mechanical coupling theory in the development of oil and gas reservoir. *Natural Gas and Oil*, 2022, **40**(1), 64–71. https://doi.org/10.3969/j.issn.1006-5539.2022.01.010
14. Terzaghi, K. *Theoretical Soil Mechanics*. 1943. Wiley, New York.
15. Biot, M. A. Theory of elasticity and consolidation for a porous anisotropic solid. *Journal of Applied Physics*, 1955, **26**(2), 182–185. https://doi.org/10.1063/1.1721956
16. Biot, M. A. Theory of deformation of a porous viscoelastic anisotropic solid. *Journal of Applied Physics*, 1956, **27**(5), 459–467. https://doi.org/10.1063/1.1722402

17. Rice, J. R., Cleary, M. P. Some basic stress diffusion solutions for fluid-saturated elastic porous media with compressible constituents. *Reviews of Geophysics*, 1976, **14**(2), 227–241. https://doi.org/10.1029/RG014i002p00227
18. Zienkiewicz, O. C., Shiomi, T. Dynamic behaviour of saturated porous media; the generalized Biot formulation and its numerical solution. *International Journal for Numerical and Analytical Methods in Geomechanics*, 1984, **8**(1), 71–96. https://doi.org/10.1002/nag.1610080106
19. Bear, J., Corapcioglu, M. Y. A mathematical model for consolidation in a thermoelastic aquifer due to hot water injection or pumping. *Water Resources Research*, 1981, **17**(3), 723–736. https://doi.org/10.1029/WR017i003p00723
20. Lewis, R. W., Roberts, P. J., Schrefler, B. A. Finite element modelling of two-phase heat and fluid flow in deforming porous media. *Transport in Porous Media*, 1989, **4**, 319–334. https://doi.org/10.1007/BF00165778
21. Jing, L., Tsang, C.-F., Stephansson, O. DECOVALEX – an international co-operative research project on mathematical models of coupled THM processes for safety analysis of radioactive waste repositories. *International Journal of Rock Mechanics and Mining Sciences & Geomechanics Abstracts*, 1995, **32**(5), 389–398. https://doi.org/10.1016/0148-9062(95)00031-B
22. Gutierrez, M., Makurat, A. Coupled HTM modelling of cold water injection in fractured hydrocarbon reservoirs. *International Journal of Rock Mechanics and Mining Sciences*, 1997, **34**(3–4), 113.e1–113.e15. https://doi.org/10.1016/S1365-1609(97)00140-8
23. Chai, J. R. Continuum model for coupled seepage, stress and temperature fields in rock mass. *Hongshui River*, 2003, **22**(2), 18–20.
24. Kang, Z. Q. *The Pyrolysis Characteristics and In-situ Hot Drive Simulation Research that Exploit Oil-gas of Oil Shale*. PhD thesis. Taiyuan University of Technology, China, 2008.
25. Zhao, L. M. *Properties of Oil Shale In-situ Pyrolysis and Coupling Process of Underground Coal Gasification*. PhD thesis. China University of Mining and Technology, Beijing, China, 2013.
26. Wang, G. Y. *Evolution of anisotropic thermophysical, hydraulic, mechanical characteristics under high temperature and its application*. MS thesis. Taiyuan University of Technology, China, 2019.
27. Jin, J., Jiang, W. D., Liu, J. D., Shi, J. F., Zhang, X. W., Cheng, W. et al. Numerical analysis of in situ conversion process of oil shale formation based on thermo-hydro-chemical coupled modelling. *Energies*, 2023, **16**(5), 2103. https://doi.org/10.3390/en16052103
28. Huang, H. W., Yu, H., Xu, W. L., Lyu, C. S., Micheal, M., Xu, H. Y. et al. A coupled thermo-hydro-mechanical-chemical model for production performance of oil shale reservoirs during in-situ conversion process. *Energy*, 2023, **268**, 126700. https://doi.org/10.1016/j.energy.2023.126700
29. Zamani, M. Z., Dong, Y., Samadi, F., Kamran, A., Khan, Z., Hussain, S. Flow-solid-thermal-chemical coupling model for *in-situ* extraction of oil shale using high-temperature supercritical CO_2. *Open Access Library Journal*, 2024, **11**, e11951. https://doi.org/10.4236/oalib.1111951

30. Chen, Z. J., Song, S. Y., Zhang, W., Mei, S. D., Zhang, S. Investigation of thermal-hydraulic-mechanical coupling model for in-situ transformation of oil shale considering pore structure and anisotropy. *Engineering Geology*, 2025, **344**, 107859. https://doi.org/10.1016/j.enggeo.2024.107859
31. Sun, D. W., Wang, L., Lu, Y., Yang, D., Huang, X. D., Kang, Z. Q. Three-dimensional pore structure reconstruction of heterogeneous rocks using DC-SRGAN: a case study on pore evolution in oil shale under thermal stimulation. *Energy*, 2025, **337**, 138641. https://doi.org/10.1016/j.energy.2025.138641
32. Wang, Z. M. *Reservoir Fluid-Solid-Heat Coupling Model Research and Preliminary Application*. PhD thesis. Southwest Petroleum Institute, China, 2002.
33. Wang, Z. M., Du, Z. M. Finite element method for fluid-solid-heat coupling seepage problem in reservoir. *Journal of Southwest Petroleum Institute*, 2002, **2**, 28–30, 3.
34. Li, Y., Lin, M., Zhang, S. B. Numerical model of thermal-hydrological-mechanical coupling and its application. *Chinese Journal of Hydrodynamics*, 2015, **30**(1), 56–63.
35. Kang, Z. Q., Zhao, Y. S., Yang, D., Tian, L. J., Li, X. A pilot investigation of pyrolysis from oil and gas extraction from oil shale by *in-situ* superheated steam injection. *Journal of Petroleum Science and Engineering*, 2020, **186**, 106785. https://doi.org/10.1016/j.petrol.2019.106785
36. Liu, Z. J. *Temperature Dependence of Evolution of Pore Structure and Permeability Characteristics of Oil Shale*. PhD thesis. Taiyuan University of Technology, China, 2018.
37. Wang, L., Zhao, Y. S., Yang, D. Investigation on meso-characteristics of in-situ pyrolysis of oil shale by injecting steam. *Chinese Journal of Rock Mechanics and Engineering*, 2020, **39**(8), 1634–1647.
38. Wang, G. Y., Yang, D., Kang, Z. Q., Zhao, J., Lv, Y. Q. Numerical investigation of the in situ oil shale pyrolysis process by superheated steam considering the anisotropy of the thermal, hydraulic, and mechanical characteristics of oil shale. *Energy & Fuels*, 2019, **33**(12), 12236–12250. https://doi.org/10.1021/acs.energyfuels.9b02883
39. Wang, L., Yang, D., Zhao, J., Zhao, Y. S., Kang, Z. Q. Changes in oil shale characteristics during simulated in-situ pyrolysis in superheated steam. *Oil Shale*, 2018, **35**(3), 230–241. https://doi.org/10.3176/oil.2018.3.03
40. Saif, T., Lin, Q., Bijeljic, B., Blunt, M. J. Microstructural imaging and characterization of oil shale before and after pyrolysis. *Fuel*, 2017, **197**, 562–574. https://doi.org/10.1016/j.fuel.2017.02.030
41. Saif, T., Lin, Q., Singh, K., Bijeljic, B., Blunt, M. J. Dynamic imaging of oil shale pyrolysis using synchrotron X–ray microtomography. *Geophysical Research Letters*, 2016, **43**(13), 6799–6807. https://doi.org/10.1002/2016GL069279
42. Tang, J. P., Yu, H. H., Zhang, X., Cui, H. B. Analysis on variation of effective pyrolysis zones in reservoir by in-situ heat injection production of oil shale. *Chinese Journal of Computational Mechanics*, 2023, **40**(3), 440–446. https://doi.org/10.7511/jslx20211030001
43. Yu, H. H., Tang, J. P., Zhang, X., Ren, L., Zhang, X. Analysis of effective

pyrolysis zone and heat loss in oil shale reservoir with random fractures. *ACS Omega*, 2023, **8**(48), 45687–45699.

44. Huang, X. *Numerical Simulation Study on Deformation Law of Deep Roadway Surrounding Rock Under Multi-field Coupling Effect*. Master's thesis. Henan Polytechnic University, China, 2014.
45. Lee, K. J., Moridis, G. J., Ehlig-Economides, C. A. In situ upgrading of oil shale by Steamfrac in multistage transverse fractured horizontal well system. *Energy Sources, Part A: Recovery, Utilization, and Environmental Effects*, 2016, **38**(20), 3034–3041. https://doi.org/10.1080/15567036.2015.1135209
46. Lee, K. J., Moridis, G. J., Ehlig-Economides, C. A. Compositional simulation of hydrocarbon recovery from oil shale reservoirs with diverse initial saturations of fluid phases by various thermal processes. *Energy Exploration & Exploitation*, 2017, **35**(2), 172–193. https://doi.org/10.1177/0144598716684307
47. Jia, Y. C., Huang, X. D., Yang, D., Sun, D. W., Luo, C. Thermo-hydro-mechanical coupling in oil shale: investigating permeability and heat transfer under high-temperature steam injection. *Case Studies in Thermal Engineering*, 2024, **61**, 104862. https://doi.org/10.1016/j.csite.2024.104862
48. Qiu, S. W. *Experimental Study on the Impacts of Oil Shale In-situ Pyrolysis on Groundwater Hydrochemical Characteristics*. PhD thesis. Jilin University, China, 2016.
49. Zhao, J. M., Cao, D. F., Liu, Y. M., Xing, S. F. Fluid-thermal-solid coupling simulation of oil shale in-situ pyrolysis by horizontal well pattern. *Science Technology and Industry*, 2022, **22**(1), 329–337.
50. Zhang, S., Song, S. Y., Zhang, W., Zhao, J. M., Cao, D. F., Ma, W. L. et al. Research on the inherent mechanism of rock mass deformation of oil shale in-situ mining under the condition of thermal-fluid-solid coupling. *Energy*, 2023, **280**, 128149. https://doi.org/10.1016/j.energy.2023.128149
51. Hu, Y. *Study on Spatiotemporal Evolution of Surface Deformation during In-situ Exploitation of Oil Shale*. Master's thesis. Jilin University, China, 2023.
52. Song, S. Y., Mei, S. D., Hu, Y., Li, Q., Chen, Z. J., Zhang, S. Research on the thermo-hydro-mechanical coupling simulation and deformation spatiotemporal evolution for the entire process of oil shale in-situ mining. *Engineering Geology*, 2024, **339**, 107643. https://doi.org/10.1016/j.enggeo.2024.107643

Oil Shale, 2026, 43, 3, 261–279 https://doi.org/10.3176/oil.2026.3.02

Characteristics and facies classification of oil shales in major continental basins of China

Hongbiao Wang(a,b), Duoxiao Sun(a,b), Hongliang Dang(a,b,c), Yanwei Bi(a,b), Pingchang Sun(a,b)*

(a) College of Earth Sciences, Jilin University, Changchun, Jilin 130061, China
(b) Key-Lab for Oil Shale and Paragenetic Minerals of Jilin Province, Changchun, Jilin 130061, China
(c) Qinghai Geological Survey, Xining 810000, China

Received 16 December 2025, accepted 1 July 2026, available online 3 August 2026

Abstract. *The continental oil shales of China exhibit pronounced heterogeneity in organic matter abundance, mineral composition, and sedimentary structures. Characterizing their lithofacies is therefore fundamental for reconstructing depositional environments, assessing resource potential, and guiding resource development. In this study, oil shale data from major continental basins, including the Songliao, Ordos, and Junggar basins, were compiled, with a focus on TOC, XRD-derived mineralogical compositions, and sedimentary structural information. Based on an integrated evaluation of organic geochemical and sedimentological parameters, TOC, bedding characteristics, and mineralogy were selected as key criteria for lithofacies classification. Accordingly, continental oil shales in China were subdivided into 24 lithofacies types, such as organic-rich laminated argillaceous mudstone (RLAM) and organic-poor massive siliceous mudstone (PMSM). Among them, organic-rich laminated mixed mudstone (RLMM), organic-rich laminated siliceous mudstone (RLSM), and organic-rich laminated calcareous mudstone (RLCM) are identified as the most prospective lithofacies due to their relatively high TOC contents, favorable mineralogical brittleness, and well-developed lamination, which collectively indicate superior hydrocarbon generation potential and reservoir quality.*

Keywords: *lithofacies classification, oil shale, continental basin, total organic carbon, mineral composition.*

---

* Corresponding author, sunpingchang711@126.com

1. Introduction

Oil shale is a fine-grained sedimentary rock enriched in organic matter that can generate hydrocarbons upon heating [1]. As one of the most promising unconventional energy resources [2, 3], oil shale is characterized by abundant reserves, wide geographic distribution, and substantial potential for both direct utilization and in situ conversion technologies [4–6]. Lithofacies are defined as rocks or rock assemblages formed under specific depositional environments, reflecting sedimentary processes and environmental conditions. Lithofacies analysis provides a fundamental basis for evaluating the enrichment of organic sedimentary deposits, hydrocarbon generation potential, and development feasibility [7–9]. Accordingly, establishing a lithofacies classification framework for oil shale is crucial for elucidating its depositional evolution and resource potential.

At present, oil shale is commonly regarded as an extremely organic-rich shale, and a systematic lithofacies classification scheme has not yet been established. Previous studies have primarily focused on oil shale type classification. For example, Goodarzi et al. [10] divided oil shale into coastal, shallow-water, and deep-water types, whereas Lin [11] classified the oil shale of the Qingshankou Formation in the Songliao Basin into horizontally laminated, massive, and bioclastic oil shale. Given that existing mudstone and shale classification schemes typically incorporate parameters such as mineral composition, organic matter abundance, organic matter type, sedimentary structures, and grain size [7, 12–14], these parameters provide a robust methodological foundation for oil shale lithofacies classification in this study.

Compared with marine oil shale, terrestrial oil shale in China exhibits pronounced heterogeneity, more complex material sources, and broader ranges of organic matter and mineral compositions [15]. Moreover, inconsistencies in classification criteria among different studies hinder reliable inter-basin comparisons. The establishment of a unified lithofacies classification scheme for oil shale can effectively address these limitations. In this study, datasets on the sedimentary structures, organic matter abundance indices, and mineral assemblages of oil shale from six representative basins in China (Songliao, Ordos, Junggar, Maoming, Fushun, and Qaidam) were systematically compiled. By comparatively analyzing the variations in these parameters among different basins, a lithofacies classification framework for oil shale in terrestrial basins of China is established.

2. Characteristics of oil shale

2.1. Formation ages of oil shales in representative basins

Oil shales in China's terrestrial basins were primarily deposited from the Mesozoic to the Cenozoic, developing across diverse tectonic settings, including rift basins, foreland basins, and cratonic basins, with deposition predominantly occurring in deep- to semi-deep lacustrine environments [16] (Table 1). Six representative basin oil shales were selected for this study. The Maoming and Fushun basins are small Cenozoic basins controlled by major faults, yet they host abundant oil shale resources within relatively limited areas [16, 17]. The Qingshankou Formation oil shale in the Upper Cretaceous of the Songliao Basin formed during the post-rift thermal subsidence stage [11, 18]. In the Qaidam Basin, the Shimengou Formation oil-bearing shale sequences were deposited in the late Middle Jurassic, representing a transitional phase from rifting to thermal subsidence [19]. In contrast, the Ordos Basin, a stable cratonic basin, contains oil shale in the Upper Triassic Yanchang Formation, reflecting a deep-lake depositional system developed under long-term basin stability [16]. The Lucaogou Formation oil shale in the Permian of the Junggar Basin was deposited in a terrestrial foreland basin during the molasse stage, influenced by the amalgamation of the Junggar and Tarim blocks [16]. Despite spanning a wide temporal range, these oil shales share common environmental characteristics, including rapid lake-basin subsidence, a warm and humid climate, and high lacustrine productivity, which collectively provided favorable conditions for the preservation and accumulation of abundant organic matter.

Table 1. Formation ages and depositional characteristics of oil shales in representative basins in China

Basin	Type	Representative stratigraphic unit	Formation age	Depositional environment	References
Maoming	Rift basin	Youganwo Fm	Paleogene	Semi-deep lake	[17]
Fushun	Strike-slip basin	Jijuntun Fm	Paleocene–Eocene	Semi-deep to deep lake	[16]
Songliao	Rift basin	Qingshankou Fm	Upper Cretaceous	Deep lake	[11, 18]
Qaidam	Rift basin	Shimengou Fm	Middle–Late Jurassic	Semi-deep to deep lake	[19]
Ordos	Cratonic basin	Yanchang Fm	Upper Triassic	Semi-deep to deep lake	[16]
Junggar	Foreland basin	Lucaogou Fm	Middle Permian	Semi-deep to deep lake	[16]

2.2. Sedimentary structure characteristics

A comparative analysis of sedimentary structures in oil shales from six basins reveals that China's terrestrial basin oil shales predominantly develop three structural types: laminated → bedded → massive (Fig. 1), reflecting variations in water-body stability, hydrodynamic intensity, sedimentation rate, and sediment composition. Laminated structures are particularly characteristic of deep- to semi-deep lake deposits. The upper oil shales of the Songliao, Fushun, Maoming, and Qaidam basins exhibit well-developed fine laminations (Fig. 1a, d, g, i), indicative of strong water stratification, low physical disturbance, and minimal sediment dilution [11, 16, 17, 19]. In contrast, bedded or massive structures are more frequently observed in the Ordos and Junggar basins at lake-margin locations or during periods of enhanced sediment supply,

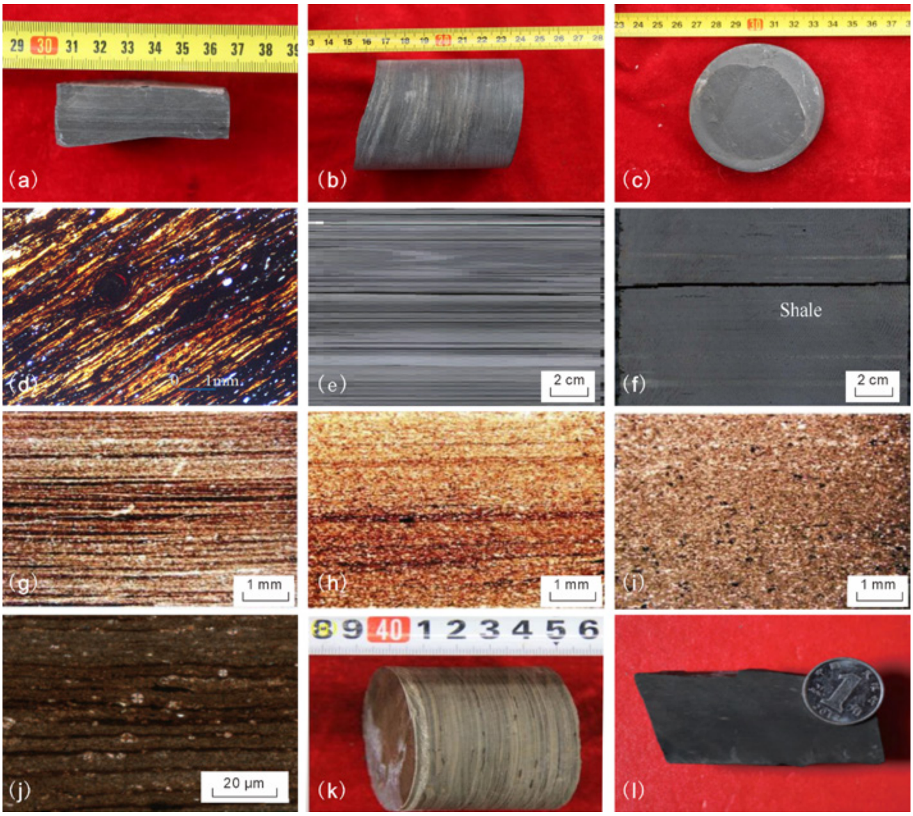

Fig. 1. Core samples and photomicrographs of oil shales [11, 18–21]. (a–c) Qingshankou Formation, Songliao Basin: oil shales displaying laminated, bedded, and massive structures, respectively; (d–f) Yanchang Formation, Ordos Basin: oil shales displaying laminated, bedded, and massive structures, respectively; (g–i) Lucaogou Formation, Junggar Basin: oil shales displaying laminated, bedded, and massive structures, respectively; (j–l) Shimengou Formation, Qaidam Basin: oil shales displaying laminated, bedded, and massive structures, respectively.

reflecting higher sedimentation rates, increased lake disturbances, and greater clastic input [20, 21]. Overall, laminated structures represent the most prevalent and defining sedimentary feature of high-quality terrestrial oil shales in China. They control rock brittleness, pore structure, and the distribution of organic matter, and their degree of development largely determines lithofacies assemblages and the potential exploitability of oil shale.

2.3. Organic matter abundance and type

Total organic carbon (TOC) of oil shales from six terrestrial basins in China generally falls within a medium- to high range (approximately 5–25%), although significant differences exist among depositional systems (Fig. 2).

Geochemical data indicate that the TOC content of the Youganwo Formation oil shales in the Maoming Basin ranges from 3.7% to 28.9%, with a mean of 13.4%. The hydrogen index (HI) varies between 332 and 1108 mg HC/g TOC, averaging 721.8 mg HC/g TOC. Organic matter is predominantly type I kerogen.

For the Jijuntun Formation oil shales in the Fushun Basin, TOC ranges from 2.3% to 30.3%, with a mean of 10.3%, and HI ranges from 102 to 699 mg HC/g TOC, averaging 475.7 mg HC/g TOC (Fig. 2). The organic matter mainly comprises type I and type II kerogen.

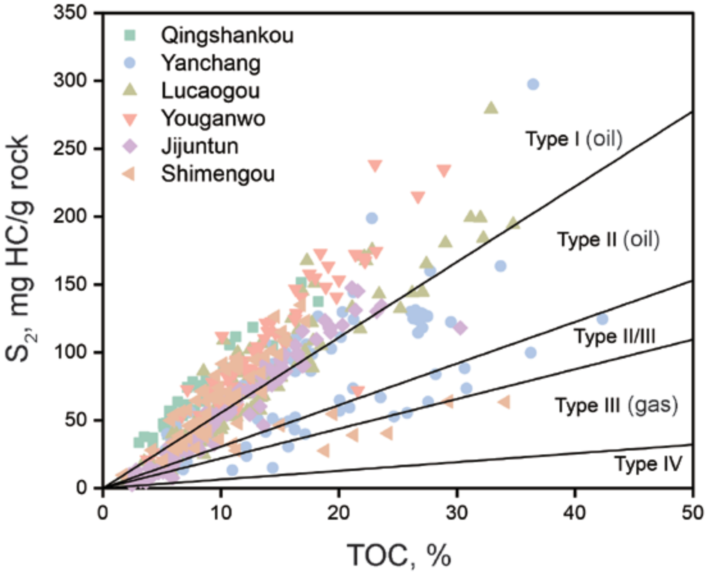

Fig. 2. TOC–S_2 cross plot for immature oil shales [48]. Qingshankou Formation data are from [49]; Yanchang Formation data are from [20, 22, 50–52]; Lucaogou Formation data are from [53]; Youganwo Formation data are from [54, 55]; Jijuntun Formation data are from [38]; Shimengou Formation data are from [56, 57].

The TOC content of the Qingshankou Formation oil shales in the Songliao Basin ranges from 4.3% to 18.3%, with an average of 7.8%. Laminated oil shales exhibit higher TOC (mean 11.3%) than bedded (5.9%) and massive (5.5%) counterparts. HI is relatively high, ranging from 362 to 1097 mg HC/g TOC, with a mean of 838.2 mg HC/g TOC (Fig. 2). Organic matter is primarily lacustrine in origin [11, 18], dominated by type I kerogen, with type II kerogen as a subordinate component.

In the Shimengou Formation of the Qaidam Basin, TOC mostly ranges from 4.2% to 29.3%, averaging 10.7%, except for a few samples with extremely high TOC (up to 34.1%). HI varies from 147 to 903 mg HC/g TOC, averaging 610.2 mg HC/g TOC. Organic matter is mainly type I and type II kerogen, with minor type III occurrences (Fig. 2).

The Yanchang Formation oil shales in the Ordos Basin display high TOC values ranging from 3.6% to 42.3%, with a mean of 19.2%. HI ranges from 103 to 871 mg HC/g TOC, averaging 437.6 mg HC/g TOC (Fig. 2). Organic matter is derived from a mixture of aquatic organisms and higher plants [22, 23], with the maceral composition dominated by vitrinite (up to 79.3%). Kerogen is predominantly type II, with minor type I.

The TOC content of the Lucaogou Formation oil shales in the Junggar Basin ranges from 3.2% to 34.8%, averaging 14.1%, with HI between 215 and 1068 mg HC/g TOC (mean 574.1 mg HC/g TOC) (Fig. 2). Organic matter is mainly lamalginite, with minor contributions from higher plant debris [21], comprising type I and type II kerogen.

Large terrestrial basins such as the Ordos and Junggar basins are generally rich in organic matter, often exceeding 10% and locally surpassing 20–30%, reflecting high productivity and good preservation in deep-lake environments. In smaller Cenozoic basins such as the Maoming and Fushun basins, strong basin confinement and rapid sedimentation allow the formation of organic-rich oil shales with a TOC content of 10–20%. Overall, China's terrestrial oil shales are dominated by type I algal- and bacterial-derived kerogen, with minor contributions of type II and type III kerogen from terrestrial higher plants at basin margins.

2.4. Mineral composition characteristics

The mineral composition of terrestrial oil shales in China exhibits clear variations related to depositional environments, but overall can be summarized as combinations of three main groups: clay minerals, siliceous minerals, and carbonate minerals [9, 14] (Fig. 3). The Songliao, Junggar, and Ordos basins received relatively strong terrigenous clastic input, resulting in generally higher quartz and feldspar contents (quartz up to 25–40%). In contrast, the Maoming and Fushun basins, characterized by strongly confined lakes and limited external input, contain higher clay mineral contents (50–75%) and relatively low quartz content. The Qaidam Basin exhibits a transition from

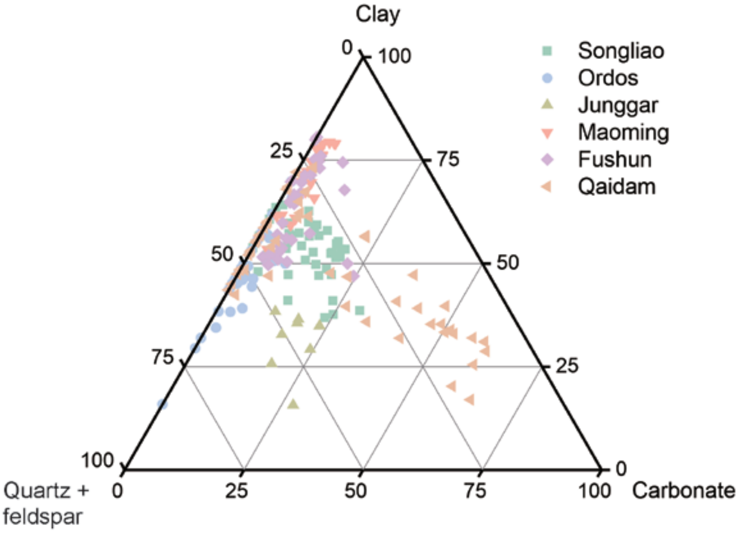

Fig. 3. Ternary diagram of mineral composition in oil shales. Songliao Basin data are from [11, 18]; Ordos Basin data are from [22, 40]; Junggar Basin data are from [58]; Maoming Basin data are from [17]; Fushun Basin data are from [38, 39]; Qaidam Basin data are from [19, 56, 57, 59, 60].

terrigenous-dominated to mixed terrigenous and autochthonous deposition (25–35%) [19].

Specifically, in the Maoming Basin, clay minerals dominate the mineral composition, ranging from 48% to 75%, with a mean of 64.9%. Siliceous minerals are relatively low, with quartz ranging from 12% to 37% (mean 22.7%) and feldspar from 0% to 4% (mean 1.9%).

For the Jijuntun Formation oil shales in the Fushun Basin, clay minerals are the most abundant (44.3–79%, mean 58.1%), followed by quartz (12–39%, mean 26.2%), with minor amounts of feldspar, calcite, and pyrite.

In the Qingshankou Formation of the Songliao Basin, siliceous minerals range from 27.0% to 47.9%, with a mean of 34.5%. Carbonate minerals are generally low, averaging around 11.1%. Some bedded and massive oil shale samples contain bioclasts such as foraminifera, which locally increase carbonate content.

In the Shimengou Formation of the Qaidam Basin, the mineral assemblage of oil shales is dominated by clay minerals, quartz, and calcite, with mean contents of 45.5%, 15.5%, and 30.4%, respectively. Mineral composition varies with oil shale quality. Lower Shimengou Formation oil shales, characterized by lower TOC content, are dominated by quartz (average 38.5%) and clay minerals (average 56.3%), whereas in the upper formation, laminated oil shales are highly developed, the carbonate content increases significantly (average 30.7%) while quartz decreases (average 14.5%), resulting in an assemblage dominated by carbonate and clay minerals.

In the Yanchang Formation of the Ordos Basin, terrigenous clastic minerals are abundant, with quartz averaging 28.7% and plagioclase averaging 12.9%. Carbonate minerals are low, averaging 1.9%, while clay minerals range from 20% to 64.7%, averaging 45.8%. Additionally, pyrite is present, reaching up to 19.3%.

In the Lucaogou Formation of the Junggar Basin, oil shale minerals are mainly siliceous and carbonate clastic minerals, with lower clay content. Quartz averages 32.7%, feldspar 15.5%, carbonate minerals 19.5%, and clay minerals 30.6%.

3. Discussion

3.1. Parameters for oil shale facies classification

Previous research [24, 25] has systematically summarized the criteria for classifying mudstone facies, identifying color, mineral composition and abundance, biological components, primary sedimentary structures, compaction and deformation features, and diagenetic structures as key parameters. Together, these constitute a multi-proxy framework for facies classification. A well-defined facies classification system is vital for understanding sedimentary processes and depositional environments and serves as an essential reference for sedimentary resource evaluation and shale oil and gas exploration [12]. Facies schemes and nomenclature should simultaneously fulfill the functions of “description,” “assessment,” and “prediction” [14]. Specifically, they should describe physical, chemical, and biological variations at scales ranging from micrometers to meters, assess primary depositional processes and mechanisms, and predict post-depositional diagenetic pathways and the evolution of overall rock properties. However, time-variant features, such as color, are unsuitable as classification parameters [14].

Considering organic geochemical data, sedimentary structures, and mineral assemblages from major oil shale basins in China, and referencing previous shale facies classification schemes [7–9], this study classifies Chinese oil shale facies using three independent criteria: organic matter abundance, sedimentary structure, and mineral composition (Fig. 4). These parameters comprehensively capture the physical and chemical characteristics of the shales, reflect depositional processes and mechanisms, and provide insight into provenance, depositional environments, and predictive diagenetic evolution.

Organic matter abundance reflects paleo-lake productivity, sedimentation rates, and redox conditions [26–28]. TOC, as the principal indicator of organic matter abundance, is a key parameter for evaluating the hydrocarbon generation potential of oil shales. Variations in TOC directly control the

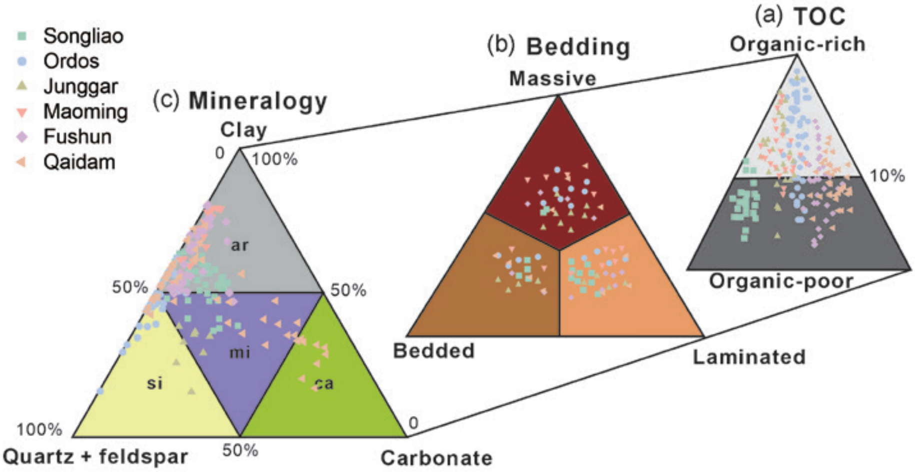

Fig. 4. Facies of oil shales are classified using a three-parameter scheme encompassing TOC content (a), bedding type (b), and mineralogy (c). Abbreviations: ar – argillaceous mudstone, mi – mixed mudstone, si – siliceous mudstone, ca – calcareous mudstone.

hydrocarbon-generating capacity of the rocks. Compared with existing TOC evaluation standards for mudstones [8], oil shales, being highly organic-rich, generally exhibit elevated TOC values. Moreover, as immature source rocks, oil shales require thermal input for efficient hydrocarbon extraction, necessitating stricter criteria in potential assessments. In China's continental basins, most oil shales display TOC values ranging from 5.8% to 24.1%, and a threshold of 10% is adopted here to distinguish between organic-rich and organic-poor shales. The TOC threshold of 10% corresponds approximately to the median–upper range of the dataset (5.8–24.1%), representing relatively organic-rich oil shale. This cutoff is also consistent with commonly adopted evaluation criteria for high-quality oil shale in previous studies.

Sedimentary structures in oil shales record abundant geological information and are essential for interpreting depositional history, resource exploration, and paleoenvironmental evolution. Laminae – defined as the smallest indivisible units of bedding with thicknesses less than 1 cm – represent the fundamental structural element [29]. Although no universally accepted theory exists for the origin of fine-grained sediment laminae [30–33], their geometry, continuity, and pattern are widely used in lithological descriptions and provide preliminary insights into primary depositional processes and mechanisms. Compared with general fine-grained sediments [34], oil shales exhibit more stable deposition, with straighter, more continuous laminae. Following previous studies [8, 35], this work quantitatively classifies sedimentary structures into three types according to lamina development: laminated (< 1 mm), bedded (1 mm–1 cm), and massive (laminae absent).

Variations in mineral composition not only reflect basin provenance, paleoclimate, and lake chemistry but also influence porosity, brittleness, and potential for exploitation [14, 34]. Minerals are categorized into three major components: siliceous, carbonate, and clay minerals. Differences in mineral assemblages affect the mechanical properties of the strata and the adsorption capacity of organic matter [36]. Using a 50% content threshold (Fig. 4c), lithology is classified into four types: argillaceous mudstone, mixed mudstone, siliceous mudstone, and calcareous mudstone.

As illustrated in Figure 4, a comprehensive classification scheme based on organic matter abundance, sedimentary structure, and mineral composition allows theoretical subdivision of oil shales in China's continental basins into 24 facies types (Table 2). In practice, however, only one to a few dominant facies typically develop in each basin. Notably, for the same stratigraphic interval, variations in burial depth and organic matter maturity across different basin regions result in significant differences in clay content and TOC, and variations in sample collection depth among studies can further affect facies determination. Therefore, this study primarily relies on data from shallowly buried, thermally immature oil shales as the basis for facies classification. The selection of predominantly shallow-buried, immature oil shale samples aims to preserve primary depositional and mineralogical characteristics, thereby minimizing thermal alteration effects and ensuring that lithofacies classification reflects original sedimentary and organic geochemical features.

Table 2. Facies types of oil shales in China's continental basins

TOC	Bedding	Mineralogy	Lithofacies
Organic-rich	Laminated	Fig. 4a	Organic-rich laminated argillaceous mudstone (RLAM)
			Organic-rich laminated mixed mudstone (RLMM)
			Organic-rich laminated siliceous mudstone (RLSM)
			Organic-rich laminated calcareous mudstone (RLCM)
	Bedded		Organic-rich bedded argillaceous mudstone (RBAM)
			Organic-rich bedded mixed mudstone (RBMM)
			Organic-rich bedded siliceous mudstone (RBSM)
			Organic-rich bedded calcareous mudstone (RBCM)
	Massive		Organic-rich massive argillaceous mudstone (RMAM)
			Organic-rich massive mixed mudstone (RMMM)
			Organic-rich massive siliceous mudstone (RMSM)
			Organic-rich massive calcareous mudstone (RMCM)

Continued on the next page

Table 2. *continued*

TOC	Bedding	Mineralogy	Lithofacies
Organic-poor	Laminated	Fig. 4a	Organic-poor laminated argillaceous mudstone (PLAM)
			Organic-poor laminated mixed mudstone (PLMM)
			Organic-poor laminated siliceous mudstone (PLSM)
			Organic-poor laminated calcareous mudstone (PLCM)
	Bedded		Organic-poor bedded argillaceous mudstone (PBAM)
			Organic-poor bedded mixed mudstone (PBMM)
			Organic-poor bedded siliceous mudstone (PBSM)
			Organic-poor bedded calcareous mudstone (PBCM)
	Massive		Organic-poor massive argillaceous mudstone (PMAM)
			Organic-poor massive mixed mudstone (PMMM)
			Organic-poor massive siliceous mudstone (PMSM)
			Organic-poor massive calcareous mudstone (PMCM)

3.2. Oil shale facies classification

Facies variations in China's lacustrine basins reflect the combined influences of paleoclimate, basin type, water column stratification, sediment supply, and lake productivity [37]. The Songliao, Fushun, and Maoming basins are predominantly characterized by laminated argillaceous mudstone facies, indicating stable water column stratification and minimal hydrodynamic disturbance during deposition [11, 17, 18, 38, 39]. In contrast, the Ordos and Junggar basins are dominated by organic-rich mixed mudstone and organic-rich siliceous mudstone facies, with elevated carbonate and siliceous mineral contents, high lake productivity, and abundant terrigenous and autochthonous sediment supply [21, 22, 40]. The Shimengou Formation in the Qaidam Basin corresponds to a Middle Jurassic transitional paleoclimate, shifting from humid to arid conditions, which influenced lake productivity, organic matter preservation, and sediment supply, thereby shaping the facies assemblage of the Shimengou oil shales [19].

Within individual basins, facies assemblages follow discernible patterns. The Qingshankou Formation in the Songliao Basin develops organic-rich laminated argillaceous mudstone (RLAM), organic-rich bedded argillaceous mudstone (RBAM), organic-rich laminated mixed mudstone (RLMM), organic-poor laminated argillaceous mudstone (PLAM), organic-poor bedded argillaceous mudstone (PBAM), organic-poor massive argillaceous mudstone (PMAM), organic-poor laminated mixed mudstone (PLMM), organic-poor bedded mixed mudstone (PBMM), and organic-poor massive mixed mudstone (PMMM) facies. In the Ordos Basin, facies include RLAM, organic-rich laminated siliceous mudstone (RLSM), RBAM, organic-rich bedded siliceous mudstone (RBSM), organic-rich massive argillaceous mudstone (RMAM), organic-rich massive siliceous mudstone (RMSM), and organic-poor massive siliceous mudstone (PMSM). The Permian oil shales of the Junggar Basin display a broader diversity, including RLSM, RLMM, RBSM, organic-rich bedded mixed mudstone (RBMM), RMSM, organic-rich massive mixed mudstone (RMMM), organic-poor laminated siliceous mudstone (PLSM), PLMM, organic-poor bedded siliceous mudstone (PBSM), PBMM, PMSM, and PMMM. The Fushun and Maoming basins show similar assemblages, with RLAM, RBAM, RMAM, PLAM, PBAM, and PMAM facies. The Qaidam Basin exhibits the highest facies diversity, encompassing nearly all oil shale types, with RLAM, organic-rich laminated calcareous mudstone (RLCM), RLMM, PBSM, PBAM, PMSM, and PMAM being particularly common.

3.3. Implications of facies for hydrocarbon generation and resource assessment

Facies serve as a critical link connecting depositional processes, organic matter accumulation, and the hydrocarbon generation potential of lacustrine oil shales [41]. Variations in facies not only reflect differences in depositional environments and organic matter input but also govern the hydrocarbon generation, expulsion, and in-situ transformation potential of oil shale sequences [42]. Essentially, each facies represents a distinct “organic matter–mineral–porosity” system [42].

Identifying organic-rich facies with well-developed lamination and high brittleness indices is particularly critical for assessing hydrocarbon potential and producibility. Laminated facies, which form under low depositional rates, typically exhibit elevated TOC values [41] and favor the development of interlayer microfractures [43]. Rigid components, including siliceous and carbonate minerals, enhance compaction resistance, thereby promoting the formation and preservation of intergranular porosity [44], whereas clay minerals are generally inversely correlated with porosity development. During in-situ transformation, organic acids released from the thermal maturation of organic matter can dissolve carbonate and feldspar minerals [45], further improving reservoir properties.

The brittleness index (BI) is defined as the weight fraction of siliceous plus carbonate minerals relative to the total mineral content (siliceous + carbonate + clay minerals) [46]. Rocks with BI $> 60\%$ exhibit brittle behavior, whereas those with BI $< 60\%$ display ductility [36, 47]. Consequently, organic-rich laminated facies with high BI constitute the most promising oil shale targets.

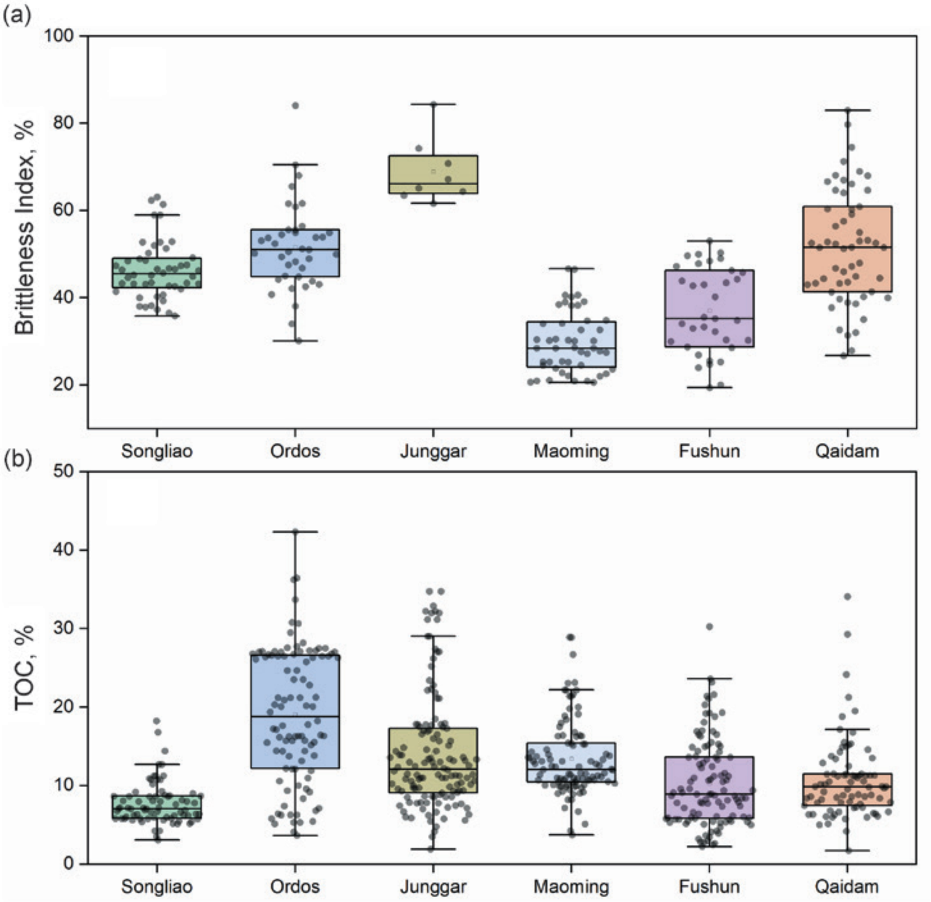

Fig. 5. Distribution of brittleness index (a) and TOC content (b) for oil shales from different basins. The upper and lower boundaries of the boxes represent the 75th and 25th percentiles, respectively.

At the facies scale, RLMM, RLSM, and RLCM represent the most favorable "sweet spots" within basins. At the basin scale, the Junggar Basin stands out with the highest brittle mineral content (BI = 68.9%) and relatively high TOC content (average 14.14%) (Fig. 5). Furthermore, the Lucaogou Formation oil shales in the Junggar Basin are hydrogen-rich, with HI values reaching 574.1 mg/g TOC, marking it as the basin with the greatest oil shale exploitation potential.

4. Conclusions

This study presents an oil shale facies classification scheme tailored for lacustrine basins in China, based on organic geochemical parameters, mineralogical composition, and depositional structures of oil shales from six major basins (Songliao, Ordos, Junggar, Maoming, Fushun, and Qaidam). Systematic basin-scale comparisons were also conducted. The main findings are summarized as follows:

1. By integrating three key parameters – TOC content, depositional structure, and mineralogical composition – 24 operationally practical lacustrine oil shale facies were delineated. This classification effectively captures geological processes such as paleo-productivity, depositional conditions, and sediment provenance, exhibiting strong applicability and comparability across different basins.
2. Analysis of the oil shale characteristics across these basins indicates that the organic-rich laminated mixed mudstone (RLMM), organic-rich laminated siliceous mudstone (RLSM), and organic-rich laminated calcareous mudstone (RLCM) facies represent the most favorable "sweet spots" for in-situ hydrocarbon generation. Basin-scale comparisons further highlight the Junggar Basin as possessing oil shales with the highest development potential.

Data availability statement

The data that support the findings of this study are available from the corresponding author upon reasonable request.

Acknowledgments

This work was supported by the Oil & Gas Major Project (grant No. 2025ZD1400803) and the National Natural Science Foundation of China (grant No. 42372125). The authors gratefully acknowledge the Editorial Board and the anonymous reviewers for their constructive comments, which have significantly improved the quality of this manuscript. We also thank Ms. Kadri Põdra for her assistance during the editorial process. The publication costs of this article were partially covered by the Estonian Academy of Publishers.

References

1. Liu, Z.-J., Meng, Q.-T., Jia, J.-L. Key methods and technologies in the study of oil shale mineralization. *Journal of Palaeogeography*, 2019, **21**(1), 127–142.
2. Dyni, J. R. Geology and resources of some world oil-shale deposits. *Oil Shale*, 2003, **20**(3), 193–252. https://doi.org/10.3176/oil.2003.3.02

3. Na, J. G., Im, C. H., Chung, S. H., Lee, K. B. Effect of oil shale retorting temperature on shale oil yield and properties. *Fuel*, 2012, **95**, 131–135. https://doi.org/10.1016/j.fuel.2011.11.029
4. Yang, Q., Guo, W., Xu, S., Zhu, C. The autothermic pyrolysis in-situ conversion process for oil shale recovery: effect of gas injection parameters. *Energy*, 2023, **283**, 129134. https://doi.org/10.1016/j.energy.2023.129134
5. Wang, H., Niu, D., Luan, Z., Dang, H., Pan, X., Sun, P. Kinetic characteristics of secondary hydrocarbon generation from oil shale and coal at different maturation stages: insights from open-system pyrolysis. *International Journal of Coal Geology*, 2025, **308**, 104845. https://doi.org/10.1016/j.coal.2025.104845
6. Gavrilova, O., Vilu, R., Vallner, L. A life cycle environmental impact assessment of oil shale produced and consumed in Estonia. *Resources, Conservation and Recycling*, 2010, **55**(2), 232–245. https://doi.org/10.1016/j.resconrec.2010.09.013
7. Liu, B., Shi, J., Fu, X., Lyu, Y., Sun, X., Gong, L. et al. Petrological characteristics and shale oil enrichment of lacustrine fine-grained sedimentary system: a case study of organic-rich shale in first member of Cretaceous Qingshankou Formation in Gulong Sag, Songliao Basin, NE China. *Petroleum Exploration and Development*, 2018, **45**(5), 884–894. https://doi.org/10.1016/S1876-3804(18)30091-0
8. Wang, Y., Wang, X., Song, G., Liu, H., Zhu, D., Zhu, D. et al. Genetic connection between mud shale lithofacies and shale oil enrichment in Jiyang Depression, Bohai Bay Basin. *Petroleum Exploration and Development*, 2016, **43**(5), 759–768. https://doi.org/10.1016/S1876-3804(16)30091-X
9. Liu, Z., Liu, G., Hu, Z., Feng, D., Zhu, T., Bian, R. et al. Lithofacies types and assemblage features of continental shale strata and their implications for shale gas exploration: a case study of the Middle and Lower Jurassic strata in the Sichuan Basin. *Natural Gas Industry B*, 2020, **7**(4), 358–369. https://doi.org/10.1016/j.ngib.2019.12.004
10. Goodarzi, F., Gentzis, T., Sanei, H., Pedersen, P. K. Elemental composition and organic petrology of a Lower Carboniferous-age freshwater oil shale in Nova Scotia, Canada. *ACS Omega*, 2019, **4**(24), 20773–20786. https://doi.org/10.1021/acsomega.9b03227
11. Shen, L. *Characteristics and Prediction of Deep Oil Shale in the Upper Cretaceous Qingshankou Formation in the Southern Songliao Basin*. Master's thesis. Jilin University, China, 2020.
12. Liu, B., Wang, H., Fu, X., Bai, Y., Bai, L., Jia, M. et al. Lithofacies and depositional setting of a highly prospective lacustrine shale oil succession from the Upper Cretaceous Qingshankou Formation in the Gulong sag, northern Songliao Basin, northeast China. *AAPG Bulletin*, 2019, **103**(2), 405–432. https://doi.org/10.1306/08031817416
13. Tang, X., Jiang, Z., Huang, H., Jiang, S., Yang, L., Xiong, F. et al. Lithofacies characteristics and its effect on gas storage of the Silurian Longmaxi marine shale in the southeast Sichuan Basin, China. *Journal of Natural Gas Science and Engineering*, 2016, **28**, 338–346. https://doi.org/10.1016/j.jngse.2015.12.026

14. Peng, J., Hu, Z., Feng, D. The classification scheme for fine-grained sedimentary rocks: a review and a new approach based on five inherent rock attributes. *Gondwana Research*, 2025, **145**, 107–141. https://doi.org/10.1016/j.gr.2025.04.014
15. Huang, C., Zhang, J., Hua, W., Yue, J., Lu, Y. Sedimentology and lithofacies of lacustrine shale: a case study from the Dongpu sag, Bohai Bay Basin, eastern China. *Journal of Natural Gas Science and Engineering*, 2018, **60**, 174–189. https://doi.org/10.1016/j.jngse.2018.10.014
16. Liu, Z., Liu, R., Sun, P., Meng, Q., Hu, F. Oil shale characteristics and distribution in typical basins of China. *Journal of Jilin University (Earth Science Edition)*, 2020, **50**(2), 313–325. https://doi.org/10.13278/j.cnki.jjuese.20200017
17. Xu, C. *Geochemical Characteristics of Oil Shale in Youganwo Formation and its Aggregation Factors of Organic Matter, Maoming Basin*. Master's thesis. Jilin University, China, 2018.
18. Zhang, S. *Characteristics and Difference Analysis of Oil Shale in the First Member of Qingshankou Formation of Upper Cretaceous in Songliao Basin*. Master's thesis. Jilin University, China, 2021.
19. Xie, W. *Late Middle Jurassic Paleoclimate and Paleoenvironmental Evolution and Organic Matter Accumulation Mechanism, Qaidam Basin*. PhD thesis. Central South University, China, 2023.
20. Yunlai, B., Yuhu, M. Geology of the Chang 7 Member oil shale of the Yanchang Formation of the Ordos Basin in central north China. *Petroleum Geoscience*, 2020, **26**(2), 355–371. https://doi.org/10.1144/petgeo2018-091
21. Gao, Y. *Organic Geochemical Characteristics and its Paleoenvironmental Significance of the Middle Permian Oil Shale in the Southern Junggar Basin*. Master's thesis. Heibei GEO University, China, 2016.
22. Li, D., Li, R., Zhu, Z., Wu, X., Cheng, J., Liu, F. et al. Origin of organic matter and paleo-sedimentary environment reconstruction of the Triassic oil shale in Tongchuan City, southern Ordos Basin (China). *Fuel*, 2017, **208**, 223–235. https://doi.org/10.1016/j.fuel.2017.07.008
23. Li, D., Li, R., Zhu, Z., Wu, X., Liu, F., Zhao, B. et al. Elemental characteristics and paleoenvironment reconstruction: a case study of the Triassic lacustrine Zhangjiatan oil shale, southern Ordos Basin, China. *Acta Geochimica*, 2018, **37**(1), 134–150. https://doi.org/10.1007/s11631-017-0193-z
24. Potter, P. E., Maynard, J. B., Depetris, P. J. *Mud and Mudstones: Introduction and Overview*. Springer, Berlin, Heidelberg, 2005. https://doi.org/10.1007/b138571
25. Potter, P. E., Maynard, J. B., Pryor, W. A. *Sedimentology of Shale*. Springer New York, New York, NY, 1980. https://doi.org/10.1007/978-1-4612-9981-3
26. Calvert, S. E., Pedersen, T. F. Geochemistry of recent oxic and anoxic marine sediments: implications for the geological record. *Marine Geology*, 1993, **113**(1–2), 67–88. https://doi.org/10.1016/0025-3227(93)90150-T
27. Tyson, R. V. Sedimentation rate, dilution, preservation and total organic carbon: some results of a modelling study. *Organic Geochemistry*, 2001, **32**(2), 333–339. https://doi.org/10.1016/S0146-6380(00)00161-3

28. Horsfield, B., Curry, D. J., Bohacs, K., Littke, R., Rullkötter, J., Schenk, H. J. et al. Organic geochemistry of freshwater and alkaline lacustrine sediments in the Green River Formation of the Washakie Basin, Wyoming, U.S.A. *Organic Geochemistry*, 1994, **22**(3–5), 415–440. https://doi.org/10.1016/0146-6380(94)90117-1
29. Campbell, C. V. Lamina, laminaset, bed and bedset. *Sedimentology*, 1967, **8**(1), 7–26. https://doi.org/10.1111/j.1365-3091.1967.tb01301.x
30. Schimmelmann, A., Lange, C. B., Schieber, J., Francus, P., Ojala, A. E. K., Zolitschka, B. Varves in marine sediments: a review. *Earth-Science Reviews*, 2016, **159**, 215–246. https://doi.org/10.1016/j.earscirev.2016.04.009
31. Schieber, J., Southard, J., Thaisen, K. Accretion of mudstone beds from migrating floccule ripples. *Science*, 2007, **318**(5857), 1760–1763. https://doi.org/10.1126/science.1147001
32. Schieber, J. Experimental testing of the transport-durability of shale lithics and its implications for interpreting the rock record. *Sedimentary Geology*, 2016, **331**, 162–169. https://doi.org/10.1016/j.sedgeo.2015.11.006
33. Shinn, E. A., Steinen, R. P., Dill, R. F., Major, R. Lime-mud layers in high-energy tidal channels: a record of hurricane deposition. *Geology*, 1993, **21**(7), 603–606. https://doi.org/10.1130/0091-7613(1993)021<0603:LMLIHE>2.3.CO;2
34. Lazar, O. R., Bohacs, K. M., Macquaker, J. H. S., Schieber, J., Demko, T. M. Capturing key attributes of fine-grained sedimentary rocks in outcrops, cores, and thin sections: nomenclature and description guidelines. *Journal of Sedimentary Research*, 2015, **85**(3), 230–246. https://doi.org/10.2110/jsr.2015.11
35. Dong, L., Li, Y., Wang, D., Liu, H., Song, G., Li, Z. et al. The classification and significance of fine-grained deposits of micro-laminae rich in unconventional oil and gas resources. *Frontiers of Earth Science*, 2022, **16**(3), 635–656. https://doi.org/10.1007/s11707-021-0955-0
36. Wang, G., Carr, T. R. Methodology of organic-rich shale lithofacies identification and prediction: a case study from Marcellus Shale in the Appalachian basin. *Computers & Geosciences*, 2012, **49**, 151–163. https://doi.org/10.1016/j.cageo.2012.07.011
37. Chen, Z., Li, X., Chen, H., Duan, Z., Qiu, Z., Zhou, X. et al. The characteristics of lithofacies and depositional model of fine-grained sedimentary rocks in the Ordos Basin, China. *Energies*, 2023, **16**(5), 2390. https://doi.org/10.3390/en16052390
38. Strobl, S. A. I., Sachsenhofer, R. F., Bechtel, A., Gratzer, R., Gross, D., Bokhari, S. N. H. et al. Depositional environment of oil shale within the Eocene Jijuntun Formation in the Fushun Basin (NE China). *Marine and Petroleum Geology*, 2014, **56**, 166–183. https://doi.org/10.1016/j.marpetgeo.2014.04.011
39. Wang, L., Lu, Y., Chen, G., Xue, L., Zhang, Z., Wang, S. et al. Greenhouse gas emissions during oil shale crushing and its main controlling factors: a contrast study of oil shale in Yaojie and Fushun areas, China. *ACS Omega*, 2024, **9**(15), 17491–17505. https://doi.org/10.1021/acsomega.4c00435
40. Li, S., Zhu, R.-K., Cui, J.-W., Luo, Z., Cui, J.-G., Liu, H. et al. The petrological characteristics and significance of organic-rich shale in the Chang 7 member

of the Yanchang Formation, south margin of the Ordos basin, central China. *Petroleum Science*, 2019, **16**(6), 1255–1269. https://doi.org/10.1007/s12182-019-00386-0

41. Sun, N., Chen, T., Gao, J., Zhong, J., Huo, Z., Qu, J. Lithofacies and reservoir characteristics of saline lacustrine fine-grained sedimentary rocks in the northern Dongpu Sag, Bohai Bay Basin: implications for shale oil exploration. *Journal of Asian Earth Sciences*, 2023, **252**, 105686. https://doi.org/10.1016/j.jseaes.2023.105686
42. Liang, C., Wu, J., Cao, Y., Liu, K., Khan, D. Storage space development and hydrocarbon occurrence model controlled by lithofacies in the Eocene Jiyang Sub-basin, East China: significance for shale oil reservoir formation. *Journal of Petroleum Science and Engineering*, 2022, **215**, 110631. https://doi.org/10.1016/j.petrol.2022.110631
43. Xin, B., Zhao, X., Hao, F., Jin, F., Pu, X., Han, W. et al. Laminae characteristics of lacustrine shales from the Paleogene Kongdian Formation in the Cangdong Sag, Bohai Bay Basin, China: why do laminated shales have better reservoir physical properties? *International Journal of Coal Geology*, 2022, **260**, 104056. https://doi.org/10.1016/j.coal.2022.104056
44. Espitalie, J., Madec, M., Tissot, B. Role of mineral matrix in kerogen pyrolysis: influence on petroleum generation and migration. *AAPG Bulletin*, 1980, **64**(1), 59–66. https://doi.org/10.1306/2F918928-16CE-11D7-8645000102C1865D
45. Surdam, R. C., Crossey, L. J., Hagen, E. S., Heasler, H. P. Organic-inorganic interactions and sandstone diagenesis. *AAPG Bulletin*, 1989, **73**(1), 1–23. https://doi.org/10.1306/703C9AD7-1707-11D7-8645000102C1865D
46. Jin, X., Shah, S., Truax, J., Roegiers, J.-C. A practical petrophysical approach for brittleness prediction from porosity and sonic logging in shale reservoirs. In *SPE Annual Technical Conference and Exhibition*, October 2014, Amsterdam. SPE-170972-MS. https://doi.org/10.2118/170972-MS
47. Jarvie, D. M., Hill, R. J., Ruble, T. E., Pollastro, R. M. Unconventional shale-gas systems: the Mississippian Barnett Shale of north-central Texas as one model for thermogenic shale-gas assessment. *AAPG Bulletin*, 2007, **91**(4), 475–499. https://doi.org/10.1306/12190606068
48. Garry, P., Atta-Peters, D., Achaegakwo, C. Source-rock potential of the lower cretaceous sediments in SD - 1X well, offshore Tano Basin, south western Ghana. *Petroleum and Coal*, 2016, **58**(4), 476–489.
49. Feng, Z., Fang, W., Wang, X., Huang, C., Huo, Q., Zhang, J. et al. Microfossils and molecular records in oil shales of the Songliao Basin and implications for paleo-depositional environment. *Science in China Series D: Earth Sciences*, 2009, **52**(10), 1559–1571. https://doi.org/10.1007/s11430-009-0121-0
50. Chen, Y., Zhu, Z., Zhang, L. Control actions of sedimentary environments and sedimentation rates on lacustrine oil shale distribution, an example of the oil shale in the Upper Triassic Yanchang Formation, southeastern Ordos Basin (NW China). *Marine and Petroleum Geology*, 2019, **102**, 508–520. https://doi.org/10.1016/j.marpetgeo.2019.01.006

51. Gao, B., Wu, X., Zhang, Y., Chen, X., Bian, R., Li, Q. Hydrocarbon generation and evolution characteristics of Triassic Zhangjiatan oil shale in southern Ordos Basin. *Petroleum Geology & Experiment*, 2022, **44**(1), 24–32. https://doi.org/10.11781/sysydz202201024
52. Ma, W., Hou, L., Luo, X., Liu, J., Tao, S., Guan, P. et al. Generation and expulsion process of the Chang 7 oil shale in the Ordos Basin based on temperature-based semi-open pyrolysis: implications for in-situ conversion process. *Journal of Petroleum Science and Engineering*, 2020, **190**, 107035. https://doi.org/10.1016/j.petrol.2020.107035
53. Tao, S., Wang, Y., Tang, D., Wu, D., Xu, H., He, W. Organic petrology of Fukang Permian Lucaogou Formation oil shales at the northern foot of Bogda Mountain, Junggar Basin, China. *International Journal of Coal Geology*, 2012, **99**, 27–34. https://doi.org/10.1016/j.coal.2012.05.001
54. Xu, C., Hu, F., Meng, Q., Liu, Z., Shan, X., Zeng, W. et al. Organic matter accumulation in the Youganwo Formation (middle Eocene), Maoming Basin, South China: constraints from multiple geochemical proxies and organic petrology. *ACS Earth and Space Chemistry*, 2022, **6**(3), 714–732. https://doi.org/10.1021/acsearthspacechem.1c00383
55. Zhao, D.-F., Guo, Y.-H., Wang, G., Zhou, X.-Q., Zhou, Y.-Y., Zhang, J.-M. et al. Organic matter enrichment mechanism of Youganwo Formation oil shale in the Maoming Basin. *Heliyon*, 2023, **9**(2), e13173. https://doi.org/10.1016/j.heliyon.2023.e13173
56. Bai, Y.-Y., Xie, W.-Q., Liu, Z.-J., Xu, Y.-B. Formation and evolution mechanisms of coal and oil shale from the Middle Jurassic Shimengou Formation, northern Qaidam Basin, China. *Ore Geology Reviews*, 2022, **151**, 105206. https://doi.org/10.1016/j.oregeorev.2022.105206
57. Bai, Y., Liu, Z., George, S. C., Meng, J. A comparative study of different quality oil shales developed in the Middle Jurassic Shimengou Formation, Yuqia area, northern Qaidam Basin, China. *Energies*, 2022, **15**(3), 1231. https://doi.org/10.3390/en15031231
58. Pang, H., Pang, X., Dong, L., Zhao, X. Factors impacting on oil retention in lacustrine shale: Permian Lucaogou Formation in Jimusaer Depression, Junggar Basin. *Journal of Petroleum Science and Engineering*, 2018, **163**, 79–90. https://doi.org/10.1016/j.petrol.2017.12.080
59. Li, L., Liu, Z., George, S. C., Sun, P., Xu, Y., Meng, Q. et al. Lake evolution and its influence on the formation of oil shales in the Middle Jurassic Shimengou Formation in the Tuanyushan area, Qaidam Basin, NW China. *Geochemistry*, 2019, **79**(1), 162–177. https://doi.org/10.1016/j.geoch.2018.12.006
60. Guo, W., Chen, G., Li, Y., Li, Y., Zhang, Y., Zhou, J. et al. Factors controlling the lower radioactivity and its relation with higher organic matter content for middle Jurassic oil shale in Yuqia depression, northern Qaidam Basin, China: evidence from organic and inorganic geochemistry. *ACS Omega*, 2021, **6**(11), 7360–7373. https://doi.org/10.1021/acsomega.0c05618

Oil Shale, 2026, 43, 3, 280–299 https://doi.org/10.3176/oil.2026.3.03

Well pattern-controlled heat transfer in in-situ oil shale conversion: a review of numerical modeling

Yu Cao[(a)], Yi Pan[(a)]*, Shuangchun Yang[(a)], Hui Yang[(b)]

(a) College of Petroleum and Natural Gas Engineering, Liaoning Petrochemical University, Liaoning 113001, China
(b) Kunlun Safety & Health (Beijing) Technology Co. Ltd, Beijing 102200, China

Received 20 October 2025, accepted 1 July 2026, available online 3 August 2026

Abstract. *As an important alternative to conventional oil and gas resources, oil shale holds significant strategic importance. While in-situ conversion technology has addressed the challenges of deep oil shale mining, heat transfer efficiency remains the core bottleneck for its large-scale application. Through a systematic review of heat transfer simulation studies on oil shale in-situ conversion under well pattern control, this paper fills existing research gaps. It first systematically reviews the current research status of heat transfer during oil shale in-situ conversion, then clarifies the heat transfer mechanisms, and finally elaborates on the thermal-hydraulic-mechanical coupling model and research progress in in-situ extraction under well pattern control. It provides theoretical support for well pattern design and efficient mining in oil shale in-situ conversion projects.*

Keywords: *oil shale, well pattern, heat transfer characteristics, thermal-fluid-solid coupling, numerical simulation.*

1. Introduction

Global oil shale resources are extremely abundant, estimated at approximately 1×10^{13} t, equivalent to 4.5×10^{11} t of shale oil, which is four times the reserves of conventional petroleum resources [1]. Oil shale is a high-ash sedimentary rock rich in organic matter, from which shale oil produced by kerogen pyrolysis can be directly used as fuel or further processed to produce gasoline, diesel, and other fuels [2]. As an important alternative energy source, oil shale has attracted worldwide attention due to its vast reserves and comprehensive utilization value [3].

In-situ oil shale conversion technology still has certain limitations and drawbacks [4]. Generally, conduction heating is relatively mature in its

---

* Corresponding author, panyi_beijing@163.com

process, simple, and easy to control, but it requires prolonged heating time and incurs high costs. Convection heating offers high heating efficiency, yet it results in significant heat loss and environmental damage. Radiation heating provides rapid heating rates; however, its heating range is constrained by technical limitations and remains in the research and development stage [5]. Reactive heating exhibits high efficiency and low cost, but its control process is complex. The in-situ pyrolysis of oil shale and hydrocarbon migration are influenced by multiple factors, making efficient heating a key challenge in the study of in-situ conversion technology [6]. Therefore, it is essential to clarify the heat transfer characteristics of oil shale under in-situ conversion conditions to provide a theoretical basis for the in-situ conversion process [7].

At present, a large number of scholars have studied the in-situ conversion technology of oil shale [8–10]. Based on the Web of Science database, a total of 726 articles from the past five years were analyzed using the search terms *oil shale*, *in situ conversion*, and *heat transfer*. As shown in Figure 1, recent research on in-situ pyrolysis of oil shale has primarily focused on fundamental mechanisms of oil shale pyrolysis, in-situ conversion technologies and reservoir engineering, and co-conversion techniques of oil shale. However, the heat transfer issue in in-situ oil shale conversion remains a critical bottleneck hindering its large-scale commercialization [11, 12]. Currently, there is a lack of comprehensive literature reviewing numerical simulation techniques for heat transfer in in-situ oil shale conversion under well pattern regulation. This paper fills the gap in literature.

This paper first describes the heat transfer characteristics of oil shale in-situ mining. Then, the solid heat transfer theory of oil shale in-situ conversion fluid is expounded, and the commonly used simulation software and thermal-fluid-solid coupling are introduced. Finally, the role of well pattern control in in-situ mining of oil shale is analyzed, the influence of well pattern on mining is discussed, and the numerical simulation and optimization directions of different well pattern models are discussed. The paper provides theoretical support and effective insights for the in-situ conversion development of oil shale and the optimization of well pattern deployment.

2. Current research status of in-situ heat transfer in oil shale conversion

The key issue in the in-situ exploitation of oil shale lies in how external temperature can heat the ore layer to the effective pyrolysis temperature, which is essentially a matter of heat transfer characteristics. However, the underground environment is extremely complex, and different bedding structures may significantly affect the heat transfer characteristics of oil shale [13]. Heat conduction in an object occurs under the condition of no macroscopic relative displacement, where energy is transferred in the form of

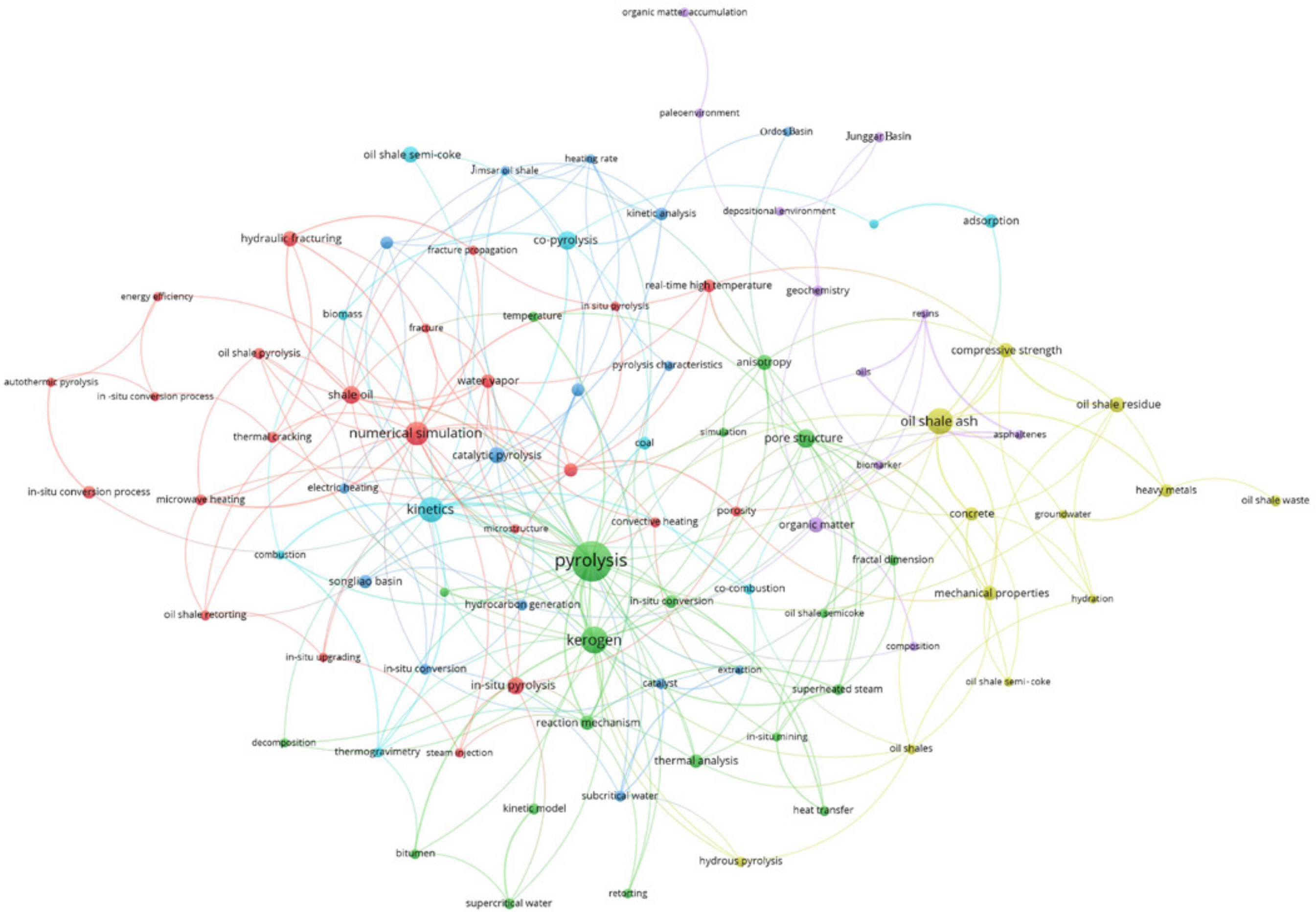

Fig. 1. Visualization analysis of keyword co-occurrence in heat transfer research on in-situ conversion of oil shale over the past five years.

internal energy through the thermal motion of molecules or atoms constituting the object [14]. Convective heat transfer refers to the process of heat transfer that occurs when fluids of different temperatures undergo overall or partial relative movement. When an object's temperature is above absolute zero, the thermal motion of atoms and molecules continuously emits electromagnetic waves, releasing energy [15]. For heat transfer via conduction or convection, the presence of a medium is necessary, whereas radiative heat transfer can occur in a vacuum without requiring any medium [16].

Oil shale is a poor thermal conductor with low thermal conductivity, and it is a porous solid with relatively low porosity. Therefore, heat transfer issues inevitably arise during pyrolysis [17, 18]. These heat transfer mechanisms interact and overlap, making it highly challenging to comprehensively study the heat transfer behavior of oil shale during in-situ conversion process.

Regarding the key equipment for in-situ oil shale conversion, the large-scale spiral baffle downhole heater, Bu et al. [19] conducted numerical heat transfer simulations to analyze its performance under different heating powers and injected gas flow rates. At a gas flow rate of 160 m^3/h and a heating power of 6 kW, the outlet temperature reached 280 °C. When $h/\Delta p^{1/3}$ was used as the heat transfer performance indicator, the performance was optimal at 100 m^3/h, most stable at 160 m^3/h, and significantly affected by heating power at 200 m^3/h, being approximately 6% lower than that at 100 m^3/h. Gas heating was divided into three stages: rapid heating, stable heating, and excessive heating. The outlet temperature curve exhibited a two-stage variation due to the energy exchange balance between heating power and gas flow rate, preventing the outlet temperature from reaching the theoretical maximum. This large-scale heater can inject higher flow rates of heat-carrying gas, providing technical support for efficient in-situ pyrolysis of oil shale.

Regarding the thermo-hydro-mechanical (THM) coupling problem under high-temperature steam injection in oil shale, Jia et al. [20] investigated the heat transfer characteristics of Balikun oil shale from Xinjiang at temperatures

(a)

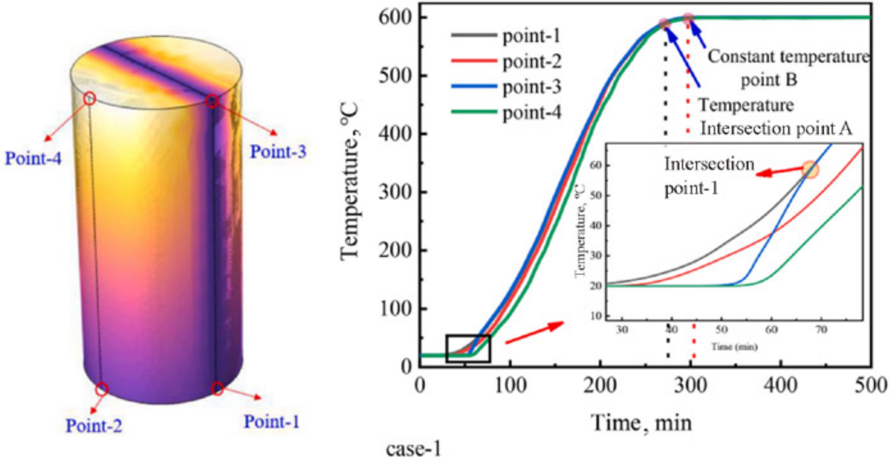

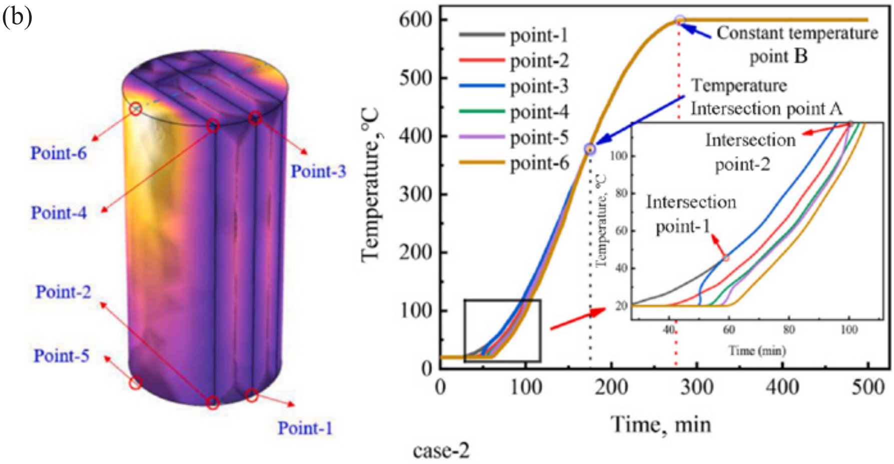

Fig. 2. Specimen temperature measurement points over time [20].

ranging from 25 to 550 °C. They demonstrated that a multi-fracture heating model provides a larger heating area compared to a single-fracture model, as shown in Figure 2, achieving a stable temperature of 600 °C 30 min earlier. The study revealed the permeability–heat transfer mechanism of oil shale during steam pyrolysis.

To further elucidate the evolution of the anisotropic thermal conductivity of oil shale with temperature and its correlation with anisotropic pore-fracture structures, Jin et al. [21] tested the weight loss, specific heat capacity, pore-fracture structure, and anisotropic thermal conductivity of oil shale with temperature. As shown in Figure 3, the main weight loss of oil shale occurs after 400 °C. The thermal conductivity of parallel and vertical beddings decreases

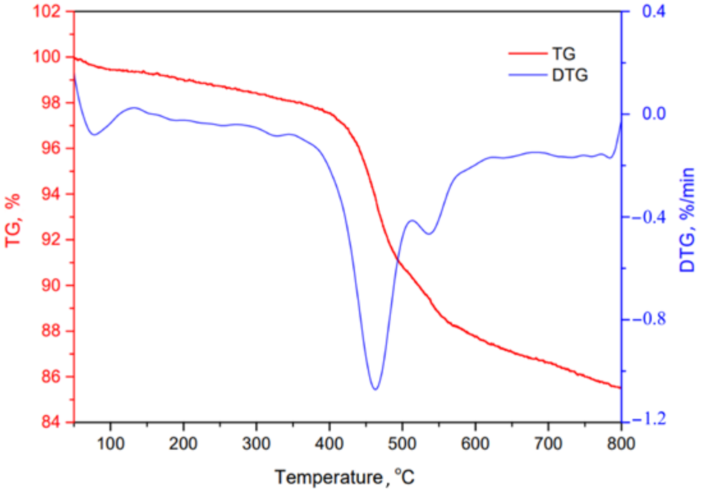

Fig. 3. TG and DTG curves of weight loss during oil shale pyrolysis [21].

linearly with the increase of temperature, and the thermal conductivity of parallel bedding is always greater than that of vertical bedding. The specific heat capacity increases first and then decreases, reaching a maximum at 400 °C. This study provides a key experimental basis for the optimization of oil shale in-situ pyrolysis mining technology.

Numerous scholars have conducted extensive research on heat transfer during in-situ oil shale conversion. Zhang et al. [22] established a spherical heat transfer model and a first-order heat transfer model, and suggested that heat transfer is an important factor affecting the yield of oil shale pyrolysis products. When the particle size of oil shale is small or the heating rate is slow, the calculation results of the first-order heat transfer model are more accurate. When the simulation is carried out in the same number of stages, the first-order heat transfer model can also reduce the computational load. Furthermore, regarding the heat transfer model within the pyrolysis reactor, Di Maio [23] used the discrete element method to simulate the heat transfer process of particles in the retort. The model considers the heat transfer between fluid and particles, particles and particles, fluid and reactor surface, and particles and reactor surface. The simulation results are in good agreement with the experimental data.

Overall, significant progress has been made in the field of heat transfer during in-situ oil shale conversion in recent years, particularly in multi-physics coupling simulations and a refined understanding of heat transfer processes. The core challenges faced by current research primarily stem from the geological characteristics of oil shale itself. Future research should focus on the low thermal conductivity characteristics of oil shale, deeply explore and optimize the heat transfer process, overcome the bottleneck of oil shale in-situ conversion technology, and enable its large-scale application.

3. Mechanism of heat transfer between fluids and solids in in-situ oil shale conversion

In the in-situ pyrolysis of oil shale, high-temperature gas brings heat from the gas injection well to the oil shale layer, and then the heat is transferred from the gas into the solid and liquid phases [24]. The numerical simulation of in-situ pyrolysis mining of oil shale requires establishing the corresponding physical model, and then calculating and solving the simulation results. The physical laws that the fluid must follow during flow are mainly the continuity equation, the mass conservation equation, and the motion equation [25].

The continuity equation is generally expressed as follows:

$$\frac{\partial \rho}{\partial t} + \nabla \cdot (\rho \vec{v}) = S_m, \tag{1}$$

where S_m denotes the mass source term.

If the established geometric model exhibits two-dimensional axisymmetric characteristics, the mass conservation equation is expressed as follows:

$$\frac{\partial \rho}{\partial t}+\frac{\partial}{\partial x}(\rho v_x)+\frac{\partial}{\partial r}(\rho v_r)+\frac{\rho v_r}{r}=S_m, \tag{2}$$

where x denotes the axial coordinate, r represents the radial coordinate, v_x indicates the axial velocity, and v_r stands for the radial velocity.

In an inertial reference frame, the motion equation can be expressed as follows:

$$\frac{\partial \rho}{\partial t}(\rho\vec{v})+\nabla\cdot(\rho\vec{v}\vec{v})=-\nabla \mathrm{p}+\nabla\cdot(\bar{\bar{\tau}})+\rho\vec{g}+\vec{F}, \tag{3}$$

where p denotes the fluid pressure, $\rho\vec{g}$ represents the gravitational force, $\vec{F}$ includes other external forces related to the model, and $\bar{\bar{\tau}}$ signifies the stress tensor. The latter can be expressed as follows:

$$\bar{\bar{\tau}}=\mu\left[(\nabla\vec{v}+\nabla\vec{v}^T)-\frac{2}{3}\nabla\cdot\vec{v}I\right], \tag{4}$$

where μ denotes the molecular viscosity, I represents the unit tensor, and v indicates the swirl velocity.

If the established geometric model exhibits two-dimensional axisymmetric characteristics, the motion equations can be expressed as follows:

$$\begin{aligned}&\frac{\partial}{\partial t}(\rho v_x)+\frac{1}{r}\frac{\partial}{\partial x}(r\rho v_x v_x)+\frac{1}{r}\frac{\partial}{\partial r}(r\rho v_r v_x)=-\frac{\partial p}{\partial x}\\&+\frac{1}{r}\frac{\partial}{\partial x}\left[r\mu\left(2\frac{\partial v_x}{\partial x}-\frac{2}{3}(\nabla\cdot\vec{v})\right)\right]+\frac{1}{r}\frac{\partial}{\partial r}\left[r\mu\left(\frac{\partial v_x}{\partial r}+\frac{\partial v_r}{\partial x}\right)\right]+F_x\end{aligned}, \tag{5}$$

$$\begin{aligned}&\frac{\partial}{\partial t}(\rho v_r)+\frac{1}{r}\frac{\partial}{\partial x}(r\rho v_x v_r)+\frac{1}{r}\frac{\partial}{\partial r}(r\rho v_r v_r)=-\frac{\partial p}{\partial r}+\frac{1}{r}\frac{\partial}{\partial x}\left[r\mu\left(\frac{\partial v_r}{\partial x}+\frac{\partial v_x}{\partial r}\right)\right]\\&+\frac{1}{r}\frac{\partial}{\partial r}\left[r\mu\left(2\frac{\partial v_r}{\partial r}-\frac{2}{3}(\nabla\cdot\vec{v})\right)\right]-2\mu\frac{v_r}{r^2}+\frac{2}{3}\frac{\mu}{r}(\nabla\cdot\vec{v})+\rho\frac{v_z^2}{r}+F_r,\end{aligned} \tag{6}$$

$$\nabla\cdot\vec{v}=\frac{\partial v_x}{\partial x}+\frac{\partial v_r}{\partial r}+\frac{v_r}{r}. \tag{7}$$

Considering the energy model in the research process, heat transfer occurs when there is a temperature difference between different blocks. The heat conduction equation can be expressed as follows:

$$\rho\cdot C\frac{\partial T}{\partial t}=\nabla(\lambda\nabla T)+S(x,y,z,t). \tag{8}$$

The initial conditions can be expressed as follows:

$$T(x,y,z,0)=T_0(x,y,z). \tag{9}$$

The boundary conditions can be expressed by the following three equations:

$$T|_{\Gamma_1} = T_w(x,y,z,t)(\Gamma \in \Gamma_1), \tag{10}$$

$$-\lambda \cdot \frac{\partial T}{\partial n} = q(x,y,z,t)(\Gamma \in \Gamma_2), \tag{11}$$

$$-\lambda \cdot \frac{\partial T}{\partial n}|_{\Gamma_3} = h(T - T_1)(\Gamma \in \Gamma_3). \tag{12}$$

In Equations (8)–(12), $T(x,y,z,t)$ denotes the temperature field, ρ is the density of the material, λ represents the thermal conductivity, C is the specific heat capacity, and $S(x,y,z,t)$ denotes the internal heat source generated by radiation. $T_0(x,y,z)$ is the initial temperature distribution, while $T_w(x,y,z,t)$ represents the prescribed temperature on the system boundary. $q(x,y,z,t)$ denotes the heat flux density on the boundary, and h is the convective heat transfer coefficient. T_1 represents the ambient temperature. The variables x,y,z denote the spatial coordinates and t denotes time. ∇ is the gradient operator and n represents the outward normal direction to the boundary. Γ_1, Γ_2, and Γ_3 denote the Dirichlet, Neumann, and Robin boundaries, respectively, of the computational domain.

In THM simulations of oil shale, software such as COMSOL or Ansys Fluent is commonly employed. COMSOL yields accurate results but is computationally demanding, while Fluent is more flexible and suited for larger-scale problems. When Fluent is utilized for such studies, it enables the simulation of heat conduction processes within both fluid and solid domains, as well as at their boundaries, requiring only the configuration of necessary parameters for the simulation.

The energy equation in Fluent is expressed as follows:

$$\frac{\partial}{\partial t}(\rho E) + \nabla \cdot \left(\vec{v}(\rho E + p)\right) = \nabla \cdot \left(k_{eff} \nabla T - \sum_j h_j \vec{J}_j + \left(\bar{\bar{\tau}}_{eff} \cdot \vec{v}\right) \right) + S_h, \tag{13}$$

where $E = h - \frac{p}{\rho} + \frac{v^2}{2}$, k_{eff} presents the effective conductivity, and $\vec{J}$ denotes the diffusion flux.

Undeniably, oil shale is a typical porous medium characterized by low permeability and low porosity [26]. The energy conduction equation in Fluent is as follows:

$$\frac{\partial}{\partial t}(\rho h) + \nabla \cdot (\vec{v} \rho h) = \nabla \cdot (k \nabla T) + S_h. \tag{14}$$

In-situ underground pyrolysis of oil shale occurs in a multi-field coupled environment involving thermal, hydrodynamic, mechanical, and chemical interactions, representing a classic THM coupling problem in porous fractured rock masses [27]. After the beginning of pyrolysis, the porosity and permeability of oil shale increase rapidly, which accelerates the seepage velocity of fluids and improves the diffusion rate of the temperature field. On the other hand, the density, elastic modulus, and Poisson's ratio of oil shale change with temperature, and the variation of the temperature field leads to the redistribution of stress field [28]. Ultimately, thermal stress modifies the apertures of pores and fractures, affecting the reservoir's porosity and permeability, which in turn induces further alterations in the seepage field. On the whole, the in-situ pyrolysis of oil shale is a thermal-flow-force multi-field dynamic coupling cycle process initiated by heat, involving changes in physical and chemical properties, and driving the evolution of permeability and seepage field through stress field adjustments.

Regarding shale gas extraction, Li et al. [29] developed a fully coupled multi-domain and multi-physics model, dividing the post-hydraulic fracturing shale reservoir into three core domains: SRD (stimulated reservoir domain), NSRD (non-stimulated reservoir domain), and HF (hydraulic fractures). The proposed THM coupling simulation accurately reflects the interactions of multi-domain and multi-physical processes during shale gas extraction.

For the pyrolysis of oil shale under microwave irradiation, Wang et al. [30] conducted numerical simulations based on a fully coupled electromagnetic-thermal-chemical-hydraulic model for three-dimensional porous media using the finite element method. As shown in Figure 4, high power was suitable for rapid heating, while low power facilitated efficient pyrolysis. Consequently, they proposed a variable-power heating mode, which simultaneously reduced heating time and improved thermal uniformity. Product analysis indicated that precise temperature control through parameter optimization was necessary to avoid secondary reactions of oil products. This study provides theoretical support for improving the heat transfer efficiency of microwave pyrolysis of oil shale.

Based on a fully coupled three-dimensional electro-thermal-chemical-fluid-solid model to study microwave heating in-situ conversion technology, Zhu et al. [31] found that the dielectric properties of oil shale are temperature-dependent, exhibiting a slow initial heating rate followed by rapid acceleration. When the pyrolysis temperature exceeds 500 °C, the heating rate increases significantly, and this phenomenon becomes more pronounced under high-power microwave irradiation. Compared to electric heating, microwave heating accelerates the generation of pressure gradients and thermal stress in oil shale while simultaneously enhancing its porosity and permeability. The research proves that microwave heating, rather than oil shale upgrading, has great potential.

In-situ oil shale conversion involves complex coupling of pyrolysis reactions, fluid flow, rock deformation, and heat transfer processes. The THM coupling model can simultaneously account for the interactions among temperature fields, seepage fields, and stress fields, thereby avoiding

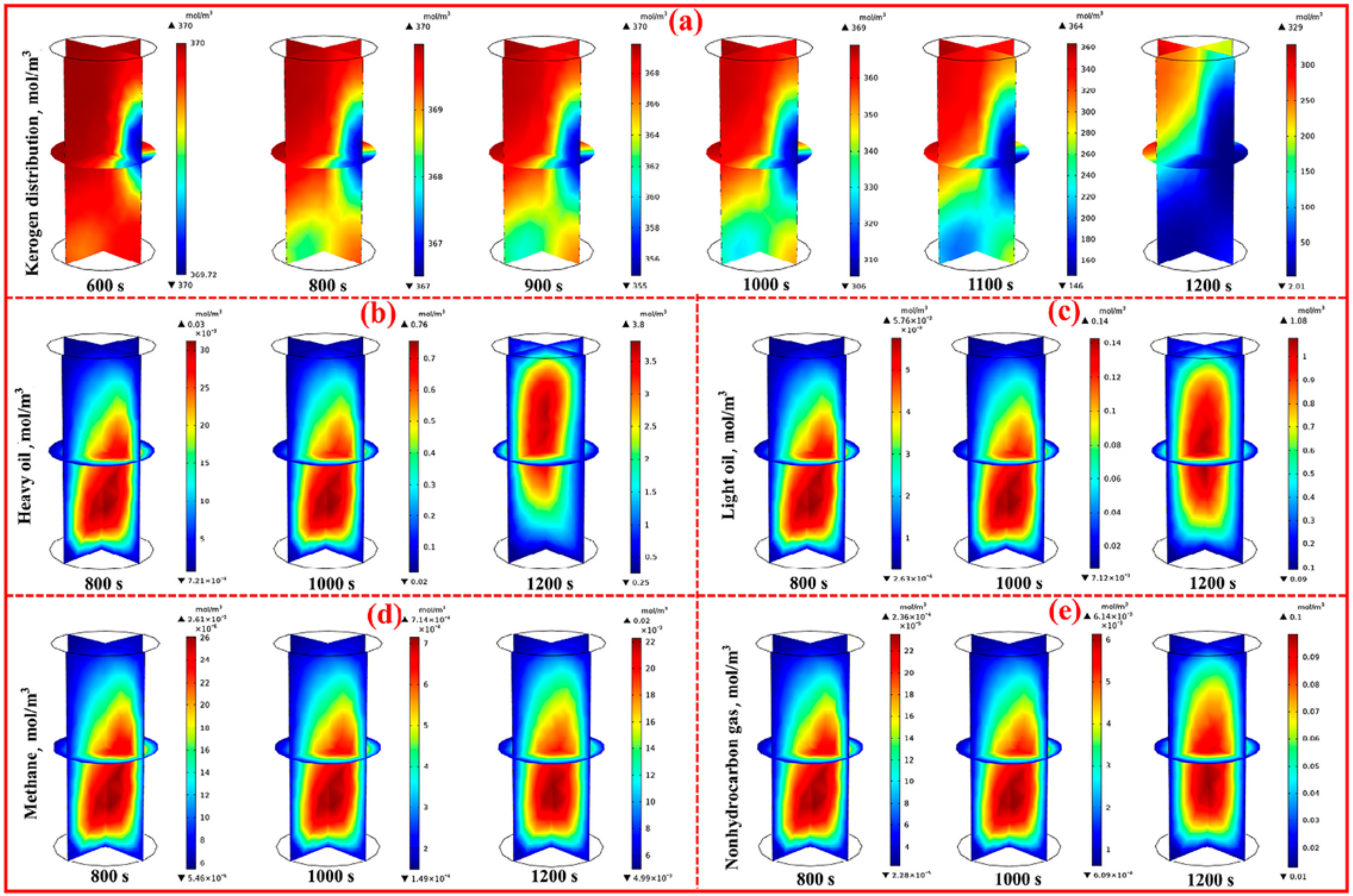

Fig. 4. Dynamic distribution of products during oil shale pyrolysis under a variable-power heating mode [30].

biases inherent in single-physics simulations [32]. Under well pattern control conditions, THM coupling simulations can analyze the impact of different operational parameters on heat transfer efficiency. THM coupling can simulate stress-strain field variations, predict formation change trends, and provide a basis for well pattern control strategies [33]. Therefore, conducting THM simulations for in-situ oil shale conversion serves as a critical approach to studying heat transfer mechanisms under well pattern control conditions.

4. Numerical simulation of in-situ oil shale extraction via well pattern regulation

The core of in-situ oil shale extraction lies in heating kerogen to pyrolyze it into oil and gas, a process that heavily relies on efficient heat transfer [34]. Under natural conditions, heat transfer in the formation is inefficient and difficult to control. Well pattern regulation establishes a controlled engineering system by deploying specific injection and production wells, fundamentally altering the heat transport environment. Specifically, well pattern control directly influences the temperature field distribution within the formation by adjusting the temperature, pressure, and flow rate of the injected fluid [35]. Large-scale field testing of well pattern control for heat transfer technology is usually difficult; therefore, numerical simulation has become an important tool for such studies.

Conducting numerical simulations of heat transfer in oil shale under well pattern control conditions is a key technical pathway to enhance the efficiency and safety of in-situ oil shale extraction [36]. The fundamental principle of well pattern control technology lies in precisely regulating the physical fields around the wellbore and within the reservoir to create an optimal environment for the pyrolysis and conversion of oil shale. The core concept of this technology involves meticulous management of injection and production wells to actively control the temperature, pressure, and fluid flow fields within the reservoir, thereby effectively guiding and constraining the oil shale pyrolysis process [37]. Its primary objective is to efficiently and safely convert solid oil shale kerogen into mobile hydrocarbon products within a controlled "reaction vessel" (i.e., the reservoir). Table 1 summarizes the well pattern deployment methods for in-situ oil shale extraction.

Numerical simulation serves as the cornerstone for the design and optimization of well pattern control technology. Researchers establish comprehensive mathematical models that couple heat transfer, chemical reactions, fluid flow, and rock mechanics to simulate and predict extraction performance under various well pattern control schemes [38].

Table 1. Well pattern deployment methods for in-situ oil shale extraction

Well pattern deployment type	**Typical layout description**	**Advantages**	**Disadvantages**
Five-spot/nine-spot well pattern	The center of a square area serves as an injection/heating well, with the four corners/edges as production wells	Established theoretical model, easy to manage, suitable for early small-scale pilot tests	Sweep efficiency may be non-uniform; poor adaptability to heterogeneous reservoirs; difficult to achieve large-scale volume heating
Triangular/hexagonal well pattern	Heating wells are arranged in an equilateral triangular or regular hexagonal array; production wells can be located at the center or edges of the array	Triangular: fast heating rate. Hexagonal: high energy utilization efficiency and uniform coverage	Requires a large number of wells, increasing investment costs; high requirements for drilling precision
Linear well pattern	Heating and production wells are arranged alternatingly in separate rows	Clear displacement direction, easy control of the heating sweep range, suitable for large-area development	High reservoir homogeneity required; prone to forming “dead oil zones” between well rows; limited lateral sweep efficiency
Vertical-horizontal well combination	Vertical and horizontal wells are deployed in coordination	Flexible layout, adjustable according to reservoir conditions	Complex design; requires precise geological understanding

The impact of well pattern on oil shale extraction is primarily reflected in two aspects: inter-well structure design and well spacing. Jia et al. [39] innovatively adopted an “injection well-heating hole-production well” configuration. By adding heating holes between injection and production wells, a low-temperature gas barrier was constructed to prevent groundwater intrusion into the production zone, thereby avoiding energy waste caused by direct exposure of groundwater to high temperatures in traditional well patterns. Simultaneously, this design allows nitrogen to heat up during flow, focusing thermal energy on hydrocarbon production rather than groundwater, which enhances pyrolysis efficiency and accelerates the initiation of oil production. Compared to conventional well patterns, this approach also reduces production delays and improves concurrent extraction efficiency.

In the investigation of a novel method for in-situ extraction of oil shale through long-distance horizontal wells high-temperature steam injection, Ren et al. [40] established a THM-coupled mathematical model that accounts for the anisotropy of oil shale. They compared the extraction efficiency between the conventional vertical well pattern and the new method, as illustrated in Figure 5. The results demonstrated that the new method achieves higher heating efficiency. Furthermore, key parameters were optimized, and economic analysis was conducted to validate the feasibility of the new approach, providing theoretical and data support for efficient in-situ pyrolysis of oil shale.

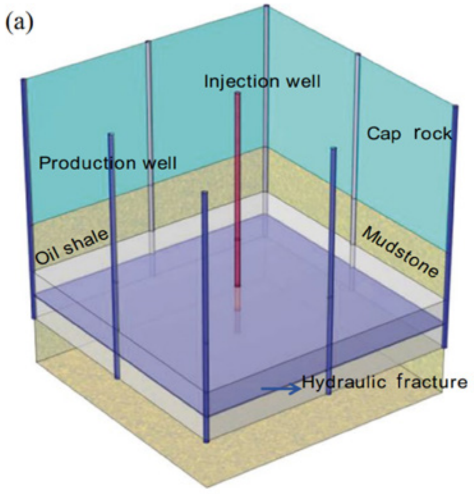

Vertical well case

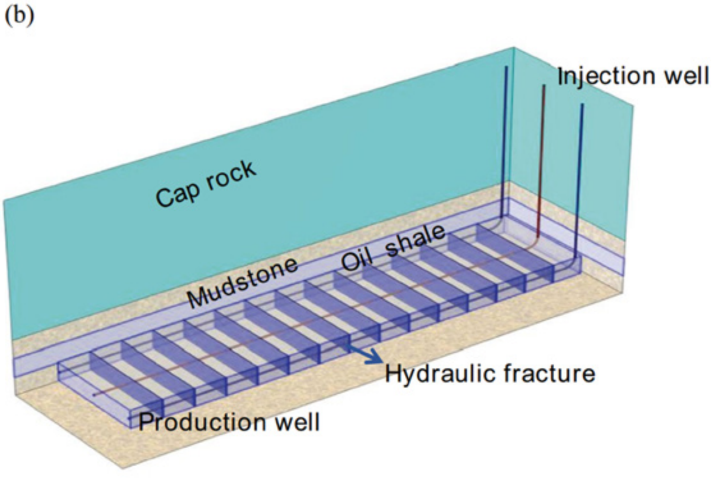

Horizontal well case

Fig. 5. Schematic diagram of vertical and horizontal well cases [40].

To explore low-power, high-yield three-dimensional oil shale well pattern models, Sun et al. [41] conducted numerical simulations using Ansys Fluent to evaluate the cumulative oil production, annual oil production, heating rate factor, and energy consumption per unit volume for the seven well pattern models shown in Figure 6. The results demonstrated that all models achieved in-situ pyrolysis directly without a preheating period. Model VII reached peak annual oil production at 360 days, with a peak heating rate factor of 3.696 at 540 days, and completed full pyrolysis by 780 days. Model VI exhibited the lowest energy consumption per unit volume at only 814.87 kW/m³, reducing consumption by 41.93% compared to other models and achieving the highest energy utilization efficiency. This study provides key technical support for the design of well types in in-situ oil shale mining field experiments.

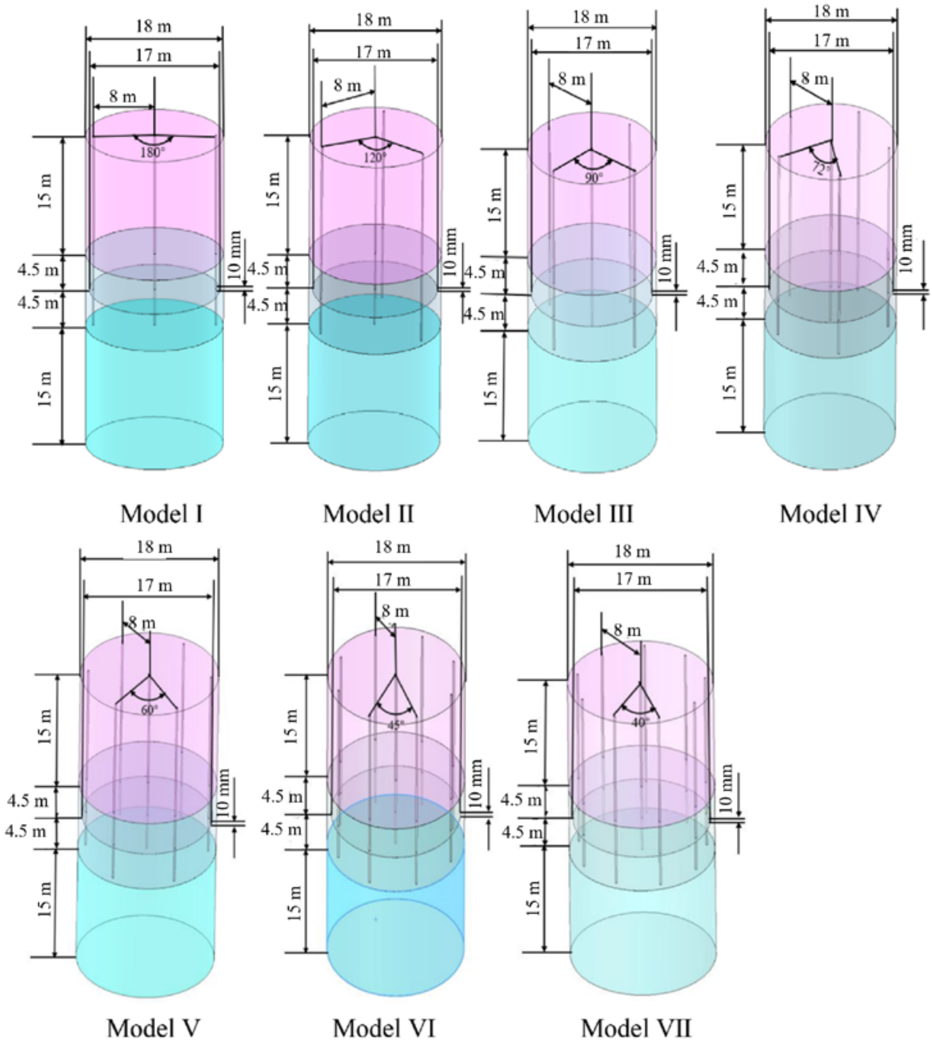

Fig. 6. Schematic diagram of different well pattern models for in-situ heating of oil shale [41].

At present, scholars mainly use the STARS module of CMG software to simulate the in-situ conversion and heating process of oil shale. Pei et al. [42] carried out numerical simulations of a seven-spot well group for nitrogen injection assisted in-situ conversion process (NAICP) and analyzed factors influencing the energy utilization rate and oil-gas recovery ratio. Under a gas injection temperature of 300 °C gas injection and a flow rate of 400 m^3/day, the NAICP technology demonstrated higher production efficiency. The oil output equivalent and maximum oil yield were 1.17 and 1.28 times that of the in-situ conversion process, respectively, and energy utilization rate was improved. Song et al. [43] conducted numerical simulations of multi-level branch wells, showing that the injection temperature strongly influences hydrocarbon generation in oil shale. For multi-branch wells, a production scheme of five branch wells with a 60° branch angle and 40 m branch length achieved the highest oil and gas generation efficiency. These studies show that optimizing injection temperature and well structure can significantly improve oil production efficiency and energy utilization in the in-situ conversion of oil shale.

Current research has clearly revealed the complex effects of well spacing, well type, and well pattern on thermal field distribution, heating efficiency, and production dynamics. Future studies should adopt an economically oriented approach, focusing on establishing numerical simulation methods for well pattern control that account for multi-well pattern characteristics. This involves uncovering the synergistic mechanisms of thermal field regulation through well patterns and quantifying the differential effects of various well pattern combinations on the evolution of porosity and permeability parameter fields. The ultimate goal is to develop well group optimization technology that enhances heat transfer efficiency in self-generating heat in-situ conversion of oil shale, thereby providing theoretical support for predicting development outcomes and optimizing well pattern deployment.

5. Conclusions

This paper presents an in-depth examination of numerical simulation of well-pattern controlled heat conduction in in-situ oil shale conversion and draws the following conclusions:

1. The core of in-situ oil shale conversion lies in heat transfer efficiency. Current research has made progress in multi-field coupling simulations and understanding heat transfer mechanisms. However, the low thermal conductivity of oil shale leads to high costs and significant environmental risks. Well pattern control (including well type and spacing) directly affects the thermal field and extraction efficiency, making it a critical direction for optimization.

2. This paper fills a gap in the review of numerical simulations of in-situ heat transfer in oil shale under well pattern regulation. Future research should focus on refining the flow rate control ratio of production wells in group well regulation experiments, determining the optimal production flow ratio, and characterizing pyrolysis products, component variations, pyrolysis temperature, and its evolution patterns. These efforts aim to maximize pyrolysis oil yield and quality while optimizing the group well regulation extraction system.

This study provides valuable insights for the in-situ conversion and development of oil shale. Based on numerical simulation technology, it highlights the heat transfer mechanism in in-situ oil shale conversion and identifies new opportunities in the field under well pattern control.

Data availability statement

No new data were generated or analyzed in support of this review.

Acknowledgments

Yu Cao contributed to writing the original draft, Yi Pan contributed to funding acquisition, Shuangchun Yang contributed to supervision and proofreading, and Hui Yang was responsible for investigation and formal analysis. This work was supported by the National Science Foundation of China (project No. 52574041) Microscopic mechanism of transverse isotropic thermal damage in microwave-enhanced pyrolysis of oil shale. The publication costs of this article were partially covered by the Estonian Academy of Sciences.

References

1. Al-Gharabli, S. I., Azzam, M. O. J., Al-Addous, M. Microwave-assisted solvent extraction of shale oil from Jordanian oil shale. *Oil Shale*, 2015, **32**(3), 240–251. https://doi.org/10.3176/oil.2015.3.04
2. Yihdego, Y., Salem, H. S., Kafui, B. G., Veljkovic, Z. Economic geology value of oil shale deposits: Ethiopia (Tigray) and Jordan. *Energy Sources Part A: Recovery, Utilization, and Environmental Effects*, 2018, **40**(17), 2079–2096. https://doi.org/10.1080/15567036.2018.1488015
3. Kong, D., Meng, X., Zhu, J., Zhou, W. Molecular dynamics simulation of surfactant induced wettability alteration of shale reservoirs. *Frontiers in Energy Research*, 2023, **11**, 1272132. https://doi.org/10.3389/fenrg.2023.1272132
4. Publisher's note. *Energy Reports*, 2022, **8**(S13), 1099–1112. https://doi.org/10.1016/j.egyr.2022.08.174

5. Wang, L., Yang, D., Kang, Z., Zhao, J., Meng, Q. Experimental study on the effects of steam temperature on the pore-fracture evolution of oil shale exposed to the convection heating. *Journal of Analytical and Applied Pyrolysis*, 2022, **164**, 105533. https://doi.org/10.1016/j.jaap.2022.105533
6. Wang, L., Yang, D., Li, X., Zhao, J., Wang, G., Zhao, Y. Macro and meso characteristics of in-situ oil shale pyrolysis using superheated steam. *Energies*, 2018, **11**(9), 2297. https://doi.org/10.3390/en11092297
7. Bai, F., Sun, Y., Liu, Y., Guo, M. Evaluation of the porous structure of Huadian oil shale during pyrolysis using multiple approaches. *Fuel*, 2017, **187**, 1–8. https://doi.org/10.1016/j.fuel.2016.09.012
8. Kang, Z., Zhao, Y., Yang, D. Review of oil shale in-situ conversion technology. *Applied Energy*, 2020, **269**, 115121. https://doi.org/10.1016/j.apenergy.2020.115121
9. Hou, L., Tian, H., Yu, Z., Zhao, Z., Wu, S., Li, X. Dynamic evolution mechanism of reservoir physical properties during oil shale in situ conversion. *Energy & Fuels*, 2024, **38**(10), 8631–8640. https://doi.org/10.1021/acs.energyfuels.4c00141
10. Jiang, T., Yang, L., Zhu, C. Effect of pressure on the oil shale convection heating in-situ conversion process. *International Journal of Thermal Sciences*, 2025, **214**, 109940. https://doi.org/10.1016/j.ijthermalsci.2025.109940
11. Wang, C., Liu, Y., Song, D., Xu, J., Wang, Q., Zhang, S. Evaluation of bedding effect on the bursting liability of coal and coal-rock combination under different bedding dip angles. *Advances in Geo-Energy Research*, 2024, **11**(1), 29–40. https://doi.org/10.46690/ager.2024.01.04
12. Sun, Y., He, L., Kang, S., Guo, W., Li, Q., Deng, S. Pore evolution of oil shale during sub-critical water extraction. *Energies*, 2018, **11**(4), 842. https://doi.org/10.3390/en11040842
13. Liu, Z., Ma, H., Guo, J., Liu, G., Wang, Z., Guo, Y. Pyrolysis characteristics and effect on pore structure of Jimsar oil shale based on TG-FTIR-MS analysis. *Geofluids*, 2022, 7857239. https://doi.org/10.1155/2022/7857239
14. Wang, C.-Y. Measurements, mechanisms, and models of heat transport: by A. M. Hofmeister, Elsevier, 2018. *Contemporary Physics*, 2020, **61**(4), 303–304. https://doi.org/10.1080/00107514.2020.1853240
15. Mandal, I., Pal, S. COVID-19 pandemic persuaded lockdown effects on environment over stone quarrying and crushing areas. *Science of The Total Environment*, 2020, **732**, 139281. https://doi.org/10.1016/j.scitotenv.2020.139281
16. Metwally, H., Mahmoud, N. A., Aboelsoud, W., Ezzat, M. Yearly performance of the photovoltaic active cooling system using the thermoelectric generator. *Case Studies in Thermal Engineering*, 2021, **27**, 101252. https://doi.org/10.1016/j.csite.2021.101252
17. Pan, Y., Jia, Y., Zheng, J., Yang, S., Bttina, H. Research progress of fracture development during in-situ cracking of oil shale. *Journal of Analytical and Applied Pyrolysis*, 2023, **174**, 106110. https://doi.org/10.1016/j.jaap.2023.106110

18. Jiang, H., Liu, S., Wang, J., You, Y., Yuan, S. Study on evolution mechanism of the pyrolysis of Chang 7 oil shale from Ordos basin in China. *Energy*, 2023, **272**, 127097. https://doi.org/10.1016/j.energy.2023.127097
19. Bu, Q., Li, Q., Li, X. Numerical heat transfer simulation of oil shale large-size downhole heater. *Applied Sciences*, 2024, **14**(6), 2235. https://doi.org/10.3390/app14062235
20. Jia, Y., Huang, X., Yang, D., Sun, D., Luo, C. Thermo-hydro-mechanical coupling in oil shale: investigating permeability and heat transfer under high-temperature steam injection. *Case Studies in Thermal Engineering*, 2024, **61**, 104862. https://doi.org/10.1016/j.csite.2024.104862
21. Jin, J., Liu, J., Jiang, W., Cheng, W., Zhang, X. Evolution of the anisotropic thermal conductivity of oil shale with temperature and its relationship with anisotropic pore structure evolution. *Energies*, 2022, **15**(21), 8021. https://doi.org/10.3390/en15218021
22. Zhang, F., Parker, J. C. An efficient modeling approach to simulate heat transfer rate between fracture and matrix regions for oil shale retorting. *Transport in Porous Media*, 2010, **84**, 229–240. https://doi.org/10.1007/s11242-009-9495-x
23. Di Maio, F. P., Di Renzo, A., Trevisan, D. Comparison of heat transfer models in DEM-CFD simulations of fluidized beds with an immersed probe. *Powder Technology*, 2009, **193**(3), 257–265. https://doi.org/10.1016/j.powtec.2009.03.002
24. Wang, L., Yang, D., Zhang, Y., Li, W., Kang, Z., Zhao, Y. Research on the reaction mechanism and modification distance of oil shale during high-temperature water vapor pyrolysis. *Energy*, 2022, **261**, 125213. https://doi.org/10.1016/j.energy.2022.125213
25. Wang, X., Huang, L., Li, X., Bi, S., Li, H., Zhang, J. et al. Wellbore multiphase flow behaviors of gas kick in deep water horizontal drilling. *Frontiers in Physics*, 2022, **10**, 1049547. https://doi.org/10.3389/fphy.2022.1049547
26. Wu, Z., Fang, F., Li, X., Xiao, H., Liu, X., Rao, Y. et al. Division method and seepage law of seepage channels in a tight reservoir. *Geofluids*, 2021, 4804513. https://doi.org/10.1155/2021/4804513
27. Huang, H., Yu, H., Xu, W., Lyu, C., Micheal, M., Xu, H. et al. A coupled thermo-hydro-mechanical-chemical model for production performance of oil shale reservoirs during in-situ conversion process. *Energy*, 2023, **268**, 126700. https://doi.org/10.1016/j.energy.2023.126700
28. Yin, T., Wu, Y., Li, Q., Wang, C., Wu, B. Determination of double-K fracture toughness parameters of thermally treated granite using notched semi-circular bending specimen. *Engineering Fracture Mechanics*, 2020, **226**, 106865. https://doi.org/10.1016/j.engfracmech.2019.106865
29. Li, W., Liu, J., Zeng, J., Leong, Y.-K., Elsworth, D., Tian, J. et al. A fully coupled multidomain and multiphysics model for evaluation of shale gas extraction. *Fuel*, 2020, **278**, 118214. https://doi.org/10.1016/j.fuel.2020.118214
30. Wang, H., Li, X., Zhu, J., Yang, Z., Zhou, J., Yi, L. Numerical simulation of oil shale pyrolysis under microwave irradiation based on a three-dimensional

porous medium multiphysics field model. *Energies*, 2022, **15**(9), 3256. https://doi.org/10.3390/en15093256

31. Zhu, J., Yi, L., Yang, Z., Duan, M. Three-dimensional numerical simulation on the thermal response of oil shale subjected to microwave heating. *Chemical Engineering Journal*, 2021, **407**, 127197. https://doi.org/10.1016/j.cej.2020.127197
32. Chen, X., Rao, X., Xu, Y., Liu, Y. An effective numerical simulation method for steam injection assisted in situ recovery of oil shale. *Energies*, 2022, **15**(3), 776. https://doi.org/10.3390/en15030776
33. Liu, Y., Xue, L., Bai, F., Zhao, J., Yan, Y. Three-dimensional numerical simulation of hydrocarbon production and reservoir deformation of oil shale in situ conversion processing using a downhole burner. *ACS Omega*, 2022, **7**(27), 23695–23707. https://doi.org/10.1021/acsomega.2c02317
34. Ramsay, T. Uncertainty quantification of an explicitly coupled multiphysics simulation of in-situ pyrolysis by radio frequency heating in oil shale. *SPE Journal*, 2020, **25**(3), 1443–1461. https://doi.org/10.2118/200476-PA
35. Lu, Y.-C., Song, S.-R., Taguchi, S., Wang, P.-L., Yeh, E.-C., Lin, Y.-J. et al. Evolution of hot fluids in the Chingshui geothermal field inferred from crystal morphology and geochemical vein data. *Geothermics*, 2018, **74**, 305–318. https://doi.org/10.1016/j.geothermics.2017.11.016
36. Yu, H., Tang, J., Zhang, X., Ren, L., Zhang, X. Analysis of effective pyrolysis zone and heat loss in oil shale reservoir with random fractures. *ACS Omega*, 2023, **8**(48), 45687–45699. https://doi.org/10.1021/acsomega.3c06014
37. Nie, B. Study on thermal decomposition of oil shale: two-phase fluid simulation in wellbore. *Energy*, 2023, **272**, 127124. https://doi.org/10.1016/j.energy.2023.127124
38. Briceño Montilla, M. J., Li, S., Zhang, Z., Hu, Y., He, J., Bo, Z. et al. Energy recovery analysis through numerical simulations of steam injection in continental shale oil reservoirs. *Journal of Petroleum Exploration and Production Technology*, 2025, **15**, 69. https://doi.org/10.1007/s13202-025-01970-4
39. Jia, B., Huang, Z. Oil shale in situ production using a novel flow-heat coupling approach. *ACS Omega*, 2024, **9**(7), 7705–7718. https://doi.org/10.1021/acsomega.3c07009
40. Ren, S., Jia, Y., Zhao, J., Yang, D., Wang, G. Numerical study on in-situ mining oil shale by high-temperature steam injection in long-distance horizontal wells. *Geomechanics and Geophysics for Geo-Energy and Geo-Resources*, 2024, **10**, 161. https://doi.org/10.1007/s40948-024-00869-4
41. Sun, T., Liu, H., Zhang, Y., Li, Y. Numerical simulation and optimization study of in-situ heating for three-dimensional oil shale exploitation with different well patterns. *Case Studies in Thermal Engineering*, 2024, **55**, 104089. https://doi.org/10.1016/j.csite.2024.104089
42. Pei, S., Wang, Y., Zhang, L., Huang, L., Cui, G., Zhang, P. et al. An innovative nitrogen injection assisted in-situ conversion process for oil shale recovery:

mechanism and reservoir simulation study. *Journal of Petroleum Science and Engineering*, 2018, **171**, 507–515. https://doi.org/10.1016/j.petrol.2018.07.071

43. Song, X., Zhang, C., Shi, Y., Li, G. Production performance of oil shale in-situ conversion with multilateral wells. *Energy*, 2019, **189**, 116145. https://doi.org/10.1016/j.energy.2019.116145

Effect of organic macerals on hydrocarbon generation ability of oil shale and coal and establishment of a contribution model – constraints from machine learning

Duoxiao Sun(a,b), Feng Ma(c,d)*, Hongbiao Wang(a,b), Hongliang Dang(a,e,f), Yanwei Bi(a,b), Pingchang Sun(a,b)

(a) College of Earth Sciences, Jilin University, Changchun, Jilin 130061, China
(b) Key-Lab for Oil Shale and Paragenetic Minerals of Jilin Province, Changchun, Jilin 130061, China
(c) School of Resources and Environment, University of Electronic Science and Technology of China, Chengdu 611731, China
(d) Research Institute of Petroleum Exploration & Development-Northwest (NWGI), PetroChina, Lanzhou 730020, China
(e) Technology Innovation Center for Exploration and Exploitation of Strategic Mineral Resources in Plateau Desert Region, Ministry of Natural Resources, Xining 810000, China
(f) Qinghai Geological Survey, Xining 810000, China

Received 13 November 2025, accepted 1 July 2026, available online 3 August 2026

Abstract. *To quantify the impact of organic macerals on hydrocarbon generation in oil shale and coal, this study analyzed 403 datasets. The results show distinct differences in maceral composition between the two materials. Using a random forest model with aquatic liptinite, terrigenous liptinite, vitrinite, and inertinite as inputs, TOC and HI predictions achieved R^2 values of 0.62 and 0.73, respectively. SHAP analysis reveals that aquatic liptinite is the dominant positive contributor to both parameters, while terrigenous liptinite shows a bidirectional effect. Based on these relationships, a quantitative contribution model for organic macerals in oil shale is established, offering insights for resource evaluation and exploration.*

Keywords: *oil shale, coal, organic macerals, random forest model, SHAP analysis.*

---

* Corresponding author, mafeng@petrochina.com.cn

1. Introduction

Oil shale and coal are very important combustible organic minerals, playing a significant role in the energy structure [1, 2]. Both coal and oil shale are organic-rich sedimentary rocks. From the perspectives of clean coal utilization and in-situ oil shale conversion, their hydrocarbon generation capacity is a core indicator for assessing the quality and development feasibility of coal and oil shale resources. This capacity is comprehensively constrained by various factors such as organic matter abundance, organic macerals (source of organic matter), and organic matter maturity. Among these, organic macerals, as the basic constituent units of organic matter in coal and oil shale, directly determine the hydrocarbon generation potential, pyrolysis efficiency, and product characteristics of the organic matter through their type, content, and spatial distribution. They are the key intrinsic factors regulating the hydrocarbon generation processes of oil shale and coal [1–5]. Differences in the source of organic matter (organic macerals) and depositional environments directly lead to significant distinctions in the organic maceral composition of coal versus oil shale.

Traditional studies often qualitatively or semi-quantitatively investigate the relationship between organic macerals and hydrocarbon generation capacity through experimental analyses such as optical microscopy and pyrolysis experiments [6–8]. However, these approaches face challenges in precisely quantifying the contribution weights of individual macerals and unveiling the complex non-linear relationships between macerals and key hydrocarbon generation parameters such as total organic carbon (TOC) and hydrogen index (HI). SHAP (SHapley Additive exPlanations) analysis, an explainable machine learning method grounded in game theory, can overcome the limitations of traditional analyses. By calculating the SHAP value of each feature variable relative to the target variable [9], SHAP quantifies the degree of influence of organic macerals on TOC and HI, identifies key controlling macerals, and visualizes interaction effects between feature variables. Therefore, based on a large compiled dataset of organic geochemical parameters and organic macerals from immature to low-maturity coal and oil shale, this paper investigates the impact of organic macerals on the hydrocarbon generation capacity of oil shale and coal. It focuses specifically on utilizing SHAP analysis to decipher the intrinsic relationships between organic maceral data and TOC/HI, aiming to provide theoretical support and technical references for the precise exploration, quality evaluation, and efficient development and utilization of oil shale and coal resources.

2. Data and research methods

2.1. Data collection

In fact, oil shale is rich in immature to low-maturity organic matter. Therefore, in order to facilitate the comparison of coal and oil shale at the same maturity level, the maturity of the oil shale and coal samples collected in this study ranges from immature to low maturity. This study compiled 178 sets of data for immature to low-maturity oil shales ($Ro \leq 0.7\%$) and 225 sets of data for coals from the Songliao Basin and the Junggar Basin in China, as well as from a series of basins in other countries [10–41]. The complete data sources for all samples are listed in Appendices 1 and 2 (see Supplementary online data). It should be noted that although samples with complete datasets – including organic maceral content, TOC, and HI – are relatively limited, the samples collected in this study generally provide both organic maceral and organic geochemical data from the same source. Furthermore, to ensure comparability of data across different basins, the data collected in this study generally adhere to similar testing methods and experimental instruments. For example, the TOC testing instrument was mainly the LECO TS-230, and the data for rock pyrolysis were obtained using the Rock Eval 6. The organic microscopic component counting scheme is based on percentage statistics and has been normalized.

2.2. Methods

Random forest (RF) was proposed by Breiman based on the integration of statistical learning theory with classification and regression methods [27]. The multiple classification regression decision tree (CART) included in the RF algorithm prevents overfitting and can adjust different types of input variables.

In this study, four organic maceral parameters – aquatic liptinite, terrigenous liptinite, vitrinite, and inertinite – were selected as sensitive factors to investigate their influence on the hydrocarbon generation potential (TOC and HI) of coal and oil shale. The RF model was developed using the Python 3.12 programming language, with implementation carried out via the scikit-learn library. The train_test_split method from the scikit-learn library was employed to partition the dataset into training and testing sets, with a ratio of 70% for training and 30% for testing.

Table 1. Optimal hyperparameter combination

Model	random_state	n_estimators	min_samples_leaf	min_samples_split	max_depth
TOC	240	100	3	4	9
HI	211	300	3	2	4

The GridSearchCV function in Python facilitates the identification of parameters that yield the highest model estimation accuracy [28]. By specifying the values and ranges of the hyperparameters for the RF estimator model and applying the GridSearchCV function, the optimal combination of RF hyperparameters was derived (Table 1).

To identify the most influential factors affecting TOC and HI, the SHAP method was selected to evaluate the contribution value of each feature in predicting TOC and HI. SHAP is a game-theory-based approach designed to explain the output of any machine learning model [9, 29]. In this study, both the global features of multiple linear regression and the global/local features of the RF model, along with the contributions of individual samples, were analyzed.

3. Results

3.1. Organic geochemical characteristics

The collected data (Fig. 1) show that the TOC of oil shale samples is predominantly distributed between 5 and 25 wt%, with a maximum value of 34.6 wt% and an average of 13.36 wt% (Fig. 1a, b). The HI values are concentrated in the range of 435–780 mg HC/g TOC, with a few samples approaching 1000 mg HC/g TOC, and an average as high as 668.2 mg HC/g TOC (Fig. 1b, c). The S_2 values range from 35 to 301.4 mg HC/g rock, with an average of 81.6 mg HC/g rock (Fig. 1a, c). A strong positive correlation is observed between TOC and S_2, while moderate positive correlations exist between TOC and HI, and between S_2 and HI. The organic matter in oil shale samples is mainly type I and type II_1 (Fig. 1).

(a)

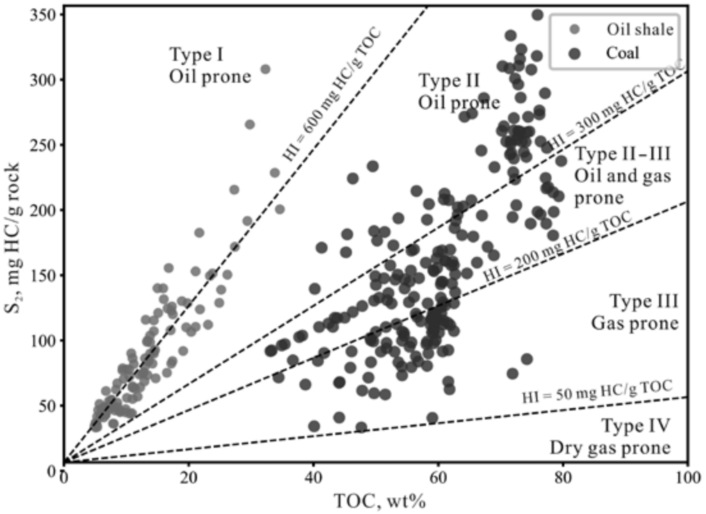

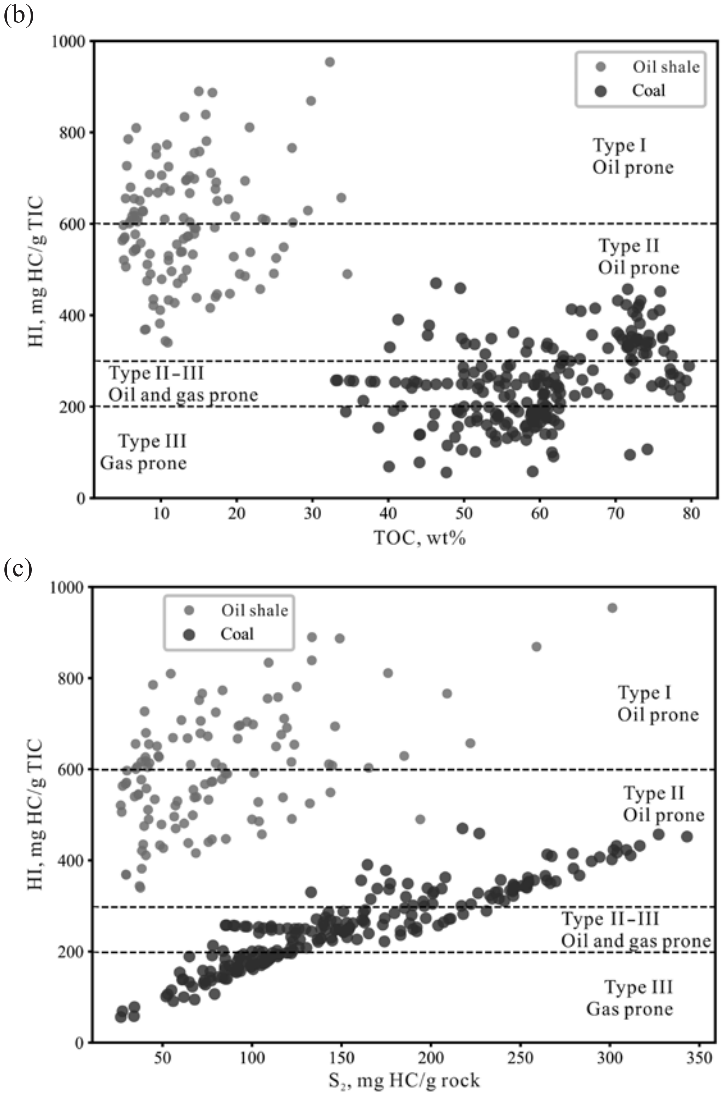

Fig. 1. Scatter plots of the organic geochemical characteristics of oil shale and coal samples: TOC–S_2 scatter plots, showing organic matter types (a); TOC–HI scatter plots (b); S_2–HI scatter plots (c).

For coal samples, TOC ranges from 43.8 to 79.7 wt%, with an average of 59.68 wt% (Fig. 1a, b). HI mainly falls between 138.2 and 366 mg HC/g TOC, averaging 251.26 mg HC/g TOC (Fig. 1b, c). S_2 is predominantly distributed from 73.9 to 265 mg HC/g rock, reaching a maximum of 343.1 mg HC/g rock, with a high average value of 167.73 mg HC/g rock (Fig. 1a, c). Strong positive correlations are observed among TOC, S_2, and HI in coal samples. The organic matter in coal samples is mainly type II–III and type III (Fig. 1).

Although the TOC of oil shale is only one-third to one-fifth that of coal, its hydrocarbon generation efficiency per unit mass of TOC (HI, S_2 /TOC) is two to three times higher than that of coal [30, 31]. This indicates that TOC in oil shale per unit mass typically generates more hydrocarbons than that in coal. Oil shale generally contains higher proportions of hydrogen, oxygen, and sulfur, whereas coal is primarily composed of carbon. These compositional differences lead to variations in combustion characteristics and hydrocarbon yields. One ton of TOC from oil shale can yield 200–300 kg of shale oil, whereas one ton of TOC from coal produces only 50–100 kg of tar (and this is feasible only for low-rank coal). In summary, although oil shale has lower TOC, its hydrocarbon generation potential is higher, exhibiting greater hydrocarbon generation efficiency than coal, which positions oil shale as a potentially efficient oil-generating resource [32–34].

3.2. Organic macerals

The collected data reveal that in oil shale samples, the content of aquatic liptinite is predominantly distributed between 45% and 97%, reaching a maximum of 100%, with a high average value of 66.83%. Terrigenous liptinite content primarily ranges from 5% to 30%, with a small number of samples approaching 70%, while the average is only 15.98% (Fig. 2). Vitrinite is mainly distributed between 5% and 30%, with an average content of 12.24%. Inertinite content ranges from 0% to 10%, with a notably low average of 4.93% (Fig. 3).

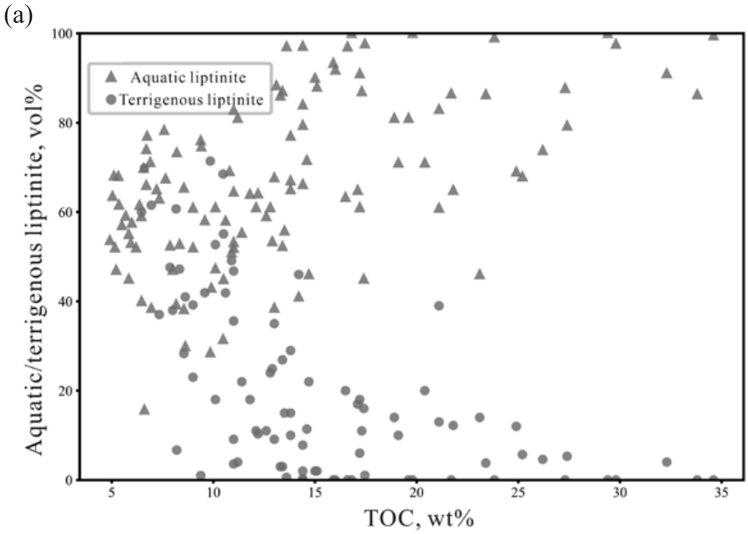

(b)

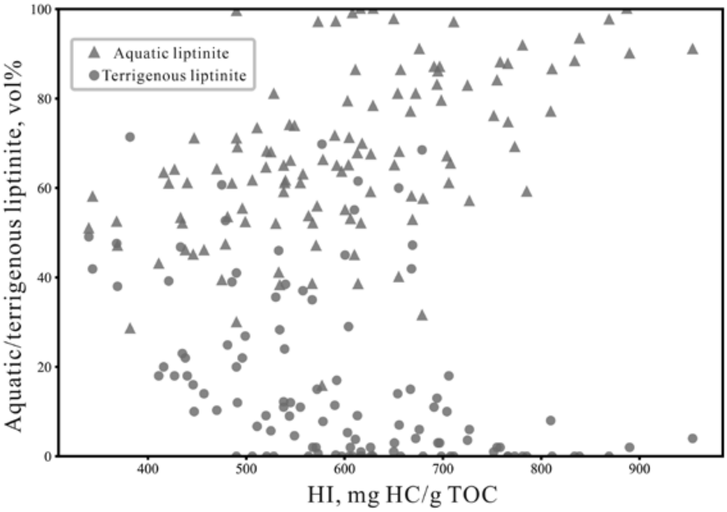

Fig. 2. Scatter plots of TOC vs. aquatic liptinite/terrigenous liptinite (a) and HI vs. aquatic liptinite/terrigenous liptinite (b).

In coal samples, the content of aquatic liptinite is extremely low (generally < 5%, only slightly higher in humic-sapropelic coal). Terrigenous liptinite content in coal is relatively low (1–10%). Vitrinite is predominantly distributed between 40% and 90%, reaching a maximum of 98%, with a high average value of 74.09%. Inertinite content mainly ranges from 0.4% to 5%, with a maximum of 13%, and an average of only 2.73% (Fig. 3).

(a)

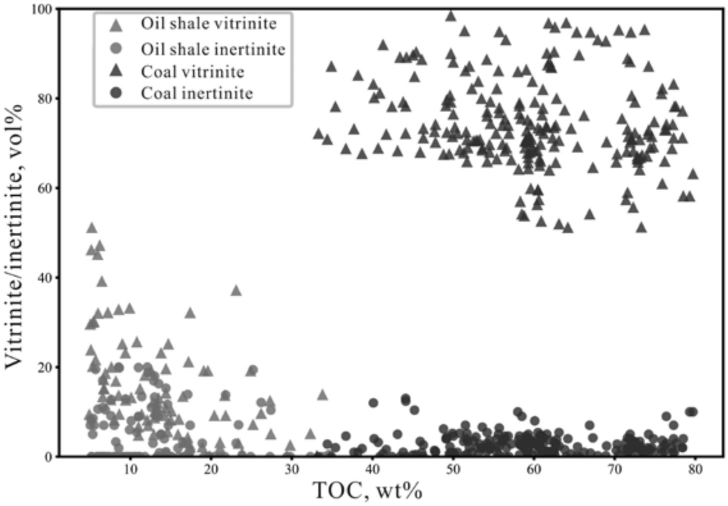

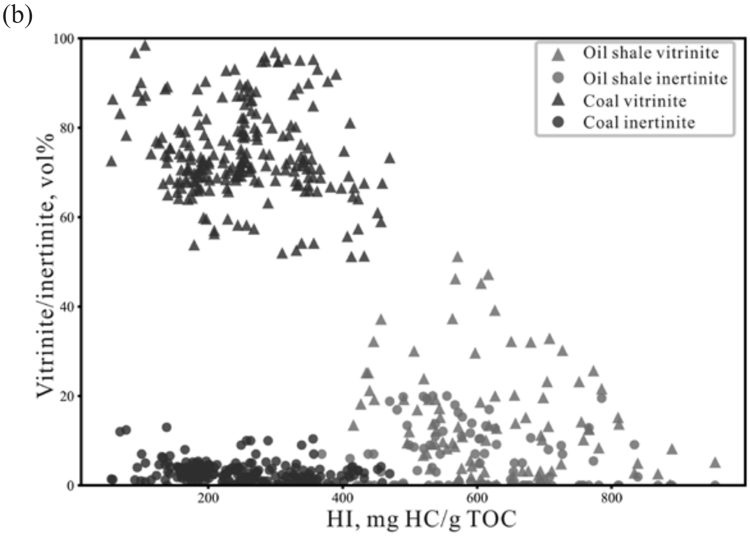

Fig. 3. Scatter plots of TOC vs. vitrinite/inertinite (a) and HI vs. vitrinite/inertinite (b) in oil shale and coal.

3.3. Random forest model and interpretation

An RF model was constructed using four organic maceral parameters to predict TOC and HI in oil shale. The red dots in Figure 4 indicate the predictive performance of the model on the test set, with R^2 (coefficient of determination) values of 0.62 and 0.73, respectively, alongside low root mean square error values, demonstrating satisfactory performance of the model. Therefore, the RF model shows adequate accuracy and adaptability, as well as good predictive ability, and can effectively reveal the complex relationship between organic microscopic components and TOC and HI.

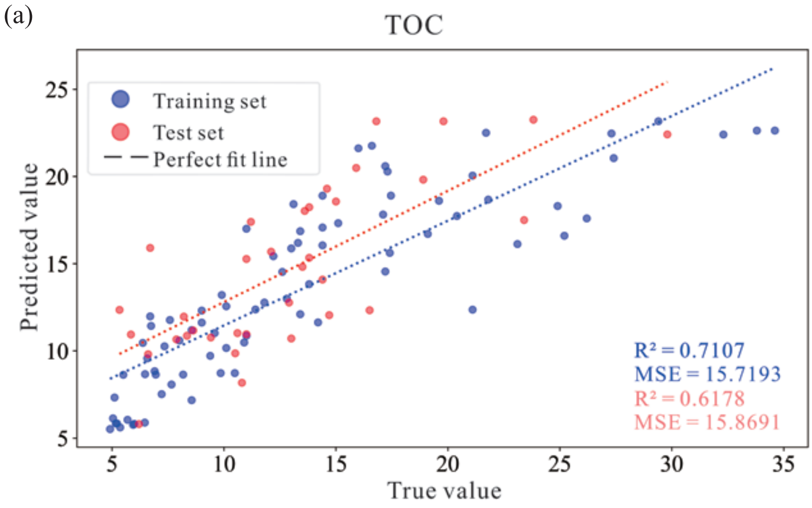

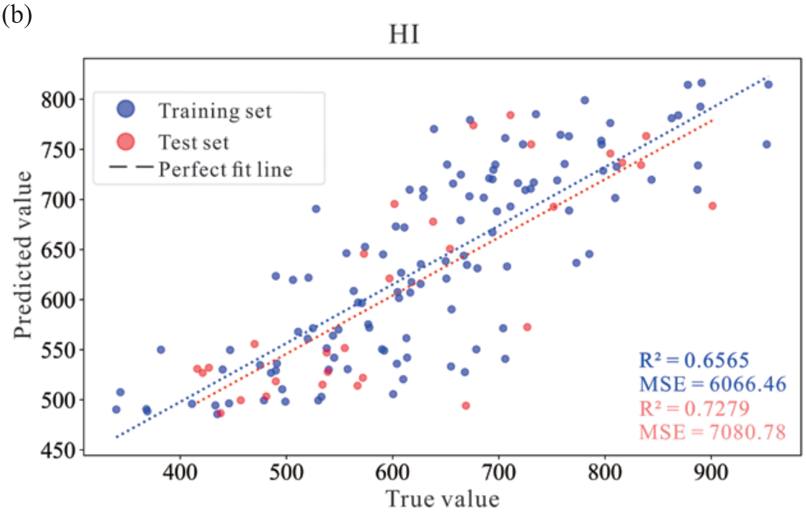

Fig. 4. Comparison of TOC real test tag and integrated output results (a) and HI real test tag and integrated output results.

Based on SHAP analysis, the mean SHAP values were obtained. The global importance of input variables (Fig. 5) represents the average of the absolute SHAP values for each feature across the entire dataset. The input variables are ranked by importance, where a higher mean SHAP value indicates greater importance of the variable [9]. The results demonstrate that aquatic liptinite contributes the most to the model, followed by terrigenous liptinite (Fig. 5). The findings indicate that aquatic liptinite is strongly correlated with TOC and HI, suggesting that it plays a dominant role in hydrocarbon generation potential.

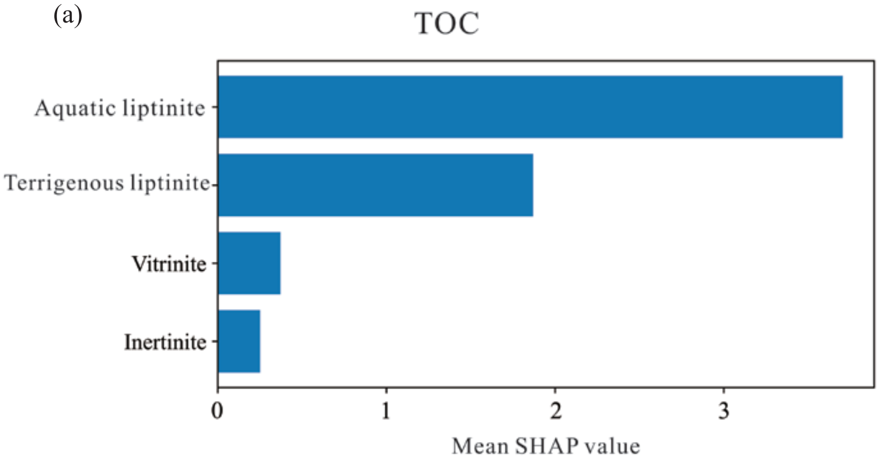

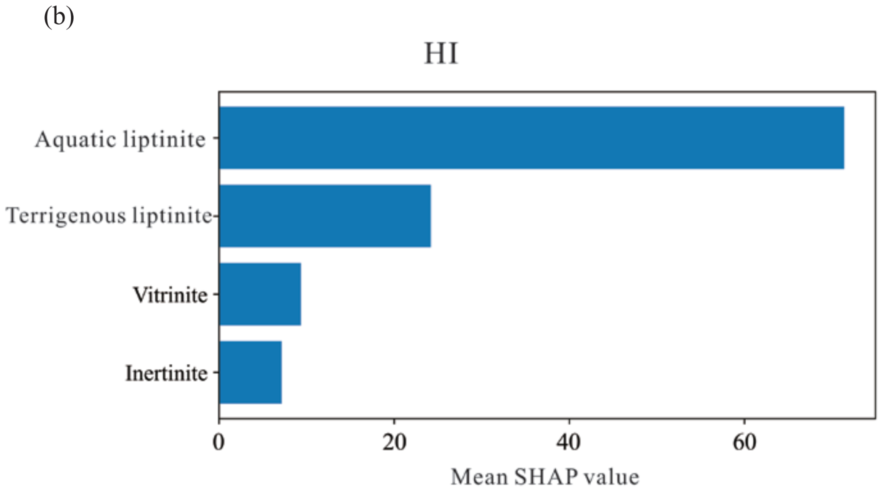

Fig. 5. SHAP values and feature-importance plots of the TOC model (a) and the HI model (b).

By analyzing the factor dependence plots (Fig. 6), the marginal effects of individual input variables on the model predictions in the RF model can be observed. Single dependency analysis illustrates the influence of individual factors on the content. The x-axis represents the feature values of the factor, while the y-axis represents the SHAP values of samples associated with the feature values. The analysis reveals the following:

1. Aquatic liptinite exhibits a strong linear positive correlation with both TOC and HI. In TOC prediction, when aquatic liptinite exceeds 70%, the SHAP values are generally greater than 0, making it more likely to increase TOC content. Conversely, when aquatic liptinite is below 70%, TOC content decreases. The threshold for aquatic liptinite to increase HI content is 70%.
2. The SHAP values of TOC samples show an initial increase followed by a decrease as terrigenous liptinite content increases. When terrigenous liptinite content ranges from 0% to 30%, the SHAP values of TOC samples gradually increase but they begin to decrease when terrigenous liptinite exceeds 30%.
3. Vitrinite has a certain negative influence on both TOC and HI contents.

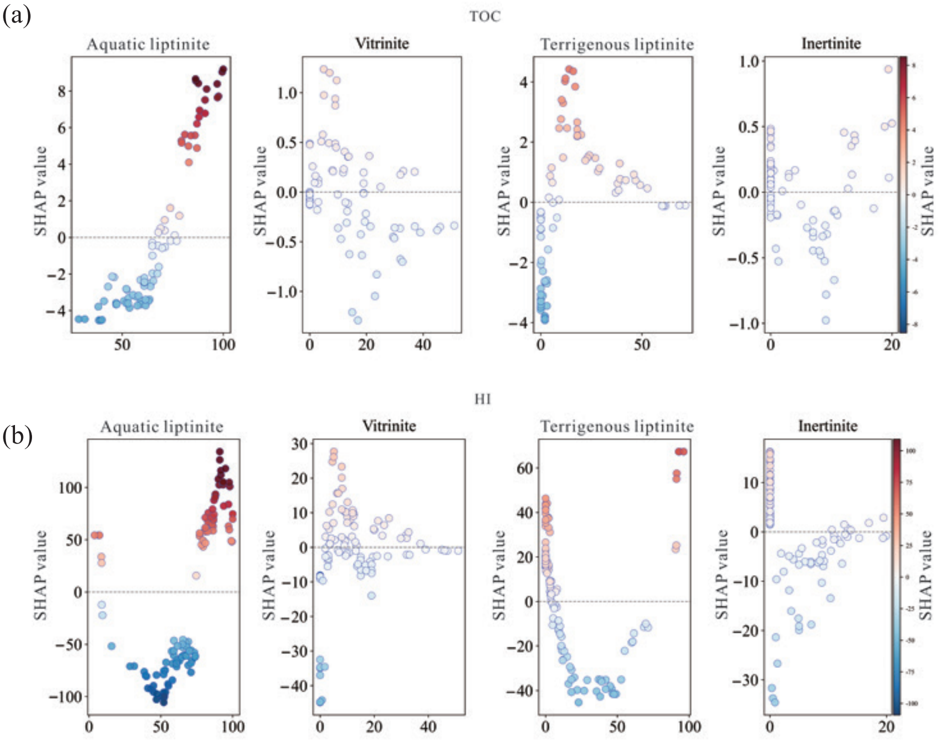

Fig. 6. Dependence plots of influencing factors for TOC (a) and HI (b).

Figure 7 displays four randomly selected SHAP force plots from the actual prediction results of TOC and HI, respectively. The SHAP values decompose the prediction of TOC and HI variation patterns into the sum of influences from each input variable [9].

Figure 7a represents predictions for different TOC contents. Figure 7a1 shows a case of low predicted TOC content. The predicted TOC value is 6.13 wt%, and the true value is 5.04 wt%. Figure 7a2 shows a case of high predicted TOC content. The predicted TOC value is 20.28 wt%, and the true value is 17.30 wt%. Overall, regardless of the increase or decrease in TOC content, aquatic liptinite is the primary influencing factor in TOC content variation. However, when TOC content is low, terrigenous liptinite has a greater influence on TOC, and as TOC content increases, the influence of terrigenous liptinite gradually decreases.

Figure 7b represents predictions for different HI contents. Figure 7b1 shows a case of low predicted HI content. The predicted HI value is 542.01 mg HC/g TOC, and the true value is 545.0 mg HC/g TOC. Figure 7b2 shows a case of high predicted HI content. The predicted HI value is 729.62 mg HC/g TOC, and the true value is 694.85 mg HC/g TOC. Overall, regardless of the increase or decrease in HI content, aquatic liptinite is the

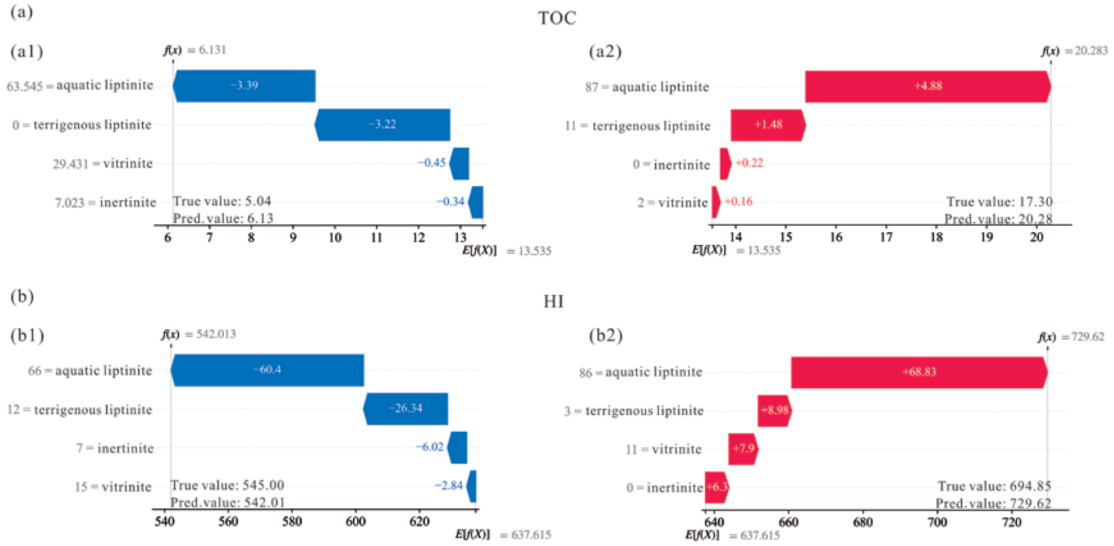

Fig. 7. Explanation of evaluation results based on the SHAP TreeExplainer for TOC (a) and HI (b).

primary influencing factor in HI content variation. However, when HI content is low, terrigenous liptinite has a certain influence on HI, and as HI content increases, the influence of terrigenous liptinite gradually decreases.

4. Discussion

4.1. Contribution of organic macerals to TOC and HI

TOC fundamentally represents the total carbon content of organic matter in oil shale and coal. In oil shale, aquatic liptinite content shows a significant positive correlation with TOC. For every 10% increase in aquatic liptinite content, the TOC of oil shale increases by an average of 5–8 wt% (Fig. 2a). Terrigenous liptinite content in oil shale ranges from 5% to 30%, and its moderate inherent carbon content (72–82%) results in a limited contribution to TOC [35]. However, in low-grade oil shale, a 10% increase in terrigenous liptinite content elevates TOC by 1–3 wt% (Fig. 2a). Based on the scatter plot of TOC/HI versus liptinite, oil shale TOC exhibits a clear positive correlation with liptinite, with a correlation coefficient of $R^2 = 0.563$ (Fig. 8a). Vitrinite content in oil shale varies widely (5–50%), but oil shale with high TOC tends to have lower vitrinite content, showing a minor negative correlation between vitrinite and TOC. Inertinite content in oil shale is < 10%, and its contribution to TOC is much more limited than that of the dominant macerals (Fig. 3a).

In coal, aquatic liptinite content is extremely low, and its contribution to TOC is negligible [15, 17, 21, 36, 37]. Terrigenous liptinite content in coal is relatively low (1–10%) and results in a limited contribution to TOC [35]. Coal TOC shows a poor correlation with liptinite (Fig. 8a). Vitrinite is the most dominant maceral in coal (content 40–90%) (Fig. 3a). Derived from the lignocellulosic tissues of higher plants and with a high inherent carbon content (75–85%), it directly determines the TOC level of coal [44]. Inertinite content in coal is low ($<5\%$), and its contribution to TOC is much more limited than that of the dominant macerals (Fig. 3a).

The HI fundamentally reflects the macroscopic manifestation of hydrogen enrichment in organic matter. Its value is primarily determined by the hydrogen content of organic macerals. The contribution of different macerals directly dictates the oil-generating capacity of oil shale and coal [39–41]. In oil

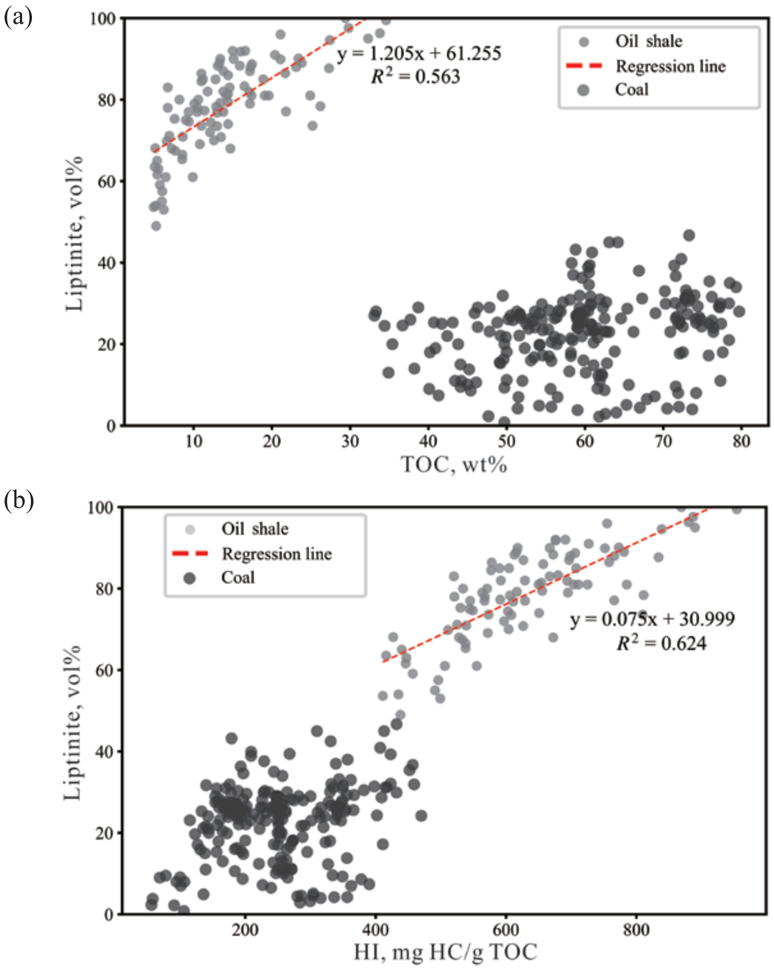

Fig. 8. Scatter plots of TOC vs. liptinite (a) and HI vs. liptinite (b) for oil shale and coal samples.

shale, aquatic liptinite content shows a significant positive correlation with HI. Aquatic liptinite contributes the most to HI, with every 10% increase in its content raising HI by an average of 80–100 mg HC/g TOC (Fig. 2b). Terrigenous liptinite's contribution to HI is secondary to aquatic liptinite; a 10% increase in its content elevates HI by 25–40 mg HC/g TOC, a notably smaller increase than that from aquatic liptinite (Fig. 2b). Based on the relationship between the lipidic group and HI (Fig. 8b), oil shale HI exhibits a clear positive correlation with the lipidic group, with a correlation coefficient of $R^2 = 0.624$. Vitrinite in oil shale exerts a minor inhibitory effect on HI: a 10% increase in its content reduces HI by 60–80 mg HC/g TOC (Fig. 3b). Inertinite content in oil shale is generally below 10%, and its contribution to HI is minor (Fig. 3b).

In coal, aquatic liptinite content is extremely low, making its contribution to HI negligible. Terrigenous liptinite content in coal is relatively low (1–10%). Coal HI shows a poor correlation with the lipidic group (Fig. 10b). Vitrinite is the primary organic maceral in coal (40–90%) (Fig. 3b). Its hydrocarbon generation capacity varies significantly with the degree of coalification [42]. In low-rank coal, vitrinite has a slightly higher hydrogen content, resulting in a more limited inhibitory effect. In high-rank coal, due to intensified aromatization, its inhibitory effect strengthens [43–46]. Inertinite content in coal is typically below 5%, and its contribution to HI is much more limited than that of the dominant macerals (Fig. 3b).

4.2. Key factors controlling oil shale quality

The key organic macerals controlling oil shale quality are primarily aquatic liptinite, followed by minor amounts of terrigenous liptinite and vitrinite. Vitrinite mainly exerts a certain negative influence. Specifically, when TOC < 15 wt%, oil shale quality is jointly controlled by aquatic liptinite and terrigenous liptinite (Fig. 9), indicating that during the depositional period of medium- to low-quality oil shale, influenced by dual supply from aquatic organisms and terrigenous organic matter, the quality of the corresponding oil shale gradually improves with increasing organic matter supply [47–49]. In contrast, when TOC > 15 wt%, the contribution of terrigenous liptinite decreases significantly, and quality is primarily controlled by aquatic liptinite. This suggests that high-quality oil shale forms during periods of minimal terrigenous organic matter influence, where aquatic productivity and effective organic matter preservation are the key factors determining oil shale quality [50–52]. Thus, TOC = 15 wt% can be used as a boundary for distinguishing oil shale quality: high-quality oil shale is primarily controlled by aquatic liptinite, while ordinary oil shale is jointly controlled by aquatic liptinite and terrigenous liptinite. This aligns with the SHAP analysis results, which indicate that when aquatic liptinite content exceeds 70% and terrigenous liptinite content is below 30% in oil shale, both TOC and HI significantly increase (Fig. 6).

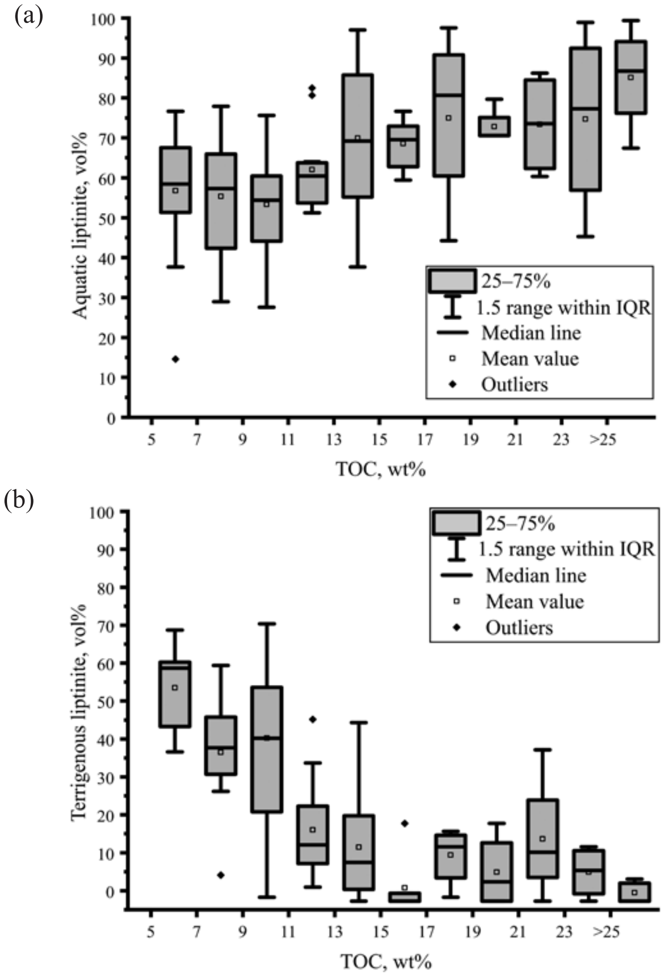

Fig. 9. Box plots of TOC vs. aquatic liptinite (a) and TOC vs. terrigenous liptinite (b) in oil shale.

4.3. Quantitative model of organic maceral contributions to oil shale

The core industrial value of oil shale depends on the oil production potential and economic viability of its organic macerals [53]. From the perspective of hydrocarbon generation [54], only aquatic liptinite, terrigenous liptinite, and vitrinite are considered as organic macerals in oil shale, while inertinite is temporarily excluded from calculations due to its generally negligible content ($\leq 5\%$) and lack of practical contribution to oil yield. The core evaluation metric of the model is the oil production efficiency index of oil shale, which ranges from 0 to 100, with higher values indicating superior oil shale quality.

To quantify the comprehensive contribution of each maceral to oil shale quality, the formula is defined as follows:

$$C = \frac{\mathrm{A}\times P_A + T\times P_T - V\times P_V}{\mathrm{W}\times（\mathrm{A+T+V}）}, \tag{1}$$

where C represents the oil production efficiency index of oil shale, W denotes the contribution weight of organic macerals, A is the percentage content of aquatic liptinite, T is the percentage content of terrigenous liptinite, V is the percentage content of vitrinite, P_A is the unit oil production contribution coefficient of aquatic liptinite, P_T is the unit oil production contribution coefficient of terrigenous liptinite, and P_V is the unit loss coefficient of vitrinite. Based on the SHAP analysis results, the values are set as follows: $W = 0.7$, $P_A = 70$, $P_T = 30$, and $P_V = 130$.

The model calculation results indicate that when $C \geq 80$, the oil shale is classified as premium-grade, with aquatic liptinite content $\geq 85\%$ and vitrinite content $\leq 5\%$.When $60 \leq C < 80$, the oil shale is classified as medium-grade, with aquatic liptinite content between 70% and 85% and vitrinite content between 5% and 10%. When $C < 60$, the oil shale is classified as low-grade, with aquatic liptinite content $< 70\%$ and vitrinite content $> 10\%$.

5. Conclusions

Based on data from immature to low-maturity oil shale and coal samples from multiple basins, this study analyzes the contributions of organic macerals to organic matter abundance and hydrocarbon generation potential, identifies key factors controlling the quality of oil shale and coal, and focuses on interpreting the intrinsic relationships between organic maceral data and TOC/HI using SHAP analysis. A quantitative model for the contribution of organic macerals to the hydrocarbon generation capacity of oil shale was established.

1. Machine learning models were developed based on the relationships between TOC/HI and organic macerals in oil shale. SHAP analysis was used to interpret the model results, confirming that aquatic liptinite has the greatest influence on TOC and HI in oil shale, followed by terrigenous liptinite, while vitrinite exhibits a minor negative influence.
2. Oil shale is dominated by aquatic liptinite and terrigenous liptinite, whereas coal is dominated by vitrinite. High-quality oil shale is primarily controlled by aquatic liptinite, while ordinary oil shale is jointly controlled by aquatic liptinite and terrigenous liptinite. The hydrocarbon generation capacity of oil shale significantly increases when aquatic liptinite content exceeds 70% and terrigenous liptinite content remains below 30%. Vitrinite is the most abundant organic maceral in coal, typically accounting for 50–80%, making it the most critical factor influencing coal quality.
3. Based on these relationships, a quantitative contribution model was constructed to evaluate the hydrocarbon generation capacity of oil shale using organic maceral composition.

Data availability statement

All data used in this article are publicly available. No new data were created or analyzed in this study.

Acknowledgments

This study was supported by the PetroChina Company Limited Science and Technology Project, "Research on New Theories of Overseas Oil and Gas Geology, New Resource Evaluation Technologies, and Advanced Region Selection" (project No. 2023ZZ07), and by the National Natural Science Foundation of China (grant No. 42372125). The publication costs of this article were partially covered by the Estonian Academy of Sciences.

Supplementary online data

Supplementary online data to this article can be found at https:/doi.org/... and includes Appendices 1 and 2.

References

1. Liu, Z., Dong, Q., Ye, S., Zhu, J., Guo, W., Li, D. et al. The situation of oil shale resources in China. *Journal of Jilin University (Earth Science Edition)*, 2006, **36**(6), 869–876.
2. Liu, R., Liu, Z. Oil shale resource situation and multi-purpose development potential in China and abroad. *Journal of Jilin University (Earth Science Edition)*, 2006, **36**(6), 892–898.
3. Liu, Z., Meng, Q., Dong, Q., Zhu, J., Guo, W., Ye, S. et al. Characteristics and resource potential of oil shale in China. *Oil Shale*, 2017, **34**(1), 15–41. https://doi.org/10.3176/oil.2017.1.02
4. Wang, Y., Zhai, G., Bao, S.-J., Ren, S., Ge, M., Zhou, Z. Latest progress and trend forecast of China's shale gas exploration and development. *Acta Geologica Sinica (English Edition)*, 2025, **89**(S1) 211–213. https://doi.org/10.1111/1755-6724.12303_25
5. Radwan, A. E., Yin, S., Hakimi, M. H., Li, H. Petroleum geology of conventional and unconventional resources: introduction. *Geological Journal*, 2023, **58**(11), 3965–3969. https://doi.org/10.1002/gj.4898
6. Murchison, D. G. Recent advances in organic petrology and organic geochemistry: an overview with some reference to 'oil from coal'. *Geological Society, London, Special Publications*, 1987, **32**, 257–302. https://doi.org/10.1144/GSL.SP.1987.032.01.15
7. Suárez-Ruiz, I., Flores, D., Mendonça Filho, J. G., Hackley, P. C. Review and update of the applications of organic petrology: Part 1, geological applications. *International Journal of Coal Geology*, 2012, **99**, 54–112. https://doi.org/10.1016/j.coal.2012.02.004

8. Xiao, L., Li, Z., Xu, L., Wang, L., Yang, Y. Characteristics of organic macerals and their influence on hydrocarbon generation and storage: a case study of continental shale of the Yanchang Formation from the Ordos Basin, China. *Geofluids*, 2021, 5537154. https://doi.org/10.1155/2021/5537154
9. Lundberg, S. M., Lee, S.-I. A unified approach to interpreting model predictions. In *Advances in Neural Information Processing Systems*, 2017, **30**, 4766–4777.
10. Jamaluddin,Wagreich, M.,Schöpfer, K.,Sachsenhofer, R. F.,Maria,Rahmawati, D. Hydrocarbon potential and depositional environment of the Middle Miocene Balikpapan Formation, lower Kutai Basin, Indonesia: sedimentology, calcareous nannofossil, organic geochemistry, and organic petrography integrated approach. *International Journal of Coal Geology*, 2024, **293**, 104591. https://doi.org/10.1016/j.coal.2024.104591
11. Hu, F., Misch, D., Zhang, P., Meng, Q., Sachsenhofer, R. F., Xu, Y. et al. Influence of high-frequency lake level fluctuations on organic matter accumulation in the northern Qaidam Basin, NW China: insights from spectral attribute analysis and geochemistry. *Journal of Asian Earth Sciences*, 2024, **260**, 105937. https://doi.org/10.1016/j.jseaes.2023.105937
12. Cao, T., Liu, H., Xiao, J., Pan, A., Deng, M. Paleoenviromental reconstruction and organic matter accumulation mechanism for Youganwo Formation oil shale in Maoming Basin. *Earth Science*, 2024, **49**(4), 1367–1384. http://dx.doi.org/10.3799/dqkx.2022.260
13. Camacho-Aristizabal, L., Burnaz, L., Castro-Vera, L., Mojica Silva, L., Littke, R. Organic petrology and geochemistry data reveal depositional and thermal history of coal in the Guaduas formation, Colombian Eastern Cordillera. *International Journal of Coal Geology*, 2024, **289**, 104549. https://doi.org/10.1016/j.coal.2024.104549
14. Nie, Y., Fu, X., Liang, J., Wei, H., Chen, Z., Lin, F. et al. The Toarcian Oceanic Anoxic Event in a shelf environment (Eastern Tethys): implications for weathering and redox conditions. *Sedimentary Geology*, 2023, **455**, 106476. https://doi.org/10.1016/j.sedgeo.2023.106476
15. Ajuaba, S., Sachsenhofer, R. F., Meier, V., Gross, D., Schnyder, J., Omodeo-Salé, S. et al. Coaly and lacustrine hydrocarbon source rocks in Permo-Carboniferous graben deposits (Weiach well, northern Switzerland). *Marine and Petroleum Geology*, 2023, **150**, 106147. https://doi.org/10.1016/j.marpetgeo.2023.106147
16. Zhang, P., Misch, D., Meng, Q., Sachsenhofer, R. F., Liu, Z., Jia, J. et al. Lateral changes of organic matter preservation in the lacustrine Qingshankou Formation (Cretaceous Songliao Basin, NE China): evidence for basin segmentation. *International Journal of Coal Geology*, 2022, **254**, 103984. https://doi.org/10.1016/j.coal.2022.103984
17. Fikri, H. N., Sachsenhofer, R. F., Bechtel, A., Gross, D. Coal deposition in the Barito Basin (Southeast Borneo): the Eocene Tanjung Formation compared to the Miocene Warukin Formation. *International Journal of Coal Geology*, 2022, **263**, 104117. https://doi.org/10.1016/j.coal.2022.104117

18. Fikri, H. N., Sachsenhofer, R. F., Bechtel, A., Gross, D. Organic geochemistry and petrography in Miocene coals in the Barito Basin (Tutupan Mine, Indonesia): evidence for astronomic forcing in kerapah type peats. *International Journal of Coal Geology*, 2022, **256**, 103997. https://doi.org/10.1016/j.coal.2022.103997
19. Zhang, P., Misch, D., Hu, F., Kostoglou, N., Sachsenhofer, R. F., Liu, Z. et al. Porosity evolution in organic matter-rich shales (Qingshankou Fm.; Songliao Basin, NE China): implications for shale oil retention. *Marine and Petroleum Geology*, 2021, **130**, 105139. https://doi.org/10.1016/j.marpetgeo.2021.105139
20. Körmös, S., Bechtel, A., Sachsenhofer, R. F., Radovics, B. G., Katalin, M., Félix, S. Petrographic and organic geochemical study of the Eocene Kosd Formation (northern Pannonian Basin): implications for paleoenvironment and hydrocarbon source potential. *International Journal of Coal Geology*, 2020, **228**, 103555. https://doi.org/10.1016/j.coal.2020.103555
21. Song, Y., Liu, Z., Bechtel, A., Sachsenhofer, R. F., Gross, D., Meng, Q. Paleoenvironmental reconstruction of the coal- and oil shale-bearing interval in the lower Cretaceous Muling Formation, Laoheishan Basin, northeast China. *International Journal of Coal Geology*, 2017, **172**, 1–18. https://doi.org/10.1016/j.coal.2017.01.010
22. Song, Y., Bechtel, A., Sachsenhofer, R. F., Gross, D., Liu, Z., Meng, Q. Depositional environment of the Lower Cretaceous Muling Formation of the Laoheishan Basin (NE China): implications from geochemical and petrological analyses. *Organic Geochemistry*, 2017, **104**, 19–34. https://doi.org/10.1016/j.orggeochem.2016.11.008
23. Bai, Y., Liu, Z., Sun, P., Liu, R., Hu, X., Zhou, R. et al. Diverse sedimentary conditions during deposition of coal and oil shale from the Meihe Basin (Eocene, NE China). *Journal of Sedimentary Research*, 2017, **87**(10), 1100–1120. https://doi.org/10.2110/jsr.2017.60
24. Životić, D., Bechtel, A., Sachsenhofer, R. F., Gratzer, R., Radić, D., Obradović, M. et al. Petrological and organic geochemical properties of lignite from the Kolubara and Kostolac basins, Serbia: implication on Grindability Index. *International Journal of Coal Geology*, 2014, **131**, 344–362. https://doi.org/10.1016/j.coal.2014.07.004
25. Strobl, S. A. I., Sachsenhofer, R. F., Bechtel, A., Meng, Q. Paleoenvironment of the Eocene coal seam in the Fushun Basin (NE China): implications from petrography and organic geochemistry. *International Journal of Coal Geology*, 2014, **134–135**, 24–37. https://doi.org/10.1016/j.coal.2014.10.001
26. Li, J. *Study on the Oil Shale Geochemistry of Permian Lucaogou Formation in the Northern Bogda Mountain*. PhD thesis. China University of Geosciences (Beijing), China, 2009.
27. Breiman, L. Random forests. *Machine Learning*, 2001, **45**, 5–32. https://doi.org/10.1023/A:1010933404324
28. Kim, Y., Kim, Y. Explainable heat-related mortality with random forest and SHapley Additive exPlanations (SHAP) models. *Sustainable Cities and Society*, 2022, **79**, 103677. https://doi.org/10.1016/j.scs.2022.103677
29. Lundberg, S. M., Erion, G., Chen, H., DeGrave, A., Prutkin, J. M., Nair, B. et al. From local explanations to global understanding with explainable AI for trees.

Nature Machine Intelligence, 2020, **2**, 56–67. https://doi.org/10.1038/s42256-019-0138-9

30. Jaber, J. O., Amri, A., Ibrahim, K. Experimental investigation of effects of oil shale composition on its calorific value and oil yield. *International Journal of Oil, Gas and Coal Technology*, 2011, **4**(4), 307–321. https://doi.org/10.1504/IJOGCT.2011.043714
31. Mathews, J. P., Krishnamoorthy, V., Louw, E., Tchapda, A. H. N., Castro-Marcano, F., Karri, V. et al. A review of the correlations of coal properties with elemental composition. *Fuel Processing Technology*, 2014, **121**, 104–113. https://doi.org/10.1016/j.fuproc.2014.01.015
32. Gao, B., Wu, X., Zhang, Y., Chen, X., Bian, R., Li, Q. et al. Hydrocarbon generation and evolution characteristics of Triassic Zhangjiatan oil shale in southern Ordos Basin. *Petroleum Geology & Experiment*, 2022, **44**(1), 24–32. https://doi.org/10.11781/sysydz202201024
33. Pollastro, R. M.,Cook, T. A.,Roberts, L. N. R.,Schenk, C. J.,Lewan, M. D. et al. Assessment of undiscovered oil resources in the Devonian-Mississippian Bakken Formation, Williston Basin Province, Montana and North Dakota. U.S. Geological Survey Fact Sheet 2008–3021, 2008. https://doi.org/10.3133/FS20083021
34. Dyni, J. R. Geology and resources of some world oil-shale deposits. *Oil Shale*, 2003, **20**(3), 193–252. https://doi.org/10.3176/oil.2003.3.02
35. Peters, K. E., Walters, C. C., Moldowan, J. M. *The Biomarker Guide: Volume 1, Biomarkers and Isotopes in the Environment and Human History*. Cambridge University Press, 2007.
36. Strobl, S. A. I., Sachsenhofer, R. F., Bechtel, A., Meng, Q., Sun, P. Deposition of coal and oil shale in NE China: the Eocene Huadian Basin compared to the coeval Fushun Basin. *Marine and Petroleum Geology*, 2015, **64**, 347–362. https://doi.org/10.1016/j.marpetgeo.2015.03.014
37. Zdravkov, A., Bechtel, A., Sachsenhofer, R. F., Kortenski, J. Palaeoenvironmental implications of coal formation in Dobrudzha Basin, Bulgaria: insights from organic petrological and geochemical properties. *International Journal of Coal Geology*, 2017, **180**, 1–17. https://doi.org/10.1016/j.coal.2017.07.004
38. Stach, E. *Stach's Textbook of Coal Petrology*. 3rd ed. Gebrüder Borntraeger, Berlin-Stuttgart, 1997.
39. Taylor, G. H., Teichmuller, M., Davis, A., Diessel, C. F. K., Littke, R., Robert, P. *Organic Petrology*. Gebruder Borntraeger, Berlin, Stutgart, 1998.
40. Kalkreuth, W., Holz, M., Mexias, A., Balbinot, M., Levandowski, J., Willett, J. et al. Depositional setting, petrology and chemistry of Permian coals from the Paraná Basin: 2. South Santa Catarina Coalfield, Brazil. *International Journal of Coal Geology*, 2010, **84**(3–4), 213–236. https://doi.org/10.1016/j.coal.2010.08.008
41. Liu, C., Zhao, W., Sun, L., Wang, X., Sun, Y., Zhang, Y. et al. Geochemical assessment of the newly discovered oil-type shale in the Shuangcheng area of the northern Songliao Basin, China. *Journal of Petroleum Science and Engineering*, 2021, **196**, 107755. https://doi.org/10.1016/j.petrol.2020.107755

42. Yin, Z., Xu, H., Chen, Y., Zhao, T., Wu, J. Experimental simulate on hydrogen production of different coals in underground coal gasification. *International Journal of Hydrogen Energy*, 2023, **48**(19), 6975–6985. https://doi.org/10.1016/j.ijhydene.2022.03.205
43. Stanger, R., Xie, W., Wall, T., Lucas, J., Mahoney, M. Dynamic behaviour of coal macerals during pyrolysis – associations between physical, thermal and chemical changes. *Proceedings of the Combustion Institute*, 2013, **34**(2), 2393–2400. https://doi.org/10.1016/j.proci.2012.07.003
44. Liu, Y., Zhu, Y., Liu, S., Chen, S., Li, W., Wang, Y. Molecular structure controls on micropore evolution in coal vitrinite during coalification. *International Journal of Coal Geology*, 2018, **199**, 19–30. https://doi.org/10.1016/j.coal.2018.09.012
45. Xie, K.-C. *Structure and Reactivity of Coal: A Survey of Selected Chinese Coals*. Science Press, Beijing, 2002.
46. Wang, A., Huang, J., Zhao, M., Liu, Y., Cao, D. et al. Effects of functional groups in coal with different vitrinite/inertinite ratios on pyrolysis products. *ACS Omega*, 2023, **8**(20), 18202–18211. https://doi.org/10.1021/acsomega.3c01635
47. Bowker, K. A. Barnett shale gas production, Fort Worth Basin: issues and discussion. *AAPG Bulletin*, 2007, **91**(4), 523–533. https://doi.org/10.1306/06190606018
48. Hutton, A. C., Kantsler, A. J., Cook, A. C., McKirdy, D. M. Organic matter in oil shales. *The APPEA Journal*, 1980, **20**(1), 44–67.
49. Sun, P., Sachsenhofer, R. F., Liu, Z., Strobl, S. A. I., Meng, Q., Liu, R. et al. Organic matter accumulation in the oil shale-and coal-bearing Huadian Basin (Eocene; NE China). *International Journal of Coal Geology*, 2013, **105**, 1–15. https://doi.org/10.1016/j.coal.2012.11.009
50. Jin, J., Wang, J., Meng, Y., Sun, P., Liu, Z., Li, Y. et al. Main controlling factors and development model of the oil shale deposits in the Late Permian Lucaogou Formation, Junggar Basin (NW China). *ACS Earth and Space Chemistry*, 2002, **6**(4), 1080–1094. https://doi.org/10.1021/acsearthspacechem.2c00015
51. Shang, F., Zhou, H., Liu, Y., Zhou, X., Wang, L., Bi, H. et al. A discussion on the organic matter enrichment model of the Nenjiang Formation, Songliao Basin: a case study of oil shale in the 1st and 2nd members of the Nenjiang Formation. *Geology in China*, 2020, **47**(1), 236–248. https://doi.org/10.12029/gc20200119
52. Wang, H., Niu, D., Luan, Z., Dang, H., Pan, X., Sun, P. Kinetic characteristics of secondary hydrocarbon generation from oil shale and coal at different maturation stages: insights from open-system pyrolysis. *International Journal of Coal Geology*, 2025, **308**, 104845. https://doi.org/10.1016/j.coal.2025.104845
53. Liu, B., Teng, J., Mastalerz, M. Maceral control on the hydrocarbon generation potential of lacustrine shales: a case study of the Chang 7 Member of the Triassic Yanchang Formation, Ordos Basin, North China. *Energies*, 2023, **16**(2), 636. https://doi.org/10.3390/en16020636
54. Lin, Z.-Z., Li, J.-Q., Lu, S.-F., Hu, Q.-H., Zhang, P.-F., Wang, J.-J. et al. The occurrence characteristics of oil in shales matrix from organic geochemical screening data and pore structure properties: an experimental study. *Petroleum Science*, 2024, **21**(1), 1–13. https://doi.org/10.1016/j.petsci.2023.09.002

Oil Shale, 2026, 43, 3, 321–334 https://doi.org/10.3176/oil.2026.3.05

Kerogen destruction and partial transfer of metals to shale oil: detection and quantification

Omar S. Al-Ayed[a]*, Omar Loai Alnsour[b], Eyad S. M. Abu-Nameh[b]

[a] Department of Chemical Engineering, Faculty of Engineering Technology, Al-Balqa Applied University, Amman Marka 11134, Jordan
[b] Department of Chemistry, Faculty of Science, Al-Balqa Applied University, As-Salt 19117, Jordan

Received 2 February 2026, accepted 1 July 2026, available online 3 August 2026

Abstract. *Oil shale is pyrolyzed to investigate the transfer of selected metals (Fe, V, Ni, Mn, and Pb) to shale oil. Several heating rates are employed to study the transfer process during the heating of oil shale under a nitrogen environment. The migration or transfer of Fe, V, Ni, Mn, and Pb from oil shale to shale oil is investigated. These metals are redistributed between shale oil and spent shale. The transfers are studied as a function of heating rates of 5, 10, 15, and 20 °C/min. Metals embedded in oil shale are found to be transferable to shale oil during pyrolysis. The Fe concentration levels in shale oil are 59.4, 35.69, 34.14, and 25.29 ppm at 5, 10, 15, and 20 °C/min, respectively. The transfer of Fe shows a decreasing trend with heating rate. The concentrations of As in shale oil are 10.09, 13.88, 12.2, and 11.04 ppm, showing a decreasing trend at 10, 15, and 20 °C/min. On the other hand, the percentage recovery of Fe is $> 93.6\%$ and $< 109.3\%$, while that of As is $> 79.3\%$ and $< 83.99\%$. The concentrations of Mn and Pb in shale oil are < 1 ppm. The concentration of Ni in shale oil is < 6.04 ppm at 10 °C/min, whereas it decreases to 3.14 ppm at 20 °C/min. The percentage recovery of Ni ranges from > 81.48 to < 84.13. Finally, low concentrations of V in shale oil are detected. These concentrations are 1.13, 1.45, 0.77, and 1.76 ppm at 5, 10, 15, and 20 °C/min, respectively. The percentage recovery of V is $> 76.88\%$ and $< 86.31\%$.*

Keywords: *shale oil, heating rate, metals transfer, oil shale, metals migration.*

1. Introduction

Shale oil is an unconventional condensed liquid hydrocarbon product obtained from the oil shale pyrolysis process [1–2]. Kerogen, the organic portion of

---

* Corresponding author, omar.alayed@bau.edu.jo

the oil shale, decomposes to hydrocarbon vapors, incondensable gases, and retorted water if subjected to pyrolysis in the temperature range of 350 to 550 °C. The gaseous hydrocarbons generated include CH_4, C_2H_6, C_2H_4, C_3H_8, C_3H_6, n-C_4H_{10}, i-C_4H_{10}, C_4H_8 isomers, and traces of light hydrocarbons. These gases are condensable at room temperature and pyrolysis product condensation conditions. Hydrogen gas and other non-condensable gases such as NO, NO_2, SO_2, CO, CO_2, H_2S, and NH_3 are also generated depending upon the oil shale origin and reaction conditions [3]. On the other hand, different hydrocarbon classes that make up shale oil are also found. These classes include aliphatics (alkanes, alkenes, alkynes, and cycloalkanes), aromatics (benzoids and non-benzoids), and asphaltenes (the insoluble fraction in normal n-alkanes, but soluble in toluene and benzene) [4–7]. The density of the produced shale oil varies between 0.9587 and 0.9974 g/cm^3 [8, 9]. Oja et al. [9] reported that the densities for kukersite, Kashpir, and Green River shale oils increased with increasing boiling point from 0.7055 to 0.9887 g/cm^3, 0.8649 to 1.0031 g/cm^3, and 0.8276 to 0.9506 g/cm^3, respectively. El-Lajjun and Sultani shale oils were reported to have average densities of 0.9668 and 0.964 g/cm^3, respectively [10].

Jordanian oil shale contains several metals as confirmed by XRF results [11]. The XRF analysis of Attarat, Sultani, and El-Lajjun oil shales confirmed the presence of various metals such as Ni, V, Mn, Fe, As, and Pb, as reported by several authors [11–14]. The concentrations of these elements range from below 1 ppm up to about 1000 ppm. Very few researchers have studied the possible transfer of some of these elements to shale oil [15–17]. In a study by Abu-Nameh et al. [17], the transfer of 20 elements was detected in shale oil produced from El-Lajjun, Sultani, and Attarat oil shales. The most transferred element was Fe, followed by Zn, V, As, Cr, and Pb. In a separate study by Wang et al. [18], it was found that Pb transferred to water during in-situ pyrolysis, and it was reported that the rate of transfer increased with increasing temperature. This is an indication that shale oil metals get affected by the pyrolysis conditions and migrate into liquid products such as shale oil and chemical water. Liu et al. [19] studied the volatility of some elements during coal pyrolysis and reported that fuel characteristics depend upon pyrolysis conditions such as final pyrolysis temperature, heating rate, and pyrolysis environment. Migration of trace elements during Mongolian oil shale pyrolysis was investigated by Bai et al. [20]. They found that the rate of heavy metals decreases with increasing specific surface area due to the progress of the pyrolysis process. The developed pores during pyrolysis contributed to the re-adsorption of the released heavy metal elements originating from kerogen thermal cracking. The migration of trace elements in oil shale during pyrolysis is related both to their content and to the final pyrolysis temperature.

The presence of metals in oil shale as a part of ore or as oxides affects the secondary reactions of the generated hydrocarbon vapors. During the pyrolysis process, kerogen molecules crack to give hydrocarbon vapors, which upon condensation produce shale oil. During the generation process and the transport of these products, the ore or metal oxides influence chemical reactions. The inert gas in the reaction environment and the residence time of the generated hydrocarbons inside the solid kerogen affect the distribution of the produced hydrocarbons into gases and liquid products [21–23].

Studies using inductively coupled plasma optical emission spectroscopy (ICP-OES) have indicated that shale oil contains metals such as Fe, Mn, As, Pb, Ni, and Zn [17]. The presence of these elements in shale oil limits its usage as a fuel in engines. In a separate study by Dan et al. [24], using laser ablation inductively coupled plasma mass spectrometry (LA-ICP-MS), the authors reported the presence of 19 elements in oil shale and its solid waste. These elements include Mn, As, Pb, Ni, Zn, and many others. Unfortunately, these authors did not study the presence of metals in shale oil. The final pyrolysis temperature has an impact on the oil shale content of trace element migration. Trace element migration and volatility in semi-coke were studied as a function of final pyrolysis temperature, and it was found that higher migration indicated a higher rate of trace element transfer to gas and liquid phases. The migration of metals from coal during pyrolysis was found to be influenced by the pyrolysis conditions [25].

In this research work, the transfer of metals from oil shale during pyrolysis will be investigated. The transfer of elements will be studied as a function of the heating rate of oil shale during the pyrolysis process for some Jordanian oil shales.

2. Materials and methods

2.1. Oil shale pyrolysis

The oil shale sample was obtained from the Attarat Um Al-Ghudran area (31°16′08″ N, 36°26′52″ E). Chunk pieces were crushed in a jaw crusher to smaller sizes. The crushed samples were mixed and sieved to the desired size of 4 ± 1.5 mm. This step was performed to create a uniform composite sample that retained the homogeneity of the oil shale.

The proximate and ultimate analyses of the Attarat oil shale are shown in Table 1. The proximate analysis of the study sample indicates that 63.15 wt.%

Table 1. Proximate and ultimate analyses of Attarat oil shale

Proximate analysis components	**Ash**	**Volatile matter**	**Moisture**	**Fixed carbon**
wt.%	63.15	34.52	0.88	1.45
Ultimate analysis (elemental)	C	H	S	N
wt.%	17.89	1.75	3.02	2.76

of the sample is ash. The major composition of the ash is calcium oxide and silica, in addition to other minor components such as iron and aluminum oxides etc. [33]. The fixed carbon is the solid carbon that remains in the spent ash (unextractable carbon). According to elemental analysis, C accounts for 17.9 wt.%, followed by S at 3.02 wt.%, while N and H account for 2.76 and 1.75 wt.%, respectively.

The retort consisted of a stainless steel pipe with an inner diameter of 75 mm. The length of the retort was 300 mm. A special stainless steel perforated basket was fabricated and placed in the middle of the retort to contain the oil shale sample. A sample size of 300 g or more of oil shale was placed into the basket. The insulated retort was heated using an electrical heater wrapped around the stainless steel retort. The pyrolysis experiments were conducted at a final temperature of 550 °C. The heating rates were 5, 10, 15, and 20 °C/min. The temperature of the sample inside the retort was measured using type K thermocouple, and the process was regulated with a microcontroller (Arduino Uno) integrated into the system. Nitrogen gas flow rate was 200 mL/min, and the oil shale sample mass was approximately 300 g for each run. The hydrocarbon vapors were condensed using a circulating coolant operating at 5 °C or lower. The condensed shale oil, spent shale, and oil shale samples were subjected to metal detection and quantification using an inductively coupled plasma mass spectrometer (ICP-MS), specifically the Agilent 7500 model. The experimental work was performed in triplicate, and an overall material balance is indicated in Table 2. The masses of shale oil and water were measured together since it was not possible to separate the water from the shale oil due to the small amounts of water generated. It is clear from the data that oil yield fluctuations were heating-rate dependent. The mass of gases increased at the expense of shale oil with increasing heating rate.

Table 2. Pyrolysis variables and mass-balance results

Run No.	Heating rate, °C/min	Final temperature, °C	Mass of sample, g	Mass of shale oil and water, g	Mass of spent ash, g	Mass of non-condensable gases by difference, g	Oil yield, %
1	5	550	300	73	210	17	23.63
2		550	300	71	214	15	22.98
3		550	300	77	207	16	24.92
4	10	550	300	71	207	22	22.98
5		550	300	69	210	21	22.33
6		550	300	66	211	23	21.36

Continued on the next page

Table 2. *Continued*

Run No.	Heating rate, °C/min	Final temperature, °C	Mass of sample, g	Mass of shale oil and water, g	Mass of spent ash, g	Mass of non-condensable gases by difference, g	Oil yield, %
7	15	550	300	52	223	25	16.83
8		550	300	60	212	28	19.42
9		550	300	55	215	30	17.80
10	20	550	300	45	222	33	14.57
11		550	300	43	226	31	13.92
12		550	300	48	216	36	15.54

2.2. Sample preparation for metal analysis

To determine the metal content of the solid materials such as oil shale and spent shale after the pyrolysis process, acid digestion and metal extraction were conducted. A microwave digestion system (Ethos Easy, Milestone, Italy) with temperature feedback control up to 300 °C using a temperature sensor was employed. Oil shale was combusted at 950 °C to volatilize the different forms of water in oil shale, volatile matter, and the kerogen organic content. Tests were performed on particles of samples after grinding them using an Agate ball mill to pass 200 mesh (75 µm).

For each test sample, volumes of 6.0 to 12.0 mL of HNO_3, 1.0 to 3.0 mL of HF or 1.0 to 3.0 mL HCl, and 1.0 to 3.0 mL of H_2O_2 were added using a micropipette. The samples were mixed and transferred to the microwave digestion apparatus. A programmed method consisting of heating for 40 min to reach 230 °C, maintaining this temperature for 30 min, followed by cooling and centrifugation at 2000–3000 rpm for 10 min, was used. Upon completion, the sample was ready for ICP-MS analysis to determine the predefined metals, (Fe, Mn, Pb, Ni, and V).

The analysis of oil shale, spent shale, and shale oil samples, along with the determination of target metals (Fe, Mn, As, Pb, Ni, and V), was performed using an ICP-MS, specifically the Agilent 7500 model equipped with a Babington nebulizer due to the instrument's ability to perform multi-element analysis and to measure elements at trace levels. The specific conditions and parameters utilized during the ICP-MS analysis are outlined in Table 3. All measurements were carried out at the Jordan Atomic Energy Commission located in Amman, Jordan.

Table 3. Operating conditions and measurement parameters for ICP-MS

<table>
<tr><th colspan="2">Parameter</th><th colspan="4">Specification</th></tr>
<tr><td colspan="2">Spectrometer</td><td colspan="4">Agilent 7500 series ICP-MS</td></tr>
<tr><td colspan="2">Nebulizer</td><td colspan="4">Babington</td></tr>
<tr><td colspan="2">Spray chamber</td><td colspan="4">Quartz Scott-type</td></tr>
<tr><td colspan="2">Mass analyzer</td><td colspan="4">Quadrupole</td></tr>
<tr><td colspan="2">Radio frequency power, kW</td><td colspan="4">1330</td></tr>
<tr><td colspan="2">Nebulizer gas flow, L/min</td><td colspan="4">1</td></tr>
<tr><td colspan="2">Auxiliary gas flow, L/min</td><td colspan="4">1</td></tr>
<tr><td colspan="2">Argon gas tank pressure, kPa</td><td colspan="4">811</td></tr>
<tr><td colspan="6">Measured mass/charge, m/z</td></tr>
<tr><td>Fe</td><td>Mn</td><td>Ni</td><td>V</td><td>As</td><td>Pb</td></tr>
<tr><td>57</td><td>55</td><td>60</td><td>51</td><td>75</td><td>208</td></tr>
</table>

3. Results and discussion

Generally, oil shale is composed of organic and inorganic fractions that contain metals and rare earth elements [26], which are embedded in both fraction structures. For example, compounds such as $C_{20}H_{14}N_4Ni$ (nickel porphyrins, where the Ni atom is incorporated into the porphyrin framework [27]) and octaethyl nickel porphyrin ($C_{34}H_{44}N_4Ni$) [28] may be present. These compounds may exist in different forms such as the heavy fraction of shale oil, or organic extracts of oil shale, and could be associated with kerogen and bitumen in oil shale. On the other hand, V can also be present in different forms in crude oils and oil shale/shale oil, such as $C_{20}H_{12}N_4VO$ (vanadyl porphyrins), nitrogen heterocycles, or vanadium-asphaltene complexes either in the heavy fraction of shale oil or in bitumen [29]. As is present in crude oil and shale oil. Several authors have investigated the presence of As in crude and shale oils and reported the presence of methylated As compounds, AsH_2CH_3, $AsH\ (CH_3)_{2\text{-}3}$, and roxarsone (4-hydroxy-3-nitrophenylarsonic acid) ($C_6H_6AsNO_6$) [30]. Typical concentrations in shale oil ranged between a few ppm and more than 100 ppm [31, 32]. These authors claimed that thermally stable metal arsenide and metal arsenous sulfides are removed from shale oil by hydrocatalytic processing. The possibility of As solubility in the retorted water renders the spent catalyst as industrial waste.

The main interest in the present work is to trace the transfer of some metals from the oil shale solid material to shale oil and conduct an elemental material balance of the selected migrated elements during the pyrolysis process. The presence of metals such as Fe, Mn, Pb, Ni, and V could harm the operation of combustion engines.

The experimental runs were conducted for 300 g of fresh oil shale samples. A material balance was conducted on all runs since the spent shale, shale oil, and water liquids were collected, weighed, and the gas mass was calculated by difference. A material balance on the intended elements was also conducted (Table 4).

According to the results presented in Table 4, an elemental material balance using ICP-MS data is reported. The elemental mass balance was performed according to Eq. (1):

$$Metal\ mass\ (g) = sample\ mass\ (g) \times ppm \times 10^{-6}, \text{Eqs} \tag{1}$$

$$\%\ recovery = \frac{(mass\ in\ spent\ \text{shale} + mass\ in\ shale\ oil)}{(mass\ in\ oil\ shale)} \times 100. \tag{2}$$

The ICP-MS results for each investigated elemental metal, reported as ppm values, are presented in Table 4. These concentrations in ppm are used in Eq. (1) for calculating the metal mass. The mass of the sample (g) used in the equation is the average of triplicate tests using ICP-MS. According to this average value, the percentage recovery is calculated. Since the heating rate is thought to play a role in the rate of metal transfer to shale oil, the data in Table 4 are also presented as a function of heating rate. Before discussing the transfer of metals from oil shale to liquid, tests were conducted to determine the metal content of the oil shale rock. In Table 4, the metal content of the oil shale sample material indicates that the concentrations in ppm for V, Mn, Ni, As, Pb, and Fe are 342.2, 21.28, 171.76, 18.38, 3.26, and 2969, respectively. As clearly presented in column 6 of Table 4, the percentage recovery (mass balance) calculated according to Eq. (2) for these metals fluctuated between 76.9% for V and 109.3% for Fe. These elemental mass balances are reported without any manipulations or alterations of the experimental findings. The ppm readings obtained by ICP-MS are substituted directly into Eq. (1) to obtain the elemental mass balances. These results are based on the original charged oil shale sample of 300 g. The percentage recovery of V is the lowest among all studied elements and ranges from 76.9 to 86.3%, although V has the lowest atomic weight (50.94). This low recovery could be due to a low rate of metal transfer to shale oil. As it can be calculated from Table 4, the transfer of V to shale oil is < 0.52% of the original oil shale sample.

Table 4. V, Mn, Ni, As, Pb, and Fe concentrations in oil shale and spent shale as a function of heating rates

Mass concentrations, ppm					Metal recovery, %	Heating rate, °C/min
Metal / atomic weight	**Oil shale**	**Spent shale**	**Shale oil**	**Gases**		
V/50.94	342.2	390.8	1.1	0	78.4	5
		376.6	1.6	0	76.9	10
		371.7	0.8	0	78.5	15
		400.0	1.8	0	86.3	20
Mn/54.94	21.3	28.7	< 1	0	86.8	5
		29.0	< 1	0	94.9	10
		25.1	< 1	0	85.0	15
		24.6	< 1	0	85.4	20
Ni/58.69	171.8	208.9	5.5	0	81.5	5
		199.7	6.0	0	81.9	10
		197.9	3.4	0	84.0	15
		195.3	3.1	0	84.1	20
As/74.92	18.4	18.4	10.1	0	84.0	5
		17.2	13.9	0	82.7	10
		17.6	12.2	0	81.3	15
		17.5	11.0	0	79.3	20
Pb/207.2	3.3	4.5	< 1	0	88.3	5
		4.0	< 1	0	85.2	10
		4.1	< 1	0	90.4	15
		4.0	< 1	0	90.8	20
Fe/56.8	2969	4501.7	59.4	0	93.6	5
		3977.0	35.7	0	93.7	10
		4482.7	34.1	0	109.3	15
		4162.3	25.3	0	103.5	20

As evident in Table 4, the transfer of V to shale oil did not show a clear trend with the heating rates studied, although it decreased with increased rates of 10 and 15 °C/min and then increased at 20 °C/min. The largest percentage recovery was observed for Fe, fluctuating between 93.6% and 109.3%. It should be noted that the Fe concentration in the oil shale sample is high, reaching 0.3% of the total oil shale mass.

3.1. Spent shale

Figure 1(a) presents the concentrations of V, Ni, and Fe in the spent shale. Calculating the average metal percentages for V, Ni, and Fe that remained in the spent shale considering the studied heating rates gives values of 79.94%, 82.22%, and 99.75%, respectively.

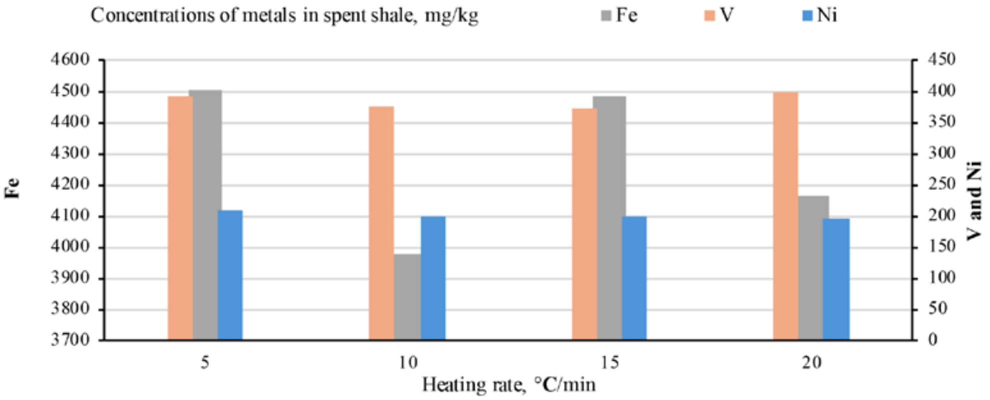

Fig. 1(a). Concentrations of metals in spent shale, ppm.

The concentration of Ni in oil shale is 171.76 ppm, and the concentration remaining in the spent shale is 197.6 ppm. These figures indicate that 82.22% of Ni is not transferred and remains in the solid material. Similarly, from Fig. 1(a), the concentration of Fe remaining in the spent shale is 99.75% of the original oil shale content.

The transfer of Mn to shale oil from oil shale during pyrolysis is < 1 ppm and the concentration of Mn remaining in the spent shale is 88.04% based on Table 4 data for material balance calculations. From Fig. 1(a) and the material balance calculations, no definite relationship exists between the heating rate and the concentrations of these elements remaining in the spent shale.

The concentrations of Mn, As, and Pb in the spent shale after pyrolyzing oil shale are depicted in Fig. 1(b). The concentrations of these elements fluctuate between 24.63–28.97, 17.24–18.5, and 3.98–4.08 ppm, respectively. These values do not show any relationship between the concentrations of these metals remaining in the spent shale and the heating rates. The average percentage of Mn remaining in the spent shale according to the mass balance in Table 4 is 88.04%, while the average percentage of As and Pb in spent shale are 68.78% and 88.67%, respectively.

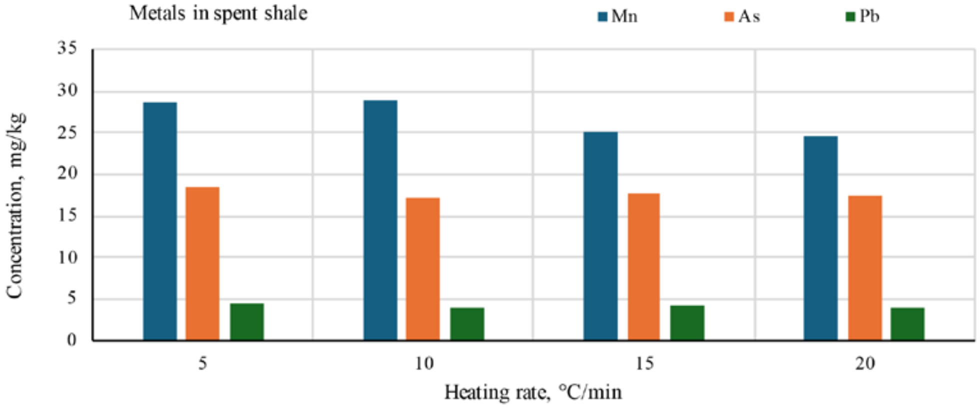

Fig. 1(b). Concentrations of metals in spent shale, ppm.

3.2. Shale oil

The concentrations of Fe, V, Ni, and As in shale oil are depicted in Fig. 2. The concentrations of Mn and Pb are not reported since their concentrations as detected by ICP-MS are < 1 ppm. The maximum concentration of Fe is 59.4 ppm in shale oil as reported at a heating rate of 5 °C/min and depicted in Fig. 2. The concentrations of Fe in shale oil at 10, 15, and 20 °C/min are 35.69, 34.14, and 25.29 ppm, respectively. These concentrations show a decreasing trend with increasing heating rates. The concentrations of V are 1.1, 1.5, 0.8,

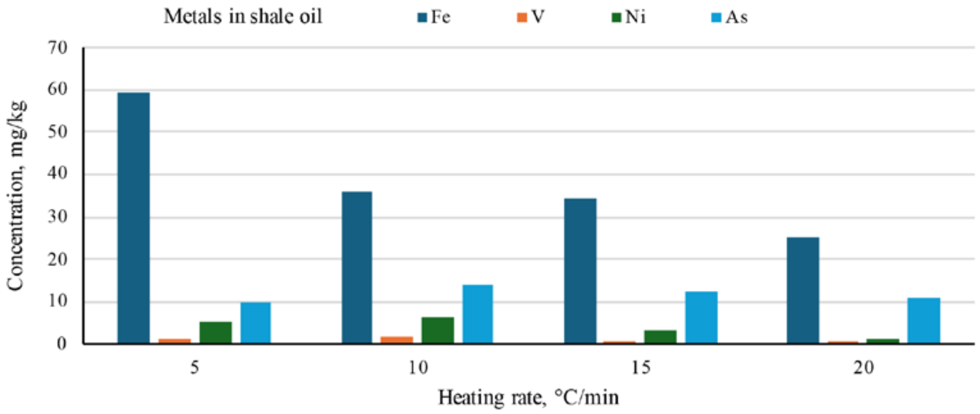

Fig. 2. Concentrations of metals in shale oil, ppm.

and 1.8 ppm at 5, 10, 15, and 20 °C/min, respectively. At a heating rate of 5 °C/min, the concentrations of Ni and As are 5.5 and 10.1 ppm, respectively, while at 10 °C/min, the corresponding concentrations are 6.0 and 13.9 ppm. At 15 °C/min, the concentrations of Ni and As are 3.4 and 12.2 ppm, respectively. Finally, at 20 °C/min, the corresponding concentrations are 3.1 and 11.0 ppm. These concentrations for Fe, V, Ni, and As represent 0.277%, 0.0740%, 0.56%, and 0.0134% of the total content of shale oil, respectively. In general, there is no clear trend relating to metal concentrations in shale oil with the heating rate.

4. Conclusions

The transfer of certain metals embedded in oil shale to shale oil during pyrolysis was investigated for Attarat oil shale. It has been proved that Fe, V, Ni, Mn, Pb, and As are transferable during pyrolysis. The elemental mass balances have shown acceptable values. The recovery of these elements (transferred to shale oil and remaining in the spent shale) varied between 76.9% for V and 109.26% for Fe. The transferred mass of these elements did not show a clear trend with 5, 10, 15, and 20 °C/min heating rates. Some increasing and decreasing trends were observed for some elements with consecutive heating rate values. The lower values of metal concentrations in shale oil could be influenced by other inputs or reaction conditions. Further investigations are required to assess the transfer of metals present in oil shale at higher heating rates, different final pyrolysis temperatures, and probably different reaction environments such as helium, carbon dioxide, and hydrogen gas, as well as particle size and the subsequent diffusional influences on reaction kinetics and kerogen decomposition, as recommended by previous researchers.

Data availability statement

All data used in this article are publicly available. No new data were created or analyzed in this study.

Acknowledgments

The authors acknowledge the support and assistance of the Jordan Atomic Energy Commission for analyzing the samples. The publication costs of this article were covered by the Estonian Academy of Sciences.

References

1. Al-Ayed, O. S., Suliman, M. R., Rahman, N. A. Kinetic modeling of liquid generation from oil shale in fixed bed retort. *Applied Energy*, 2010, **87**(7), 2273–2277. https://doi.org/10.1016/j.apenergy.2010.02.006
2. Wang, S., Jiang, A., Han, X., Tong, J. Effect of residence time on products yield and characteristics of shale oil and gases produced by low-temperature retorting of Dachengzi oil shale. *Oil Shale*, 2013, **30**(4), 501–516. https://doi.org/10.3176/oil.2013.4.04
3. Pan, L., Dai, F., Pei, S., Huang, J., Liu, S. Influence of particle size and temperature on the yield and composition of products from the pyrolysis of Jimsar (China) oil shale. *Journal of Analytical and Applied Pyrolysis*, 2021, **157**, 105211. https://doi.org/10.1016/j.jaap.2021.105211
4. Wallman, P. H., Tamm, P. W., Spars, B. G. Oil shale retorting kinetics. In *Oil Shale, Tar Sand, and Related Materials* (Stauffer, H. C., ed.). American Chemical Society, Washington, 1981, 93–113.
5. Trejo, F., Ancheyta, J., Centeno, G., Marroquín, G. Effect of hydrotreating conditions on Maya asphaltenes composition and structural parameters. *Catalysis Today*, 2005, **109**(1–4), 178–184. https://doi.org/10.1016/j.cattod.2005.08.013
6. Ancheyta, J., Centeno, G., Trejo, F., Marroquín, G. Changes in asphaltene properties during hydrotreating of heavy crudes. *Energy & Fuels*, 2003, **17**(5), 1233–1238. https://doi.org/10.1021/ef030023
7. Amer, M. W., Alhesan, J. S. A., Marshall, M., Awwad, A. M., Al-Ayed, O. S. Characterization of Jordanian oil shale and variation in oil properties with pyrolysis temperature. *Journal of Analytical and Applied Pyrolysis*, 2019, **140**, 219–226. https://doi.org/10.1016/j.jaap.2019.03.019
8. Zuo, P., Qu, S., Shen, W. Asphaltenes: separations, structural analysis and applications. *Journal of Energy Chemistry*, 2019, **34**, 186–207. https://doi.org/10.1016/j.jechem.2018.10.004
9. Oja, V., Rooleht, R., Baird, Z. S. Physical and thermodynamic properties of kukersite pyrolysis shale oil: literature review. *Oil Shale*, 2016, **33**(2), 184–197. https://doi.org/10.3176/oil.2016.2.06
10. Al-Jaraden, T., Ayadi, O., Alahmer, A. Towards sustainable shale oil recovery in Jordan: an evaluation of renewable energy sources for in-situ extraction. *International Journal of Thermofluids*, 2023, **20**, 100446. https://doi.org/10.1016/j.ijft.2023.100446
11. Ibrahim, K. M., Rahman, H. A. Geochemistry and mineralogy of oil shale from Attarat Umm Ghudran area, Jordan. *Advance Engineering Science*, 2023, **55**(1), 3209–3229.
12. Hamarneh, Y. *Oil Shale Resources Development in Jordan*. Ministry of Energy and Mineral Resources, Natural Resources Authority, 1998.
13. Ibrahim, K. M., Aljurf, S., Rahman, H. B. A., Gülamber, C. Exploration and evaluation of oil shale resources from Attarat area, central Jordan. In *IMCET 2019*, 16–19 April 2019, Antalya, Turkey, 1116–1128.

14. El-Hasan, T., Abu-Jaber, N., Abdelhadi, N. Hazardous toxic elements mobility in burned oil shale ash and attempts to attain short- and long-term solidification. *Oil Shale*, 2019, **36**(2S), 226–249. https://doi.org/10.3176/oil.2019.2S.12
15. Al-Ayed, O. S., Hajarat, R. A. Shale oil: its present role in the world energy mix. *Global Journal of Energy Technology Research Updates*, 2018, **5**, 11–18. https://doi.org/10.15377/2409-5818.2018.05.2
16. Al-Ayed, O. S., Kunzru, D. Cyclohexane dehydrogenation on a nickel catalyst: kinetics and catalyst fouling. *Journal of Chemical Technology and Biotechnology*, 1988, **43**(1), 23–38. https://doi.org/10.1002/jctb.280430104
17. Abu-Nameh, E. S. M., Al-Ayed, O. S., Jadallah, A. Determination of selected elements in shale oil liquid. *Oil Shale*, 2019, **36**(2S), 179–187. https://doi.org/10.3176/oil.2019.2S.08
18. Wang, H., Zhang, W., Qiu, S., Liang, X. Release characteristics of Pb and BETX from in situ oil shale transformation on groundwater environment. *Scientific Reports*, 2021, **11**, 16166. https://doi.org/10.1038/s41598-021-95509-2
19. Liu, P., Li, W., Tan, R., Zhongbin, L, Bin, Z. Investigation of pyrolysis behavior shale gas oil-based drilling cuttings kinetics and product characteristics. *Scientific Reports*, 2025, **15**, 19775. https://doi.org/10.1038/s41598-025-04640-x
20. Bai, J. R., Song, K. T., Chen, J. B. The migration of heavy metal elements during pyrolysis of oil shale in Mongolia. *Fuel*, 2018, **225**, 381–387. https://doi.org/10.1016/j.fuel.2018.03.168
21. Zhang, Y., Guan, J., Qiao, P., Li, J., Zhang, W. Effects of secondary reaction of primary volatiles on oil/gas yield and quality in oil shale pyrolysis. *Journal of Fuel Chemistry and Technology*, 2021, **49**(7), 924–932. https://doi.org/10.1016/S1872-5813(21)60046-4
22. Zhan, H., Qin, F., Chen, S., Chen, R., Meng, Z., Miao, X. et al. Two-step pyrolysis degradation mechanism of oil shale through comprehensive analysis of pyrolysis semi-cokes and pyrolytic gases. *Energy*, 2022, **241**, 122871. https://doi.org/10.1016/j.energy.2021.122871
23. Huang, Y., Zhang, M., Lyu, J., Yang, H., Liu, Q. Modeling study on effects of intraparticle mass transfer and secondary reactions on oil shale pyrolysis. *Fuel*, 2018, **221**, 240–248. https://doi.org/10.1016/j.fuel.2018.02.076
24. Yang, D., Tanilas, K., Konist, A., Järvik, O. Evaluating LA-ICP-MS and digestion-based ICP-MS methods for trace elements determination in oil shale and its solid wastes. *Talanta*, 2025, **295**, 128319. https://doi.org/10.1016/j.talanta.2025.128319
25. Quann, R. J., Neville, M., Janghorbani, M., Mims, C. A., Sarofim, A. F. Mineral matter and trace-elements vaporization in a laboratory-pulverized coal combustion system. *Environmental Science & Technology*, 1982, **16**(11), 776–781. https://doi.org/10.1021/es00105a009
26. Al-Ayed, O. S., Qawaqneh, M. K., Abu-Nameh, E. S. M. Tracing rare earth elements in oil shale ash. *Oil Shale*, 2024, **41**(2), 132–143. https://doi.org/10.3176/oil.2024.2.04

27. Habib, A., Serniabad, S., Khan, M. S., Islam, R., Chakraborty, M., Nargis, A. et al. Kinetics and mechanism of formation of nickel (II)porphyrin and its interaction with DNA in aqueous medium. *Journal of Chemical Science*, 2012, **133**, 83. https://doi.org/10.1007/s12039-021-01945-y
28. Stasiuk, R., Matlakowska, R. Postdiagenetic bacterial transformation of nickel and vanadyl sedimentary porphyrins of organic-rich shale rock (Fore-Sudetic Monocline, Poland). *Frontiers in Microbiological Chemistry and Geomicrobiology*, 2021, **12**, 772007. https://doi.org/10.3389/fmicb.2021.772007
29. Yakubov, M., Abilova, G., Tazeeva, E., Yakubova, S., Tazeev, D., Mironov, N. et al. A comparative analysis of vanadyl porphyrins isolated from resins of heavy oils with high and low vanadium content. *Processes*, 2021, **9**(12), 2235. https://doi.org/10.3390/pr9122235
30. O'Day, P. A. Chemistry and mineralogy of arsenic. *Elements*, 2006, **2**(2), 77–83. https://doi.org/10.2113/gselements.2.2.77
31. Sikonia, J. G. Arsenic management in shale oil upgrading. Environmental Geochemistry and Health, 1985, **7**, 64–68. https://doi.org/10.1007/BF01771340
32. Al-Ayed, O. S., Al-Harahsheh, A., Khaleel, A. M., Al-Harahsheh, M. Oil shale pyrolysis in fixed-bed retort with different heating rates. *Oil Shale*, 2009, **26**(2), 139–147. https://doi.org/10.3176/oil.2009.2.06
33. Voolmaa, M., Soesoo, A., Puura, V., Hade, S., Aosaar, H. Assessing the geochemical variability of oil shale in the Attarat Um Ghudran deposit, Jordan. *Estonian Journal of Earth Sciences*, 2016, **65**(2), 61–74. https://doi.org/10.3176/earth.2016.06

Ministry of Energy and Mineral Resources

International Oil Shale Conference, 4th
(BAU-OSC-4) October 2026

Al-Balqa Applied University

Oil shales are petroleum rock-material, and they are abundantly available in a few countries. The scientific community continues to investigate and search for the most optimal methods to benefit from the world's oil shale reserves. In this endeavor, to increase global knowledge of oil shale, conferences, symposiums, and workshops are organized in different parts of the world. Such meetings improve and accelerate scientific research and bring researchers closer together to share their thoughts and findings.

The organization of the 4th International Oil Shale Conference, at the end of October 2026 in Amman, Jordan, by Al-Balqa Applied University (BAU) in partnership with the Ministry of Energy and Mineral Resources (MEMR), will enhance participation by researchers and members of the industrial sector. BAU and MEMR believe that oil shale research communities must meet to discuss oil shale business opportunities and the progress made in oil shale research and technological advancements.

MEMR and BAU intend to provide a platform for investors and researchers to meet with technologists. Since Jordan is operating a power plant (attaratpower.com.jo), new research opportunities have emerged in ash utilization. During the conference, attention will be focused on the utilization of the huge quantities of ash produced. The ash contains nickel, vanadium, palladium, and many other metals.

Shale oil production is another dimension of oil shale industrialization. Unfortunately, the high sulfur content of pyrolyzed shale oil makes direct industrialization cumbersome. Researchers in Jordan have used ionic liquids to remove more than 60% of the sulfur content from shale oil.

The conference will host researchers, investors, and industry representatives from Estonia, China, Morocco, Australia, Kazakhstan, India, and possibly Brazil, as well as several other countries. Various MOUs have been signed between MEMR and commercial companies for oil shale exploration. The conference website will be available soon (https://www.bau.edu.jo/Conf/oilshale4), and the conference email address is bau.oilshaleconf@bau.edu.jo.

Conference sessions will cover mining and production; utilization for power generation; ash utilization; cement production; shale oil production; shale oil chemistry; physical and chemical characterization of shale oil; specialty chemical production; air pollution; and regulatory law.

Accepted papers will be published in the Oil Shale journal following the standard peer-review process. Research papers and posters will be accepted based on an initial evaluation of submitted abstracts.

A visit to the Attarat Power Company is part of the conference activities, and social events and tourist visits will be organized by the conference organizing committees. A visit to the ancient city Petra can be arranged for interested guests.

Conference Chairman
Professor Omar Al-Ayed

Conference website: https://www.bau.edu.jo/Conf/oilshale4, email: bau.oilshaleconf@bau.edu.jo

PUBLISHER
Estonian Academy Publishers
Kohtu 6
10130 Tallinn, ESTONIA
info@eap.ee
www.eap.ee

EDITORIAL OFFICE
Kohtu 6
10130 Tallinn, ESTONIA
hedi.tonso@eap.ee
www.eap.ee/oilshale

Subscription information is available at www.eap.ee/subscription

Subscription orders should be sent to subscription@eap.ee

ISBN 0208 189X (print)
ISSN 1736-7492 (electronic)

9 770208 189005